

POROUS POLYMER AND HYBRID MATERIALS FOR EFFICIENT LIQUID
PHASE SEPARATION

A Dissertation

by

CHENXU WANG

Submitted to the Office of Graduate and Professional Studies of
Texas A&M University
in partial fulfillment of the requirements for the degree of

DOCTOR OF PHILOSOPHY

Chair of Committee,	Lei Fang
Committee Members,	Hung-Jue Sue
	Hongcai Zhou
	Xiaofeng Qian
Head of Department,	Ibrahim Karaman

May 2020

Major Subject: Materials Science and Engineering

Copyright 2020 Chenxu Wang

ABSTRACT

Efficient liquid-phase separation technologies such as adsorption and membrane separation are promising to replace conventional energy-demanding separation processes. These techniques are also advantageous to deal with formidable water pollution challenges. This dissertation focuses on porous polymeric and hybrid materials that are developed as sorbents and membranes for selective adsorption, organic solvent nanofiltration, and water / oil separation applications.

The first chapter introduces benchmark industrial separation technologies and current challenges in this field from the perspective of materials research. The mechanisms of selective adsorption and membrane separation are discussed. Recent advances in the applications of polymeric materials in organic solvent nanofiltration and water / oil separation are reviewed, with representative examples discussed in details.

Chapter II reports a novel and highly efficient synthetic approach to porous polymer networks, through aldol triple condensation using methanesulfonic acid as catalyst and solvent. Aromatic porous polymer networks were obtained with high porosity and narrow pore size distribution. The porous material demonstrated fast and selective adsorption of organic small molecules in aqueous solution. In addition, the pristine composition of the reaction mixture was solution processable and enabled membranes fabrication for organic solvent nanofiltration applications, as described in Chapter III. These porous polymer network membranes exhibited retained structural integrity and

organic solvent nanofiltration performance with molecular-sieving selectivity and high permeability, in the presence of either a strong acid or strong base for extensive period.

Chapter IV reports a hybrid membrane made of a stainless-steel mesh coated with zinc oxide tetrapod crystals and polydimethylsiloxane. The presence of micrometer-size tetrapod crystals provided a rough surface, which amplified the hydrophobicity of polydimethylsiloxane, so that the water contact angle of the membrane was greatly increased. The hydrophobic and oleophilic membrane rejected water while letting the oil permeate through, suitable for potential applications in efficient water / oil separation.

Overall, this dissertation reports several examples of porous polymers and hybrid materials prepared through new synthetic and fabrication approaches. The separation mechanisms in a variety of scenarios were identified as either size-exclusion or wettability. Fundamental principles of structure-property relationships were used to guide the materials design and development. The selectivity, durability, and wettability for separation functions were tailored by engineering the porosity, aromaticity, and surface roughness of the materials, respectively. Further enhancement of the separation performances for real-life applications is anticipated through continued chemical and materials engineering approaches along this direction.

DEDICATION

Jiansheng Wang

Caixia Zhang

ACKNOWLEDGEMENTS

First, I would like to thank my PhD advisor and committee chair Dr. Lei Fang. He shaped my way of doing research and guided me to be a researcher with initiative and discipline. His support helped me get through the hardest times in research. None of these projects would work without his help.

I would like to thank my committee members Dr. Hung-Jue Sue, Dr. Hong-Cai Zhou and Dr. Xiaofeng Qian for their constructive advice on my dissertation and for graciously giving time to serve on my committee. I want to express sincere gratitude to collaborators outside of Fang group: Dr. Hong-Cai Zhou, Dr. Sarbajit Banerjee, Dr. Qiang Zhang, and Ms. Aayushi Bajpayee. Special thanks go to Dr. Sue and his team on deep collaboration on the epoxy additives project: Mr. Shuoran Du, Ms. Cong Liu, Mr. Zhiyuan Jiang, Mr. Zewen Zhu, Mr. Qihui Chen and Dr. Spencer Hawkins, who trained me on tensile tests and DMA.

I'm grateful for those came before me and gave me warm welcome and professional guidance in the Fang group: Dr. Yang Zou, Dr. Yen-Hao Lin, Dr. Jongbok Lee, Dr. Congzhi Zhu, Dr. Tianyu Yuan and Dr. Alex Kalin. Special thanks go to Dr. Zi-Hao Guo who mentored me in my first year of PhD program, led my way to become a researcher. To my fellow colleagues in Fang group: Dr. Caili Zhang, Dr. Wei Hu, Mr. Sai Che, Ms. Xiaozhou Ji, Ms. Mariela Vazquez, Mr. Anthony Mu, Ms. Che-Hsuan Chang, Ms. Bailey Philips, Mr. Yirui Cao, Mr. Bo-Ji Peng, Mr. Chenxuan Li, Ms. Mingwan Leng, and Mr. Octavio Miranda, your care and generous support in my research make me feel

home in the Fang group. Thanks to Chenxuan Li and my undergrad student Evan Rutledge who worked 2 years with me and contributed much in my research. Good luck to Chenxuan on continuing on the research projects. Thanks to Bailey Philips for helping clear some of the format errors in this dissertation.

I want to also acknowledge the help and support from faculty members and staff in Department of Materials Science & Engineering, Department of Chemistry, Material Characterization Facility, and Microscopy & Imaging Center at Texas A&M University. I'm also grateful for financial support and award from China Scholarship Council Doctorate Fellowship, Kaneka Senior Graduate Student Scholarship, PTIC Poster Award, and Kunpeng Environment Sci-Tech.

I'm grateful to the support and love from my parents Jiansheng Wang and Caixia Zhang, who support me to pursue a PhD degree in United States. I'm very much thankful to my girlfriend Jingru Zhang for her love, caring, and understanding to finish my research work.

CONTRIBUTORS AND FUNDING SOURCES

Contributors

This work was supervised by a dissertation committee consisting of Professors Lei Fang (chair of committee), Hung-Jue Sue, and Xiaofeng Qian of the Department of Materials Science & Engineering and Professor Hong-Cai Zhou of the Department of Chemistry.

The synthesis of porous polymer networks (PPNs) and their precursors were conducted by Dr. Zi-Hao Guo in Chapter 2. The FTIR analysis in Chapter 2 was done by Dr. Zi-Hao Guo. The N₂ adsorption data and porosity analysis in Chapter 2 and 3 were provided by Dr. Qiang Zhang and Sai Che. The PXRD analysis of PPN membranes in Figure 41 in Chapter 3 were provided by Sai Che. The Solid-State NMR data for Chapter 2 and 3 were provided by Dr. Vladimir Bakhmoutov in Department of Chemistry. The organic solvent nanofiltration (OSN) performance of mixed dye solutions in Figure 47 and the OSN performance of *p*-PPN membrane treated with 5M MeONa in Chapter 3 was collected by Chenxuan Li. The SEM pictures of ZnO crystals in Figure 56 a and b in Chapter 4 were provided by University of Nottingham Ningbo China. The elemental analysis data of PPNs in Chapter 2 were provided by Robertson Microlit Laboratories.

All other work conducted for the dissertation was completed by the student independently.

Funding Sources

Graduate study was supported by a fellowship from Texas A&M University and a fellowship from China Scholarship Council.

This work was also financially supported by Texas A&M University, Kunpeng Environment Sci-Tech, Welch Foundation Grants (A-1898 and A-1725), and a Welch Foundation Endowed Chair Grant (HJZ A-0030).

NOMENCLATURE

ACN	Acetonitrile
AFM	Atomic Force Microscopy
API	Active Pharmaceutical Ingredient
ATC	Aldol Triple Condensation
BET	Brunauer-Emmett-Teller
BPA	Bisphenol A
CD	Cyclodextrin
CFP	Carbon Fiber Paper
CMP	Conjugated Microporous Polymer
COF	Covalent Organic Framework
CR	Congo Red
DFT	Density Functional Theory
DMF	<i>N,N</i> -dimethylformamide
FT-IR	Fourier Transformed Infrared Spectroscopy
ISA	Integrally Skinned Asymmetric
k_B	Boltzmann constant
MB	Methylene Blue
MJ	Megajoules
MOF	Metal Organic Framework
MSA	Methanesulfonic Acid

MWCO	Molecular Weight Cut Off
MWRO	Molecular Weight Retention Onset
OSN	Organic Solvent Nanofiltration
PDMS	Polydimethylsiloxane
PEG	Polyethylene Glycol
PI	Polyimide
PIM	Polymer of Intrinsic Microporosity
ppb	part per billion
ppm	part per million
PPN	Porous Polymer Network
PTFE	Polytetrafluoroethylene
PTSA	<i>p</i> -toluenesulfonic acid
PXRD	Powder X-Ray Diffraction
RB	Rose Bengal
SEM	Scanning Electron Microscope
SRNF	Solvent Resistant Nanofiltration
SSNMR	Solid-state Nuclear Magnetic Resonance
TEOS	Tetraethyl Orthosilicate
TFC	Thin Film Composite
TGA	Thermogravimetric Analysis
THF	Tetrahydrofuran
TMP	Transmembrane Pressure

WCA	Water Contact Angle
WSA	Water Shedding Angle
λ	mean free path
η	viscosity
κ	porosity

TABLE OF CONTENTS

	Page
ABSTRACT	ii
DEDICATION	iv
ACKNOWLEDGEMENTS	v
CONTRIBUTORS AND FUNDING SOURCES	vii
NOMENCLATURE	ix
TABLE OF CONTENTS.....	xii
LIST OF FIGURES	xv
LIST OF TABLES.....	xxiii
CHAPTER I INTRODUCTION.....	1
1.1 Energy-efficient Separation.....	1
1.2 Mechanism of Selective Adsorption and Membrane Separation	5
1.2.1 Selective Adsorption.....	5
1.2.2 Membrane Separation	13
1.3 Polymer Membrane Fabrication	18
1.4 Separation Application: Organic Solvent Nanofiltration	24
1.5 Separation Application: Water/Oil Separation	29
CHAPTER II COST EFFECTIVE SYNTHESIS AND SOLUTION PROCESSING OF POROUS POLYMER NETWORKS THROUGH METHANESULFONIC ACID MEDIATED ALDOL TRIPLE CONDENSATION.....	32
2.1 Introduction	32
2.2 Synthesis	33

2.3 Characterization.....	36
2.4 Selective Adsorption.....	46
2.5 Conclusion.....	52
2.6 Experimental Section.....	53
2.6.1 General Information.....	53
2.6.2 Synthesis.....	54
2.6.3 Adsorption Test.....	54
2.6.4 Carbon Fiber Paper/ p-PPN Composite Membrane Fabrication.....	55

CHAPTER III AROMATIC POROUS POLYMER NETWORK MEMBRANES FOR ORGANIC SOLVENT NANOFILTRATION UNDER EXTREME CONDITIONS..... 57

3.1 Introduction.....	57
3.2 Fabrication of PPN membranes.....	59
3.3 Characterization.....	67
3.4 Organic Solvent Nanofiltration Performance.....	72
3.5 Stability Test.....	81
3.6 Conclusion.....	87
3.7 Experimental Section.....	88
3.7.1 General Information.....	88
3.7.2 Fabrication of PPN Thin Film.....	89
3.7.3 Fabrication of PPN Membranes for OSN.....	89
3.7.4 OSN Tests of PPN Membranes.....	90

CHAPTER IV ZNIC OXIDE / PDMS HYBRID MEMBRANE FOR WATER / OIL SEPARATION..... 92

4.1 Introduction.....	92
4.2 Synthesis of Zinc Oxide Tetrapod Crystals.....	94
4.3 Spray Coating of Hydrophobic Hybrid Membranes.....	98
4.4 Application of Water / Oil Separation.....	108
4.5 Conclusion.....	110
4.6 Experimental Section.....	111
4.6.1 Synthesis of Zinc Oxide Tetrapod Crystals.....	111

4.6.2 Preparation of ZnO / TEOS and ZnO / PDMS Hybrid Membranes	112
4.6.3 Water/oil Separation of ZnO / PDMS Hybrid Membrane	113
CHAPTER V CONCLUSIONS	114
5.1 Porous Polymer Networks and Their Membranes for Selective Adsorption and Organic Solvent Nanofiltration	114
5.1.1 Summary	114
5.1.2 Perspective	115
5.2 ZnO / PDMS hybrid membranes for Water /oil Separation	118
5.2.2 Perspective	119
REFERENCE	120

LIST OF FIGURES

	Page
Figure 1. In-plant and separation energy use for energy-intensive industries. Reproduced from technical report of Department of Energy, doi:10.2172/1218755.	2
Figure 2. Relative energy use by various separation technologies. Reproduced from technical report of Department of Energy, doi:10.2172/1218755.	3
Figure 3. Energy consumption to concentrate 1 m ³ of a dilute solution in methanol by a factor of 10, using (a) distillation and (b) membrane filtration. Reproduced from Marchetti, P.; Livingston, A. G. et al, Chem. Rev. 2014, 114, 10735. With permission from American Chemical Society.	4
Figure 4. Size selective separation of water-soluble substrates by COP-99. (a) Change in dye concentrations over time after being treated with COP-99 in terms of absorbance relative to initial absorbance (C/C ₀); (b) surface area distribution with respect to pore size, and its relation towards minimum Van der Waals size of dye molecules. Reproduced from Byun, J., Patel, H., Thirion, D. et al. Nat Commun 7, 13377 (2016). https://doi.org/10.1038/ncomms13377	8
Figure 5. (a) Dye adsorption capacities of SCF-FCOF-1 at 25 C (initial dye concentration: 500 mg L ⁻¹); (b) UV-vis spectra of the car/MG mixed solution (v/v = 1 : 1, 100 mg L ⁻¹) treated with SCF-FCOF-1 in pristine (red curve) and equilibrium (black curve) states. The inset photograph shows the colors of carmine, malachite green, and the mixed solution before and after adsorption. Reproduced from Liao, Q.; Xi, K. et al., J. Mater. Chem. A 2019, 7, 18959. With permission from The Royal Society of Chemistry.	11
Figure 6. Profiles of chemical potential, pressure, and solvent activity characteristic of pressure-driven filtration of a one-component solution through a membrane according to (a) solution-diffusion and (b) pore-flow transport models. Reproduced from Marchetti, P.; Livingston, A. G. et al, Chem. Rev. 2014, 114, 10735. With permission from American Chemical Society.	16
Figure 7. ISA membrane formation process by phase inversion. Reproduced from Marchetti, P.; Livingston, A. G. et al, Chem. Rev. 2014, 114, 10735. With permission from American Chemical Society.	20

Figure 8. Schematic representation of the COMs (M-TpBD) fabrication. Reproduced from Kandambeth, S.; Banerjee, R. et al., <i>Adv. Mater.</i> 2017, 29, 1603945. With permission from John Wiley and Sons.	22
Figure 9. Nanofiltration performances of p-CMP, m-CMP and o-CMP membranes. a, Rejection behaviour of different CMP membranes versus the molecular weight of various dyes in ethanol; b) ultraviolet visible absorption spectra of PPh-IX dye in methanol to evaluate the separation performance of the p-CMP membrane; c) plot of solvent permeance through different CMP membranes against the solvent viscosity; d) permeance for methanol versus the reciprocal membrane thickness for p-CMP, m-CMP and o-CMP; e) plot of hexane, methanol and ethanol permeances with time for p-CMP membranes; f) rejection behaviour of post-modified p-CMP-OH membranes by different moieties. Reproduced from Liang, B.; Tang, Z. et al., <i>Nat. Chem.</i> 2018, 10, 961. With permission from Springer Nature.	27
Figure 10. PTFE coated mesh with superhydrophobic and superoleophilic properties. SEM pictures showed morphology of a) coated mesh and b) ball-like PTFE sphere; c) water contact angle and diesel oil contact angle of PTFE mesh. Reproduced from Feng, L.; Zhu, D. et al., <i>Angew. Chem. Int. Ed.</i> 2004, 43, 2012. With permission from John Wiley and Sons.	30
Figure 11. Structural formula of the monomers M1 - M5 and methanesulfonic acid catalyzed ATC reaction for p-PPN.	34
Figure 12. Photos of reaction process for p-PPN synthesis.	35
Figure 13. a) BET surface areas of p-PPN synthesized at different reaction temperatures; b) 77 K N ₂ sorption isotherms and c) Pore size distribution of the p-PPN sample synthesized at 110 °C.	36
Figure 14. FT-IR spectroscopy of p-PPN samples obtained from different reaction temperatures (100 °C, 110 °C, 130 °C and 150 °C).	37
Figure 15. TGA traces of PPNs.	38

Figure 16. ^{13}C CP/MAS NMR spectra of the p-PPN (from 110 °C reaction temperature) recorded at magic-angle spinning (MAS) rate of 5 kHz, asterisks (*) indicate rotational sidebands.	38
Figure 17. ^{13}C CP/MAS NMR spectra of the PPN5 recorded at a rate of 5 kHz, asterisks (*) indicate rotational sidebands. The major two signals at 146.7 ppm and 128 ppm correspond to the carbon connected to nitrogen and other aromatic carbons, respectively.....	39
Figure 18. ^{13}C CP/MAS NMR spectra of the PPN4 recorded at a rate of 5 kHz, asterisks (*) indicate rotational sidebands. the signals at 149.9 ppm and 141.2 ppm correspond to substituted aromatic carbons, the signal at 128 ppm corresponds to unsubstituted aromatic carbons. The signal at 30 ppm corresponds to the carbon at the center of spirofluorene. Note that the signal/noise ratio of was still low despite 27,000 scans.	39
Figure 19. Plot of the linear region on the N_2 isotherm of p-PPN sample synthesized at 110 °C for BET	40
Figure 20. (a) N_2 Adsorption Isotherms of PPN2 at 77K; (b) plot of the linear region on the N_2 isotherm of PPN2.....	41
Figure 21. (a) N_2 Adsorption Isotherms of PPN3 at 77K; (b) plot of the linear region on the N_2 isotherm of PPN3 for BET.	41
Figure 22. (a) N_2 Adsorption Isotherms of PPN5 at 77K; (b) plot of the linear region on the N_2 isotherm of PPN5 for BET.	42
Figure 23. SEM pictures showed morphology of powder samples of a) p-PPN, b) PPN2, c) PPN3, d) PPN4, e) PPN5.....	45
Figure 24. (a) Plot of relative concentration changes of different dye solutions versus time upon treating with p-PPN; (b) example UV-vis spectra of MB solution at different time after the addition of p-PPN, inset shows the photo of MB solution before and 5 min after adsorption process started; (c) molecular sizes of the tested dye molecules, the bars range from the minimal projection diameters to maximal projection diameters of the solutes.....	46

Figure 25. Maximal and minimal projection radius of (a) bromothymol blue, (b) rose bengal, (c) bisphenol A, (d) rhodamine B, (e) congo red, (f) methylene blue.	47
Figure 26. UV-vis spectrum of organic molecules: (a) bisphenol A, (b) bromothymol blue, (c) rhodamine B, (d) rose Bengal, (e) congo red in water absorbed by p-PPN	48
Figure 27. Maximum adsorption capacity of p-PPN to methylene blue solution indicated by Langmuir adsorption isotherm.	49
Figure 28. Recycling of <i>p</i> -PPN for methylene blue adsorption.	49
Figure 29. (a) “Soaking-heating-washing” cycles for the fabrication of CFP/ <i>p</i> -PPN composite membrane; scanning electron microscopy (b) top view and (c) cross-section view of CFP/ <i>p</i> -PPN composite membrane.	50
Figure 30. (a) Surface view and (b) cross-section view of CFP.	51
Figure 31. Weight change of CFP/ <i>p</i> -PPN composite membranes	51
Figure 32. UV-vis spectrum of methylene blue solution treated by CFP/ <i>p</i> -PPN composite membranes	52
Figure 33. a) Synthetic scheme of cross-linked conjugated PPNs (<i>p</i> -PPN, <i>m</i> -PPN, and <i>tri</i> -PPN) through aldol triple condensation reaction; b) graphic representation of the membrane fabrication using an MSA solution of the monomer.	59
Figure 34. a) Photographic image of a free-standing thin <i>tri</i> -PPN membrane with ~200 nm thickness on a copper loop; b,c,f) AFM images showing the surface morphology and thickness of the thin <i>tri</i> -PPN membrane; d,e) SEM images showing the flexible nature and the cross section of the thin <i>tri</i> -PPN membrane. g) photographic image of a thick <i>p</i> -PPN membrane for OSN with thickness of ~100 μm; h,i) SEM images of the surface and cross-section view of the thick <i>p</i> -PPN membrane.	61
Figure 35. Transfer a PPN thin film from glass substrate onto a silica wafer.	62

Figure 36. Thickness of a, b) p-PPN and c, d) m-PPN thin membranes measured by AFM.....	62
Figure 37. Top-view AFM of a) p-PPN and b) m-PPN membranes.....	63
Figure 38. Cross section SEM image of tri-PPN membrane fabricated from 30 mg/mL of 1,3,5-triacetylbenzene solution.....	63
Figure 39. Top and cross-section views of a, c) m-PPN and b, d) tri-PPN membranes for OSN tests. Cross-section view of e) p-PPN membrane with high magnification.	64
Figure 40. Photographic images of the freestanding a) m-PPN and b) tri-PPN membranes (4.7 cm in diameter) on top of worded white paper.	65
Figure 41. Contact angle of a) p-PPN, b) m-PPN, and c) tri-PPN membranes.....	65
Figure 42. Characterization data of p-PPN, m-PPN, and tri-PPN membranes: a) Aromatic fingerprint region of FTIR spectra; b) SSNMR spectra; c) N ₂ adsorption isotherms; d) TGA traces.....	67
Figure 43. Full FTIR spectra of membranes of a) p-PPN, b) m-PPN, and c) tri-PPN.....	68
Figure 44. Powder X-ray diffraction of p-PPN, m-PPN and tri-PPN.	69
Figure 45. Pore size distribution of membranes of a) p-PPN, b) m-PPN, and c) tri-PPN, calculated based on DFT method.	70
Figure 46. Estimated pore size from ideal structure of a) p-PPN b) m-PPN, and c) tri-PPN by Chem3D.....	71
Figure 47. OSN performance of p-PPN, m-PPN, tri-PPN membranes: a) rejection rate as a function of the molecular weight of the dye solute; b) membrane permeance values as a function of the solvent viscosity; c) rejection of brilliant blue verses permeability of methanol for PPN membranes, comparing with reported microporous polymer membranes, including COFs,	

polyarylate, CMPs, and cyclodextrin. The dash line indicates an upper bond.	72
Figure 48. Photographic image of a p-PPN membrane performing OSN in a solvent resistant	73
Figure 49. UV-vis spectra of feed permeate and retentate of dye molecules before and after OSN by p-PPN membranes. a) rose bengal, b) brilliant blue, c) congo red, d) bromothymol blue, e) rhodamine B, f) fluorescein	73
Figure 50. Scheme of dye separation performance of p-PPN membrane and UV-vis absorption spectra of the feed solution and the permeate: a) separating (1) rhodamine B from (2) bromothymol blue, (3) congo red and (4) brilliant blue; b) separating (1) fluorescein and (2) rhodamine B from (3) bromothymol blue.	76
Figure 51. Plot of permeance of solvent against a) molecular diameter of solvents, b) combined solvent properties (Hansen solubility parameter \times $1/\text{viscosity} \times 1/(\text{molecular diameter})^2$), and c) dielectric constant.	79
Figure 52. Flux of a) methanol, b) toluene, and c) THF vs transmembrane pressure relationship of p-PPN membrane.....	80
Figure 53. FTIR of pristine p-PPN membrane and p-PPN membranes treated by extreme conditions for 5 days. The conditions were 18 M H_2SO_4 , 14 M NaOH in water/methanol, 0.1 M chromic acid, and 2 M NaBH_4 in methanol.	82
Figure 54. Surface morphology of and p-PPN membranes treated by extreme conditions for 5 days. The conditions are 18 M H_2SO_4 , 14 M NaOH in water/methanol, 0.1 M chromic acid, and 2M NaBH_4 in methanol.	83
Figure 55. The rejection and permeance of congo red in methanol after p-PPN membrane soaking in 18 M H_2SO_4 for 2 days and the rejection and permeance of rose bengal in methanol after p-PPN membrane soaking in 5M MeONa for 2 days.	84

Figure 56. Long-term OSN test of p-PPN membrane filtrating isopropanol solutions of brilliant blue in the presence of PTSA and rose bengal in the presence of NaOH.....	84
Figure 57. Long-term OSN test of p-PPN membrane filtrating ethanol solutions of a) brilliant blue in the presence of PTSA and b) congo red in the presence of NaOH.....	86
Figure 58. a) Pretreated zinc samples in a sample boat made of stainless-steel mesh; b) and c) white fluffy zinc oxide products in tube.	94
Figure 59. SEM pictures of ZnO crystals. a) tetrapod crystalline structure and b) the zoomed-in SEM picture of a); c) lamella crystalline structure; d) commercially ZnO crystals.....	95
Figure 60. Continuous production cycle of zinc oxide tetrapod crystals	97
Figure 61. Spray coating of ZnO on stainless steel mesh with density of a) 7 mg/cm ² and b) 21 mg/cm ²	98
Figure 62. SEM pictures of spray-coated membranes (80 x80) with zinc oxide density a) 7 mg/cm ² and b) 21 mg/cm ²	99
Figure 63. SEM pictures of coated a) 120×120 mesh and b) 150×150 mesh with zinc oxide density of 21 mg/cm ²	100
Figure 64. Hydrolysis, condensation and polycondensation of tetraethyl orthosilicate to SiO ₂ network.....	101
Figure 65. Hydrosilylation of PDMS (Sylgard® 184) precursors.	102
Figure 66. SEM pictures of zinc oxide coated on membrane blew away during spray coating of TEOS with large spray pressure.	103
Figure 67. As-coated ZnO / TEOS membrane wetted by water. a) 80×80 mesh and b) 120×120 mesh. Spray coating density 21 mg/cm ²	103

Figure 68. Water contact angle of a) 120×120 ZnO / TEOS membrane ($148.7^\circ \pm 3.3^\circ$); b) 150×150 ZnO / TEOS membrane ($146.7^\circ \pm 1.3^\circ$); c) bare 80×80 stainless- steel mesh (75.9°) and d) 80×80 ZnO / PDMS membrane ($146.2^\circ \pm 1.2^\circ$)	104
Figure 69. A water droplet rolls off from a tilted ZnO / PDMS membrane within 0.2 seconds. Water shedding angle (WSA) = 8°	105
Figure 70. 1 ft ² ZnO / PDMS membrane made in lab.	107
Figure 71. Time lapse images of waste mineral oil / water mixture separated by ZnO / PDMS hybrid membrane. The pore size of the membrane was 180 μm and density of the lab-made ZnO was 21 mg/cm ²	108
Figure 72. Time lapse images of waste mineral oil / water mixture separated by a ZnO / PDMS hybrid membrane. The pore size of the membrane was 180 μm and the density of the commercial ZnO was 21 mg/cm ²	109
Figure 73. Time lapse images of waste mineral oil / water mixture separated by used lab-made ZnO / PDMS hybrid membrane. The pore size of the membrane was 180 μm and the density of the commercial ZnO was 21 mg/cm ²	109
Figure 74. Proposed method of carbon nanotube dispersed in MSA followed by introduction of PPN monomer which would form crosslinked network.	116
Figure 75. Synthetic route of F-CTF membrane preparation.	117
Figure 76. FTIR of starting materials of F-CTF compared with the product.	118
Figure 77. Scheme of ZnO crystals used for catalyst in photo-initiator in polymerization.	119

LIST OF TABLES

	Page
Table 1. Surface area and pore volume of PPNs, and the CFP/p-PPN composite.....	42
Table 2. Results of the elemental analysis of PPNs.	43
Table 3. Roughness of p-PPN, m-PPN, tri-PPN membranes measured by AFM.....	63
Table 4. Porosity of p-PPN, m-PPN, tri-PPN membranes	70
Table 5. Summary of dye molecules size and average rejection of PPN membranes	74
Table 6. Summary of OSN performance of aromatic PPN membranes compared with other state-of-art polymer membranes.....	78
Table 7. Summary of OSN performance in harsh condition of aromatic PPN membranes compared with commercial membranes.....	85
Table 8. Contact angle, anti-scratch, and water/oil separation performance of mesh coated with different materials	106

CHAPTER I INTRODUCTION

1.1 Energy-efficient Separation

Separation is a huge energy-consuming process and accounts for 22% of in-plant energy use in all manufacture industry, especially in chemicals, petroleum refining, forest products and mining (**Figure 1**).² In those industrial processes, target products are separated from byproducts / raw materials / solvents. Among all separation techniques, thermal-driven separations such as distillation, evaporation, and drying are the most energy-intensive methods and take up to 80% of energy use in large-scale separation processes (**Figure 2**).⁸ In this context, energy-efficient technologies such as extraction, adsorption, membrane separation, crystallization and physical property-based operations are excellent potential alternatives to those traditional high energy methods.⁸⁻¹⁰ However, their development and applications have not yet been fully explored and need more innovation and optimization.

For an example, to separate the solute and solvent from a 1 m³ diluted methanol solution (enthalpy of vaporization 37.6 MJ kmol⁻¹, heat capacity 81.6 J mol⁻¹ K⁻¹, and boiling point 337.7K), distillation typically consumes 1750 MJ, while an ideal membrane separation will only use 3 MJ at ambient temperature (**Figure 3**).¹ The large difference in energy consumption is a strong driving force to push the replacement of high energy-intensive technologies with energy-efficient and environmental-friendly methods. Other motivations include separation of temperature-sensitive materials that could be damaged

or degraded during distillation and solvent swap from a high boiling point solvent to a low boiling point one.¹¹

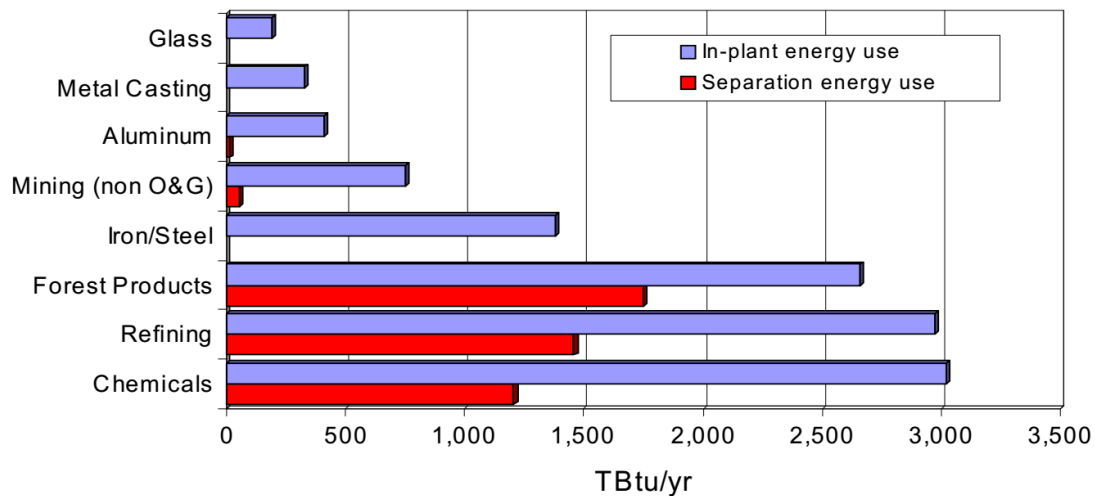


Figure 1. In-plant and separation energy use for energy-intensive industries. Reproduced from technical report of Department of Energy, doi:10.2172/1218755.²

Although there are many opportunities for new separation technologies, many practical problems hinder the employment of these new separation technologies in large scale industrial applications. From a materials research point of view, separating materials need to fulfill the following requirements in order to make those promising separation technologies eligible alternatives:²

- Distinct selectivity between target molecules and all other molecules in a complex system to make an efficient separation;
- Large flux / load capacity that fulfills the requirements of industry production rate;
- Long duration of operation, ability to avoid fouling problem in a certain period, as well as simple maintenance in terms of cleaning;

- Sufficient robustness that enables application under harsh conditions, such as high pressure, high temperature, extreme pH conditions, etc.; and
- Low cost for mass production of the separation materials.

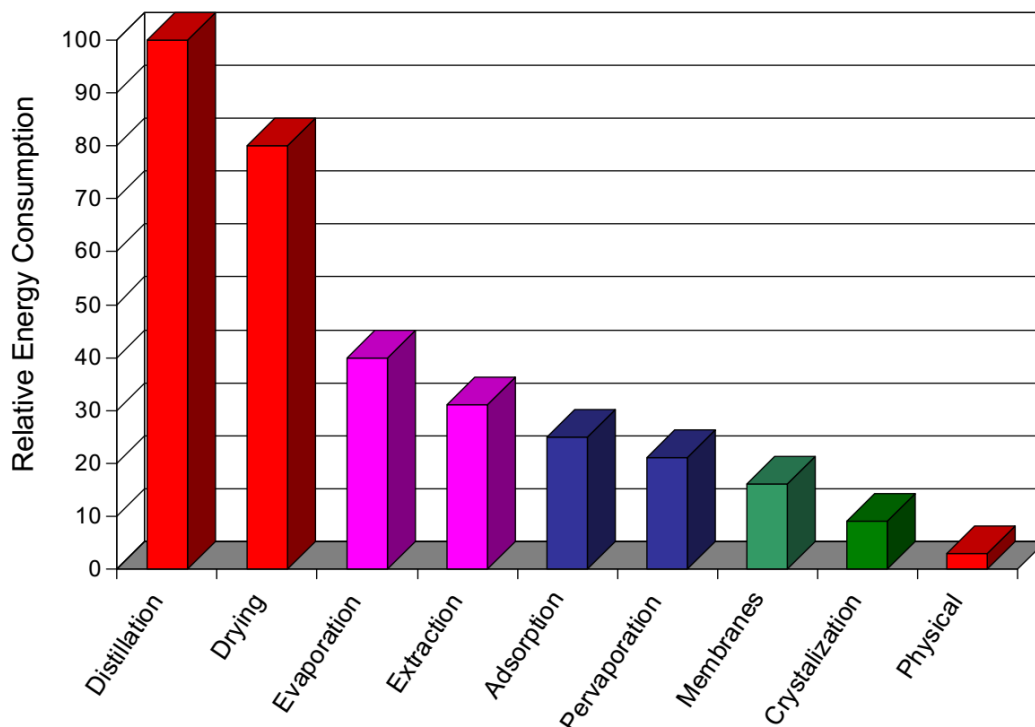


Figure 2. Relative energy use by various separation technologies. Reproduced from technical report of Department of Energy, doi:10.2172/1218755.²

These energy-efficient separation methods (extraction, adsorption, membrane, *etc.*) rely on the chemical / physical interactions of the separation materials and the components in the feeding solutions. Thus, each separation technique is limited to a specific application. Any method that aims to overcome those challenges should start with application-specific assessment on targeting separation system and define the target success.¹² After the metrics are identified, the following approaches on developing new separation materials or improving existing separation materials could be applied:²

- Enhance selectivity and fouling resistance by surface / pore modification techniques;

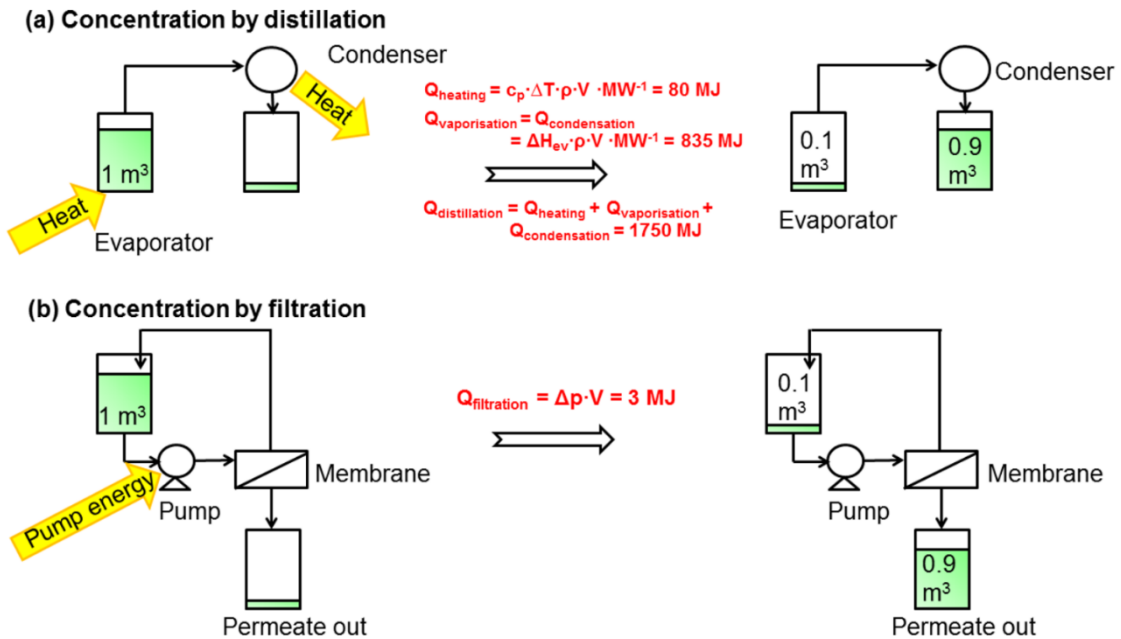


Figure 3. Energy consumption to concentrate 1 m³ of a dilute solution in methanol by a factor of 10, using (a) distillation and (b) membrane filtration. Reproduced from Marchetti, P.; Livingston, A. G. *et al*, Chem. Rev. 2014, 114, 10735.¹ With permission from American Chemical Society.

- Enhance flux / capacity by improving materials fabrication techniques for membrane, extraction, and adsorption system;
- Increase robustness to resist high pressure, high temperature, extreme pH conditions;
- Improve recovery and recycling ability of sorption materials;
- Improve permeance of membranes by decreasing thickness and by better design pore size distribution of defect-free membranes;

1.2 Mechanisms of Selective Adsorption and Membrane Separation

1.2.1 Selective Adsorption

Adsorption has been one of the most important techniques in water treatment area attracting more attention as new materials with better selectivity and capacity are emerging recently.¹³⁻¹⁵ Adsorption separates molecules depending on specific chemical / physical interactions between target molecules and the matrix.¹⁶ Typical interactions in selective adsorption include wettability such as hydrophilicity / hydrophobicity, charge interactions, and interactions between functional groups. Target molecules can compose a small portion in the mixture in certain processes, for example, CO₂ capture from fuel gas^{17,18} or a nitrogen mixture¹⁸ and recovery of specific metal ions in water¹⁹. It is energetically unfavorable to separate them from matrix and other solute molecules using distillation or diffusion. Instead, if the sorption materials exhibit exclusive interactions with target molecules, the targets can be captured by adsorption regardless of concentration gradient and then be desorbed from the sorbents afterwards. Active carbon is one of the most used sorption materials, however it exhibits poor selectivity on different molecules due to the broad pore size distribution and lack of specific interaction.¹⁶

Selective adsorption possesses several advantages over other separation methods. First, it is an inexpensive process which requires less energy compared with reverse osmosis or ion exchange, and the recycling of the sorption materials is usually simple.²⁰ Second, adsorption is a fast process which reaches equilibrium within hours or even

seconds with efficiency as high as 90 – 99 %.²¹ Third, there are versatile chemical modification options for sorption materials allowing specific interactions to be designed and imparted through the synthesis of the sorption materials.²²

Adsorption mechanism could be quantitatively studied by adsorption isotherms, which helps understand the adsorption behavior and effective system design.²³ The simplest adsorption isotherm is Henry's isotherm where only one parameter, equilibrium concentration of adsorbate, is considered.²⁴ The amount of adsorbate is proportional to the driving force, which is partial pressure of the adsorbate. The linear expression of this isotherm is

$$q_e = K_{HE}C_e$$

where q_e is amount of the adsorbate at equilibrium (mg/g), K_{HE} is Henry's adsorption constant, and C_e is equilibrium concentration of the adsorbate on the sorbents.

Langmuir isotherm was first used to describe gas-solid phase adsorption and also quantify adsorption capacity of the sorption materials.²⁵ In this isotherm, adsorption rate and desorption rate balance at equilibrium and the surface coverage could be obtained. Adsorption and desorption are proportional to the fraction of the open surface and covered surface of sorbents, respectively. The linear form of the Langmuir isotherm is in the following²⁶:

$$\frac{C_e}{q_e} = \frac{1}{q_m K_L} + \frac{C_e}{q_m}$$

Where C_e is concentration of adsorbate at equilibrium (mg/g), and K_L is Langmuir constant. K_L is related to porosity of the sorption materials indicating the large surface area leading into a higher adsorption capacity.

Freundlich isotherm applies to adsorption on heterogenous surface.²⁷ It describes the surface heterogeneity and the exponential distribution of the energy. Freundlich isotherm could be written as followed:

$$\log q_e = \log K_F + \frac{1}{n} \log C_e$$

where K_F is adsorption capacity and $1/n$ is adsorption intensity.

The Redlich-Peterson isotherm is an empirical isotherm combining elements from both Langmuir and Freundlich isotherms.²⁸ This isotherm does not follow ideal monolayer adsorption model. The model is described as followed:

$$q_e = \frac{AC_e}{1 + BC_e^\beta}$$

where A is Redlich-Peterson constant, B is constant, β is in the range of $0 \sim 1$, C_e is concentration of the adsorbent at equilibrium, and q_e is adsorbed molecules on sorbents at equilibrium.

The numerator part of Redlich-Peterson isotherm is linear dependent on concentration representing the Langmuir isotherm, while the denominator part is an exponential function representing Freundlich isotherm. The Redlich-Peterson isotherm is versatile and applicable in both homogenous and heterogenous systems.²⁹

Another adsorption model is Flory-Huggins isotherm that quantifies the degree of surface coverage of the adsorbates on the sorbents.³⁰ The linear form of Flory-Huggins equation is:

$$\ln \left(\frac{\theta}{C_o} \right) = \ln K_{FH} + n \ln(1 - \theta)$$

where θ is degree of surface coverage, n is number of the adsorbed molecules, and K_{FH} is Flory-Huggins equilibrium constant.

This model describes the feasibility of the adsorption process.

The key factors that determine efficiency of selective adsorption include adsorption rate, capacity, selectivity, recyclability and stability in solution. Adsorbates adhere on the surface of materials (adsorbents).¹³ Materials with intrinsic pores provide larger surface areas than nonporous materials do so that the efficiency of adsorption is enhanced. High porosity could be obtained by incorporating rigid backbone and

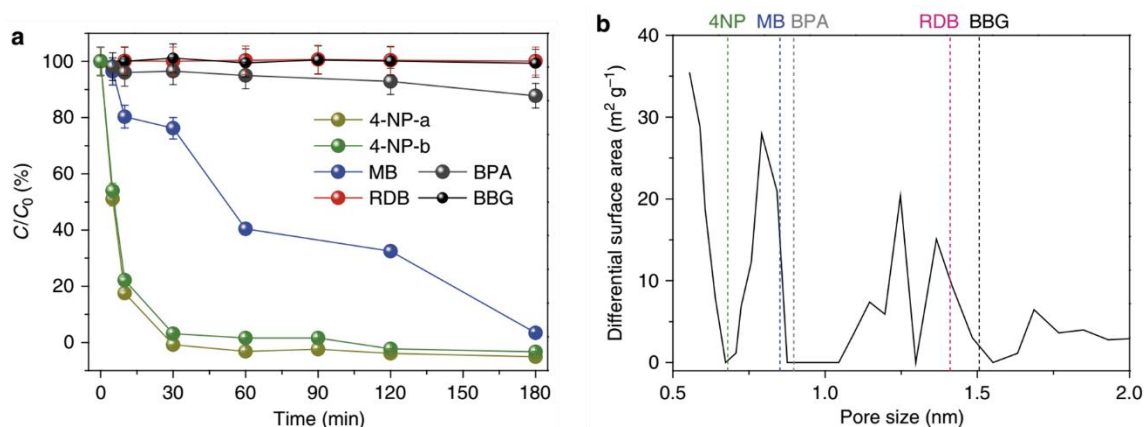


Figure 4. Size selective separation of water-soluble substrates by COP-99. (a) Change in dye concentrations over time after being treated with COP-99 in terms of absorbance relative to initial absorbance (C/C_0); (b) surface area distribution with respect to pore size, and its relation towards minimum Van der Waals size of dye molecules. Reproduced from Byun, J., Patel, H., Thirion, D. et al. Nat Commun 7, 13377 (2016).⁴ <https://doi.org/10.1038/ncomms13377>

crosslinked network into molecular design. Nowadays, porous structure and multifunctional groups are usually integrated to design sorption materials.

Porous polymers are able to adsorb organic molecules such as dyes and bisphenol A (BPA) from aqueous solution. While molecules smaller than the pores will be adsorbed into the abundant surface of the pores, larger molecules that cannot access the pores will not participate in the adsorption process. Considering the large surface areas of benchmark porous materials (in the order of hundreds to thousands m^2/g), the adsorption capacity of molecules with different sizes could be drastically different. In this way, small and large solute molecules are separated. Practically, for a more efficient size-selective adsorption, porous polymers are equipped with narrow pore size distribution and large pore volume / Brunauer-Emmet-Teller (BET) surface area. For example, Yavuz et al synthesized a fluorine functionalized porous polymer network COP-99 from a commercially available monomer through a catalyst free condensation reaction.⁴ It possessed narrow pore size distribution with three major pore sizes ranging from 0.5 – 1.4 nm and a decent BET surface area ($479 \text{ m}^2/\text{g}$) as a microporous material (pore size smaller than 2 nm). As a result, it exhibited distinct adsorption performance against dyes with different sizes (**Figure 4**). Small dye 4-nitrophenol that can access all pores in COP-99 was completely adsorbed within 30 min. Medium sized dye methylene blue that partially accessed pores in COP-99 was also fully adsorbed with a slower rate. Rhodamine B and brilliant blue with size larger than major pores of COP-99 were hardly adsorbed in equilibrium after 180 min. In fact, the similar adsorption behavior of 4-nitrophenol with different charges

in different pH conditions proved that the size-selectivity is a more important factor than fluorine-charge effect.

Polymers with specific functionalities such as hydroxyl, carboxyl, phosphate, amine, or thiol groups usually possess electronegative effects, either attraction or repulsion to charged molecules. Dyes with opposite charges can be simply separated using this method. Xi et al reported crystalline fluorinated covalent organic framework (COF) SCF-FCOF-1 and SCF-FCOF-2 using a solvothermal catalyst-free reaction.⁶ The formed COF exhibited a BET surface area exceeding 100 m²/g within one hour and reached a final BET surface area of 2056 m²/g after the 3-day reaction. They also scaled up the reaction to 1-gram scale with a yield of 87.9% and a surface area of 2018 m²/g. The high fluorine content of the COFs (13.3 wt% and 12.8 wt%, respectively) provided a strong affinity to

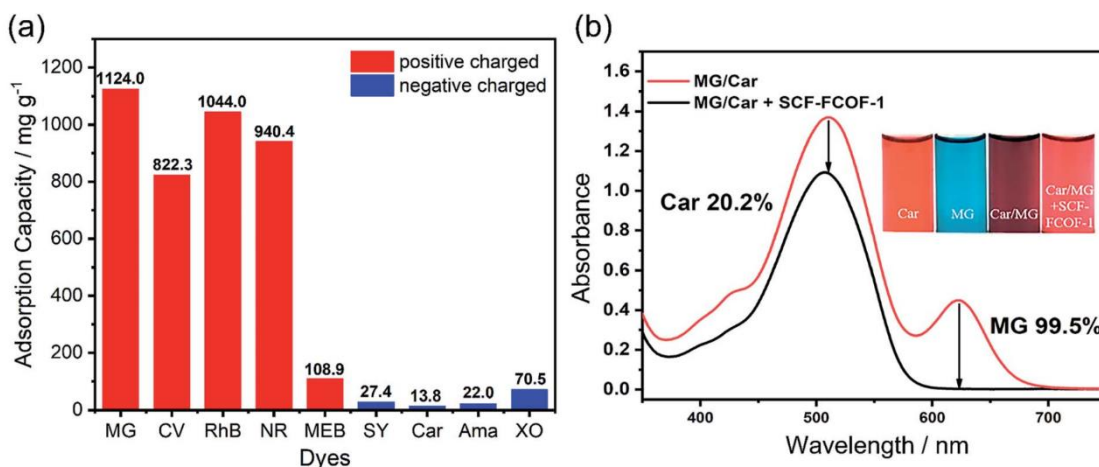


Figure 5. (a) Dye adsorption capacities of SCF-FCOF-1 at 25 C (initial dye concentration: 500 mg L⁻¹); (b) UV-vis spectra of the car/MG mixed solution (v/v = 1 : 1, 100 mg L⁻¹) treated with SCF-FCOF-1 in pristine (red curve) and equilibrium (black curve) states. The inset photograph shows the colors of carmine, malachite green, and the mixed solution before and after adsorption. Reproduced from Liao, Q.; Xi, K. *et al.*, *J. Mater. Chem. A* 2019, 7, 18959.⁶ With permission from The Royal Society of Chemistry.

cationic molecules. With the high BET surface area, ordered pore channels, and electronegative interaction, SCF-FCOF-1 showed excellent separation of cationic dyes from anionic dyes. Specifically, the adsorption capacity towards dyes with positive charges, such as crystal violet, rhodamine B, neutral red, and malachite green was in the range of 822 to 1124 mg/g, while the adsorption capacity to dyes with negative charges: sunset yellow, carmine, amaranth, and xylenol orange was only in the range of 13.8 ~ 70.5 mg/g (**Figure 5**). To be noticed, the pore size of the SCF-FCOF-1 was 3.3 nm, larger than all tested dyes indicating size selectivity was not a major factor in this case. Herein, the separation was due to the fluorine-cation interactions. They also ran a control experiment where an amorphous fluorinated polymer with similar chemical composition, but smaller

pore volume and poor crystallinity was used in dye adsorption test. The amorphous counterpart with similar hydrophobicity showed a much smaller adsorption capacity and a poor selectivity towards charged dyes. It indicated the importance of the porosity in selective adsorption.

Another selective adsorption mechanism is complexation / chemical interactions of target molecules with specific functional groups in sorption materials, such as chelating of thiol groups with heavy metal ions³¹, and sulfonate groups bonded with CO₂¹⁸. Those interactions are usually strong with high selectivity and fast kinetics. They can also be highly specific to certain metal ions. Ma et al synthesized a thiol functional porous organic polymer POP-SH by free radical polymerization from cheap starting materials.³² The POP-SH exhibited a high BET surface area 1061 m²/g and high density of thiol groups. With the benefit of soft-soft interaction between thiol and mercury, POP-SH showed an outstanding mercury ion adsorption capacity of 1216 mg/g, which outperformed many reported materials and even the theoretical uptake capacity of 1018 mg/g due to the synergetic effect of π -cation interaction. POP-SH was stable at different pH conditions and fully recyclable by a simple wash achieving a similar adsorption capacity of 1250 mg/g. POP-SH can reduce the concentration of mercury ion solution from 5 ppm to 1 ppb (less than the US Environmental Protection Agency acceptable limit 2 ppb) within 10 min and to 0.1 ppb after 3 h. POP-SH also showed selective adsorption to Hg²⁺ with efficiency of 98% in a complex solution containing several other metal ions with the same concentration. Other toxic ions such as Pb²⁺, Cd²⁺, Cu²⁺ were also captured while the

concentration of nontoxic ions, such as Ca^{2+} , Zn^{2+} , Mg^{2+} , Na^+ , was not changed. It was a result of selective interactions of the thiol groups with heavy metal ions.

Overall, the selection and structural design of sorption materials depend on adsorption mechanisms of targeting molecules, such as size-exclusion, electronegative interaction, complexation, wettability, or synergy of them. The adsorption behavior could be quantified by diverse adsorption models. As an energy-efficient and environmental-friendly process, adsorption is promising to replace many conventional separation processes. New sorption materials with higher selectivity, capacity, and cost-efficiency are the driving forces of this replacement.

1.2.2 Membrane Separation

Membrane separation has been used for replacing conventional energy-consuming industrial processes since 1960s.³³ Membrane separation is promising, because it requires less separation materials than adsorption and saves energy because pressure and concentration are used as the driving forces instead of heat. It is more advantageous in energy, environment, and safety concerns. Special membranes designed for ultrafiltration (target molecular weight 1k -100k), nanofiltration (target molecular weight 200 – 1k), reverse osmosis (targeting molecular weight < 200), and gas separation are attracting more and more attentions from both academia and industry.^{16,34} Some of the most important grand challenges confronted by humanity, such as sea water desalination³⁵ and carbon dioxide capture,³⁶ are relying on the breakthrough of membrane technology.

Generally, people use two models – pore flow model and solution diffusion model – to describe the molecule transportation in membranes (**Figure 6**).³⁷ Many other models were also derived from these two models such as Maxwell-Stefan equation,³⁸ Hagen-Poiseuille model,³⁹ Donnan steric pore flow model,⁴⁰ etc. Basically, the pore flow model regards membranes as porous membranes and describes molecule motion in pore channels. The solution diffusion model regards membranes as dense membranes and the molecules pass through the free volume of the membrane material. The major difference for “pores” in the pore flow model and “free volume” in the solution diffusion model is that the pores are persistent and do not change upon pressure or solvent.

In pore flow model, it is assumed that pores are larger than the size of solvent molecule. For those membranes with pore size much larger than kinetic diameters of molecules, free molecular transport (effusion mechanism) and modified Sampson’s model were used to explain the molecular diffusion behavior through the membranes.⁴¹ When Knudsen number λ/d (d is pore diameter, λ is mean free path) is greater than 1, the collision between molecules, and pore walls prevails over intermolecular collision. Effusion flux is described as

$$Q_E = \frac{\bar{u}\Delta n}{4} = \Delta P / \sqrt{2\pi m k_B T},$$

k_B is the Boltzmann constant, and m is the molecular weight.

This equation predicts that the diffusion rate is irrelevant with the pore size but proportional with $m^{-1/2}$. As d becomes greater than λ , molecules collide more frequently with each other and turn into a collective flow behavior. Modified Sampson’s formula^{42,43} was applied:

$$Q_s = \frac{1}{6\mu} \frac{\sum_i d_i^3}{\sum_i \pi d_i^2} \Delta P (1 + 0.894\kappa^2),$$

where d_i is the diameter of aperture i on the graphene, κ is the porosity.

Pore flow model also assumes the concentration of solution in pores is uniform and the driving force of the transportation is a pressure gradient.¹¹ In this case Darcy's law is used to describe molecular motion in pore flow model:

$$J_i = k \frac{p_0 - p_l}{l}$$

where k is the permeability coefficient, a function of structural factors, such as membrane pore size, porosity; l is the thickness of membrane.

Derived from Darcy's law, Hagen-Poiseuille model described pure solvent flux in cylinder pore channels without any concentration gradient:

$$V = \frac{\epsilon r_p^2}{8l\tau} \frac{\Delta p}{\eta} = K_{HP} \frac{\Delta p}{\eta}$$

where V is the solvent velocity, η is solvent viscosity; membrane structural factors K_{HP} , represented by pore size of membrane r_p , porosity ϵ , membrane tortuosity τ and membrane thickness l .

This equation exhibits that the solvent flux is only related to pressure difference, solvent viscosity, and membrane structural factors. It is proven in several examples involving nanofiltration in porous membranes. Several organic solvents passed through conjugated microporous polymer (CMP) membranes were investigated.⁷ Solvent permeance increased in inverse proportion to solvent viscosity, indicating the absence of interaction between solvent molecules and membrane materials. The solvent flux increased linearly with applied pressure. The product of permeance and viscosity was independent of Hansen solubility parameter, following the pore flow model and Hagen-Poiseuille equation. Lai et al compared permeance of several organic solvents and water in COF membranes with different thickness of the membranes. They found that the

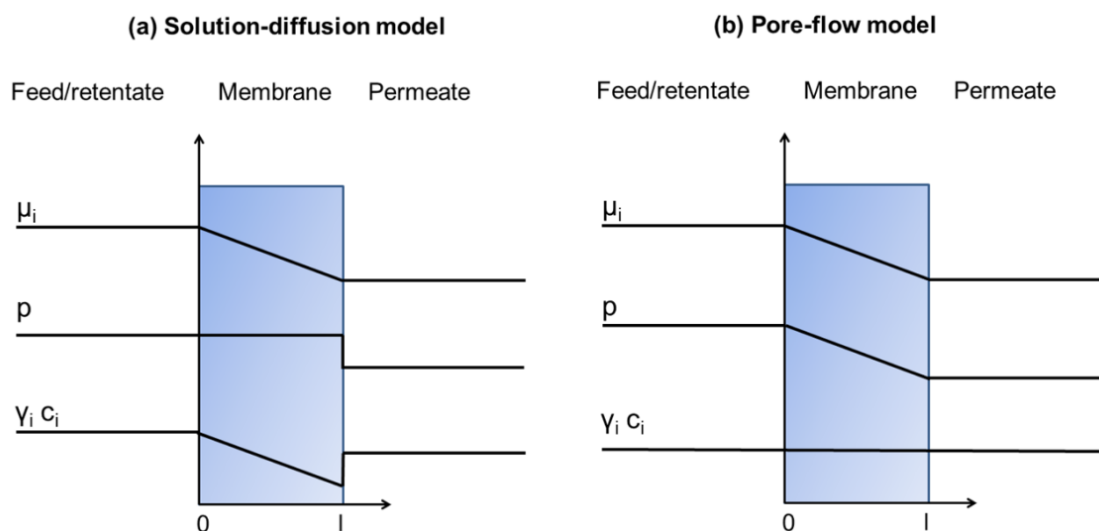


Figure 6. Profiles of chemical potential, pressure, and solvent activity characteristic of pressure-driven filtration of a one-component solution through a membrane according to (a) solution-diffusion and (b) pore-flow transport models. Reproduced from Marchetti, P.; Livingston, A. G. *et al*, Chem. Rev. 2014, 114, 10735.¹ With permission from American Chemical Society.

permeance was proportional to $1/\eta$ (solvent viscosity) instead of $\delta/\eta d^2$ (solubility parameter and solvent molecular size), which was the solvent permeance correlation of amorphous non-porous membrane.⁴⁴ Hence, the solvent transportation in COF membranes was governed by classic pore flow model.

Solute transportation in pore flow model, on the other hand, is more empirical.¹ Solute transport is affected by steric hinderance and interactions with the pore wall (membrane materials). Basically, solute molecules with molecular size larger than the pores are rejected, while solute molecules smaller than pores pass through. Any electronegative interaction between solute and pore wall will either facilitate or inhibit this process. Mathematically, several pore flow models have been developed. The simplest one used reflection coefficient, a function of the membrane pore size and solute diameter, to describe the motion. According to steric hindrance pore model,⁴⁵ the reflection coefficient σ_i is calculated as

$$\sigma_i = 1 - H_F S_F$$

$$H_F = 1 + \frac{16}{9} \lambda$$

$$S_F = (1 - \lambda)^2 [2 - (1 - \lambda)^2]$$

where $\lambda = \frac{d_i}{d_p}$, d_i and d_p are diameters of the solute and the pore. H_F and S_F represent effects of interaction with pore wall and steric hindrance of the pores, respectively.

Solution diffusion model considers the situation that molecules pass through dense membranes with a driving force of concentration gradient. The solute flux follows a similar principle with Fick's law:

$$J_i = -\frac{RTL_i}{c_i} \frac{dc_i}{dx}$$

where $-\frac{RTL_i}{c_i}$ is diffusion coefficient.

The simplest solution diffusion model derives a number of empirical models with extra factors considered. The classical solution diffusion model considers a pressure gradient as the co-driving force.⁴⁶ Maxwell-Stefan equation takes frictional and convective coupling effects between solute and solvent into account.⁴⁷ The interactions of multiple composition in solution are considered and the equation relies on species of composition. A linear relationship described the product of flux and viscosity as a function of Hansen solubility parameter of the solvent.⁴⁸ This model was adapted in ultrathin polyamide membranes as a phenomenological transport model.⁴⁹

$$P = K \left(\frac{\delta}{\eta d^2} \right)$$

where δ is the solubility parameter, η is solvent viscosity, and d is molar diameter of the solvent.

This equation reflects the strong interactions between solute, solvent and membrane materials.

1.3 Fabrication of Polymer Membranes

Polymers are widely used as materials of separation membranes because they possess many advantages, such as cost-efficiency, flexibility, and synthetic diversity, that

enable mass production, wide working range, and feasible chemical modification. Although the mechanical strength, chemical resistance, and degradation are still drawbacks compared with inorganic membranes, polymer membranes are still a more promising option for most large-scale membrane processes in industry.

The choice of fabrication method of polymer membranes depends on polymer solubility in solvent. For soluble polymers, phase inversion technique is the most prevalent and reproducible method, which was invented back in 1963 for osmosis membranes.³³ Phase inversion refers that a polymer transforms from a liquid phase to a solid phase resulting into a membrane with an asymmetric structure. During this process, the polymer in a uniform phase (casting solution) is transferred into two different phases (asymmetric structure): a porous/polymer-poor phase and a dense/polymer-rich phase.¹ The top surface of the casting solution contacts with the bad solvent of the polymer, and the polymer precipitates out forming a dense layer. The dense layer slows down the diffusion of the bad solvent into the underlying polymer solution resulting into a more porous sublayer.

In most cases, the polymer solution is immersed into the poor solvent by a roll-to-roll method to proceed phase inversion. Besides immersion precipitation, other methods are also sometimes used, including reducing temperature of the solution, exposing the casting solution in a bad solvent vapor, and evaporating the casting solution in an elevated

temperature. The structure of the formed membrane is affected by factors, such as solubility of the casting solvent in the bad solvent, solubility of the polymer in the bad solvent, and solvent temperature. Polymer membranes obtained with phase inversion

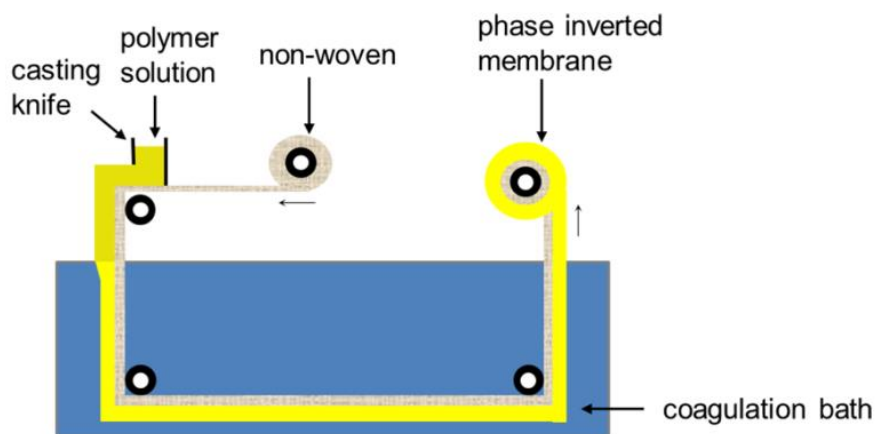


Figure 7. ISA membrane formation process by phase inversion. Reproduced from Marchetti, P.; Livingston, A. G. *et al*, Chem. Rev. 2014, 114, 10735.¹ With permission from American Chemical Society.

technique are called integrally skinned asymmetric (ISA) membranes (**Figure 7**). An ISA membrane could be used as a separation membrane by itself or the porous support of a top selective layer in a thin film composite (TFC) membrane.

One obvious drawback of the membranes produced by the phase inversion technique is that the polymer membranes could be dissolved in the casting solvent again, which limits the working environment of the membranes. In order to solve the problem, solvent resistant polymers with rigid backbone are preferred to be used, such as polyimide,⁵⁰⁻⁵³ polyamide,^{54,55} polysulfone,^{56,57} polyethersulfone,⁵⁸ etc. Post-treatment, crosslinking, is also sometimes used to improve the solvent resistance of the membrane.

For example, Hicke et al prepared copolymer PANGMA membranes by the phase inversion method.⁵⁹ The polymer solution in DMF was immersed into a bad solvent of water to form a polymer membrane. The polymer was subsequently crosslinked by ammonolysis where tri-functional ammonia was used as a crosslinking agent for 3 h at 50 °C. The resulting membranes were insoluble in various polar solvents including tetrahydrofuran (THF), acetone, DMSO, and the mother solvent DMF. The improved solvent resistance broadened the usage conditions of the ultrafiltration membranes.

Post-treatment is crucial to the membranes prepared by phase inversion, yet it has often been neglected. After phase inversion, the membranes are preferred to be dried in stages by a solvent exchange method.¹¹ First, the residual bad solvent in the membranes is replaced by a miscible solvent and is then replaced by a more volatile solvent. By doing so, the membranes are dried faster with minimal pore collapse risk. A Matrimid® polyimide membrane was obtained from a mixed solution of NMP/THF on a nonwoven support and was immersed into deionized water to undergo phase inversion.⁵¹ After that, a solvent-exchange process was conducted: the solvent in membrane was replaced with isopropanol for 3 h and then exchanged with toluene/lube oil for 3 days followed by drying in an oven at 65 °C. The solvent exchange process prevented cracking of the membranes during drying.

Polymers with little or no solubility such as crosslinked polymers cannot be prepared by phase inversion. Instead, they need to be polymerized *in-situ* in monomer solution. The two most popular methods used to fabricate crosslinked polymers are interfacial polymerization and the strategy of casting followed by *in-situ* polymerization.

Interfacial polymerization refers that two monomer solutions with immiscible solvents (usually organic solvent and water) form two layers and an interface. The monomers react at the interface and a layer of polymer membrane is generated. The reaction is self-terminated as the membrane forms a barrier of the two monomer solutions. The resulting membrane could be as thin as nanometer scale. Practically, a porous supporting membrane is often immersed into one of the monomer solutions and the other



Figure 8. Schematic representation of the COMs (M-TpBD) fabrication. Reproduced from Kandambeth, S.; Banerjee, R. et al., *Adv. Mater.* 2017, 29, 1603945.³ With permission from John Wiley and Sons.

monomer solution is casted on the support so that the resulting polymer membrane is formed at the surface of support. It provides mechanical support for the thin polymer membrane. This type of composite membrane is called TFC.

One of the classic combinations of monomers used for interfacial polymerized membranes is amines and acyl chlorides. Tri-functional trimesoyl chloride in hexane and bi-functional diaminobenzene in water formed an interface where a thin layer of crosslinked polyamide is formed.^{60,61} The resulting polyamide membranes were used for reverse osmosis and nanofiltration. A number of derivatives of polyamide were formed by monomers with versatile substitutions and functionalities.⁶²⁻⁶⁴ The crosslinked polyamide

membranes possessed robust chemical resistance to a broad range of polar and apolar solvents. In addition, the polyamide membranes conveyed the properties of the monomers. For example, monomers containing silicon and fluorine formed hydrophobic polyamide with highly improved permeance of apolar solvents, including toluene and ethyl acetate.⁶³ The porous support also played an important role affecting the performance of the selective layer. Livingston et al studied polyamides formed on crosslinked PI support and on PEEK support, respectively.⁶⁴ The hydrophilicity of porous supports influenced the solvent permeation. By treating the membranes with DMF, the solvent permeance was increased distinctly.

Solution casting followed by *in-situ* polymerization is another widely applied method to prepare crosslinked polymer membranes. The monomer solution was first cast on a support and then the polymerization is triggered *in-situ*. Sometimes, the monomer solution is pre-reacted to get the viscosity suitable for processing. The thickness of the membrane is controlled by concentration of the monomer solution and reaction time. Banerjee et al prepared crystalline COF membranes using this method (**Figure 8**).³ They cast the solution of monomers and catalyst on a clean glass and controlled the thickness of membranes by a knife-cast machine. The reaction temperature was over 100 °C, however, they found the membranes would crack if they raised the temperature to 90 °C directly. Instead, they increased the temperature stage by stage: 60 °C for 24 h, 90 °C for 24 h and 105 – 120 °C for 24 h. Crystalline COF membranes with BET surface areas from 515 – 1400 m²/g were fabricated. The COF membranes performed nanofiltration in water and several other organic solvents. The crosslinked porous membranes also showed

excellent stability upon harsh conditions, such as 3 M HCl. The COF membranes exhibited high permeance of water ($110 \text{ L m}^{-2}\text{h}^{-1}\text{bar}^{-1}$) and good size selectivity of different dyes.

While interfacial polymerization is only suitable for limited types of polymers that are synthesized by two-part monomers in two immiscible phases, the casting followed by *in-situ* polymerization from a homogenous monomer solution could be applied for a boarder range of polymers. In Chapter 3, free-standing porous polymer network membranes were fabricated by casting followed by *in-situ* polymerization.

1.4 Separation Application: Organic Solvent Nanofiltration

Membrane separation in liquid phase is classified into microfiltration, ultrafiltration, nanofiltration, and reverse osmosis depending on their molecular weight cut off (MWCO).⁵⁶ MWCO is the lowest molecular weight of solutes to which the rejection is over 90%. For nanofiltration, MWCO is usually in the range of 200 ~ 1000 g/mol. The target molecules are dyes, organic pollutant, active pharmaceutical ingredient (API), etc.¹ The corresponding separation membranes possess pores smaller than 2 nm or no pores. Nanofiltration performed in organic solvents is called organic solvent nanofiltration (OSN)¹ or solvent resistant nanofiltration (SRNF)¹¹. Electronegative interactions are weak in solvents while size exclusion is a dominate factor in OSN.

OSN is a simple operation method for processes, such as concentration, solvent exchange, and purification of solution of catalysts, pharmaceuticals, peptides, antibiotics, *etc.* OSN relies on reusable membranes and is driven by pressure, saving a large amount of energy and producing little waste emissions.

The performance of OSN membranes is characterized by solute rejection and solvent permeance. Similar with the trade-off relationship between selectivity and permeability of gas separation membranes,^{65,66} membranes with smaller MWCO (rejection to smaller molecules) usually display lower solvent permeance. However, with delicate molecular engineering, both good selectivity and permeability could be realized in membranes with ordered pores, narrow pore size distribution, and large porosity.⁶⁷

Cyclodextrin (CD)-based crosslinked polymer membranes were prepared by interfacial polymerization method using acyl chloride as a crosslinker.⁶⁸ The resulting membranes were flexible, hydrophilic with high mechanical strength. The crumpled structure provided a larger surface area that facilitated the transport of molecules with a solvent permeance 47 times higher than that of control flat films. By using the monomer solution with low concentration, the thickness of the membrane was controlled as thin as 180 nm. The CD membranes could be activated for a higher solvent permeance by 0.1 – 2 M NaOH solution which facilitated the access of molecules into CD cavities. The pore size of CD membranes was in the range of 0.5 ~ 0.8 nm leading to a low MWCO of 327 g/mol. However, with the assist of thin active layer and porosity, the methanol permeance of CD membranes was as high as $9.6 \text{ L m}^{-2}\text{h}^{-1}\text{bar}^{-1}$, which is 20 times higher than that of commercially available membranes. In another work, three types of membranes were synthesized with trimesoyl chloride and α -CD, β -CD, γ -CD, respectively.⁶⁹ Polar and nonpolar solvents could pass through the hydrophobic cavities of CDs and the hydrophilic channels outside of CD, respectively. Such a unique feature was called Janus pathway for

molecular transport. Similarly, α -CD, β -CD, and γ -CD membranes in this study showed MWCO of 320, 400, 550 g/mol, corresponding to the order of their pore size.

20-nm-thickness crosslinked polyarylate membranes were prepared by interfacial polymerization.⁷⁰ Polyarylate membranes with contorted structure possessed intrinsic porosity due to inefficient packing of the polymer chains. The polyarylate membranes were prepared on top of PTMSP membrane or polyimide P84 porous membrane for a TFC assembly. With a major pore size around 0.4 nm, the thin polymer membranes exhibited a MWCO of 249 g/mol and a decent methanol permeance of $8.0 \text{ L m}^{-2}\text{h}^{-1}\text{bar}^{-1}$. In contrast, polyarylate membranes synthesized with planar monomers displayed no porosity and much smaller solvent permeance. The polyarylate membranes showed high rejection to styrene oligomers in both acetone and THF, outperforming many reported OSN membranes in terms of acetone permeance and rejection of styrene oligomers.

With the assist of a special sacrificed layer, a sub-10 nm polyamide nanofilm was prepared by interfacial polymerization.⁴⁹ Usually, a film with such low thickness is too weak to be fabricated onto a porous support directly. A layer of nanostrand was added onto an ultrafiltration membrane to support the fabrication of the thin film. The nanostrand layer was dissolved by an acid later and the polyamide film was placed onto the ultrafiltration membrane. The polyamide TFC was flexible, stable and robust. An 8 nm freestanding thin film was obtained. The polyamide membranes showed rejection over 90% to dyes with molecular weight of 246 g/mol or higher. Similar with other polyamide membranes that could be activated by DMF, the polyamide thin film also showed improved solvent permeance ($52.22 \text{ L m}^{-2}\text{h}^{-1}\text{bar}^{-1}$) after treatment with DMF.

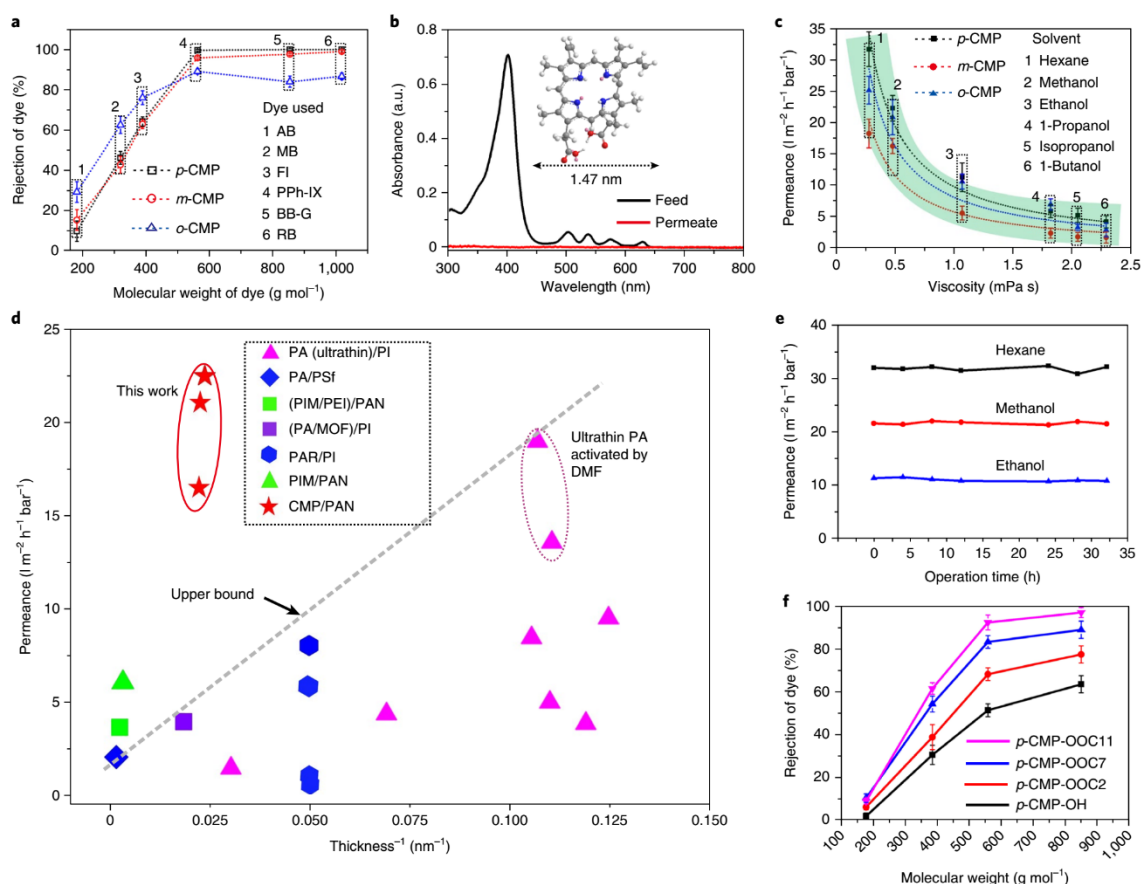


Figure 9. Nanofiltration performances of *p*-CMP, *m*-CMP and *o*-CMP membranes. **a**, Rejection behaviour of different CMP membranes versus the molecular weight of various dyes in ethanol; **b**) ultraviolet visible absorption spectra of PPh-IX dye in methanol to evaluate the separation performance of the *p*-CMP membrane; **c**) plot of solvent permeance through different CMP membranes against the solvent viscosity; **d**) permeance for methanol versus the reciprocal membrane thickness for *p*-CMP, *m*-CMP and *o*-CMP; **e**) plot of hexane, methanol and ethanol permeances with time for *p*-CMP membranes; **f**) rejection behaviour of post-modified *p*-CMP-OH membranes by different moieties. Reproduced from Liang, B.; Tang, Z. et al., *Nat. Chem.* 2018, 10, 961.⁷ With permission from Springer Nature.

Recently, crosslinked polymers with high microporosity, such as COFs^{3,44,71} and CMPs^{7,72}, have been used for porous OSN membranes. These polymers are advantageous due to rigid backbones, high cross-linking density, and narrow pore size distribution. CMP membranes were prepared by a surface-initiated carbon-carbon coupling reaction.⁷ *p*-CMP, *m*-CMP, and *o*-CMP membranes with BET surface areas in the range of 383 ~ 593 m²/g were synthesized with 1,4-dibromobenzene, 1,3-dibromobenzene, and 1,2-dibromobenzene, respectively. With thickness of only 40 nm, CMP membranes showed ultrafast solvent permeance (22.5 L m⁻²h⁻¹bar⁻¹ for methanol) and MWCO of 562 g/mol (**Figure 9**). It is worthy to notice that less ordered *o*-CMP membranes exhibited less selectivity to dyes. *p*-CMP membranes with ordered packing showed both highest selectivity to dyes and highest solvents permeance among CMP membranes. By comparing with other published work, a conclusion was obtained that porous polymer membranes demonstrated better intrinsic permeability (product of permeance and membrane thickness) than that of dense polymer membranes.

Few COFs possess pore size smaller than 2 nm due to the long building blocks in frameworks. However, the ordered crystalline porous structure ensures the narrow pore size distribution to be ideal materials for OSN applications. Banerjee et al. prepared COF films as thin as 90 nm by interfacial polymerization.⁷¹ Although the membranes used in OSN tests were much thicker, high solvent permeance was obtained. The COF membranes showed good selectivity towards dyes with different molecular weight and good recyclability. In another work of COF membranes, a few layers of 2D COF were fabricated in to membranes.⁴⁴ Each layer of 2D COF was as thin as 2 nm. The COF membranes based

on 15-30 layers of 2D COF showed methanol permeance of $106 \text{ L m}^{-2}\text{h}^{-1}\text{bar}^{-1}$ and MWCO of 915 g/mol.

1.5 Separation Application: Water/Oil Separation

All oily wastewater goes into the ocean eventually causing an environmental crisis. The largest source comes from natural oil seeping, which is mostly biodegraded by microbials in the deep ocean. The second largest source is the operational discharge from ships, more specifically, the bilge water that contains oil leaked from engines. Oil spill accidents are the third largest oil source. The oil leaked from transportation makes up 35% of all oil in ocean.⁷³ They are disastrous for the economy, environment, and ecology. Conventional processes to clean the oil spill include mechanical extraction, burning, bioremediation, etc.⁷⁴ Water/oil separation could also be achieved by nanofiltration or reverse osmosis based on size exclusion principle.⁷⁵ However, the filtration rate is low because the viscosity of oil is much higher than that of solvents. Instead, water/oil separation depending on wettability of materials, such as hydrophobicity, hydrophilicity, lipophobicity, oleophilicity, is much more efficient.^{74,76} These materials could be classified into two categories: hydrophobic–oleophilic materials and hydrophilic–oleophobic materials. They are also called oil removing materials and water removing materials, respectively.

For oil removing materials, two types of techniques have been used: membrane filtration and oil adsorption. Common materials used for oil adsorption are porous materials including inorganic materials, synthetic polymers and natural materials. If the

sorption materials could transfer the oil from liquid state to solid state by adsorption, it will facilitate the water/oil separation.⁵ The separation efficiency is determined by hydrophobicity of the sorption materials.

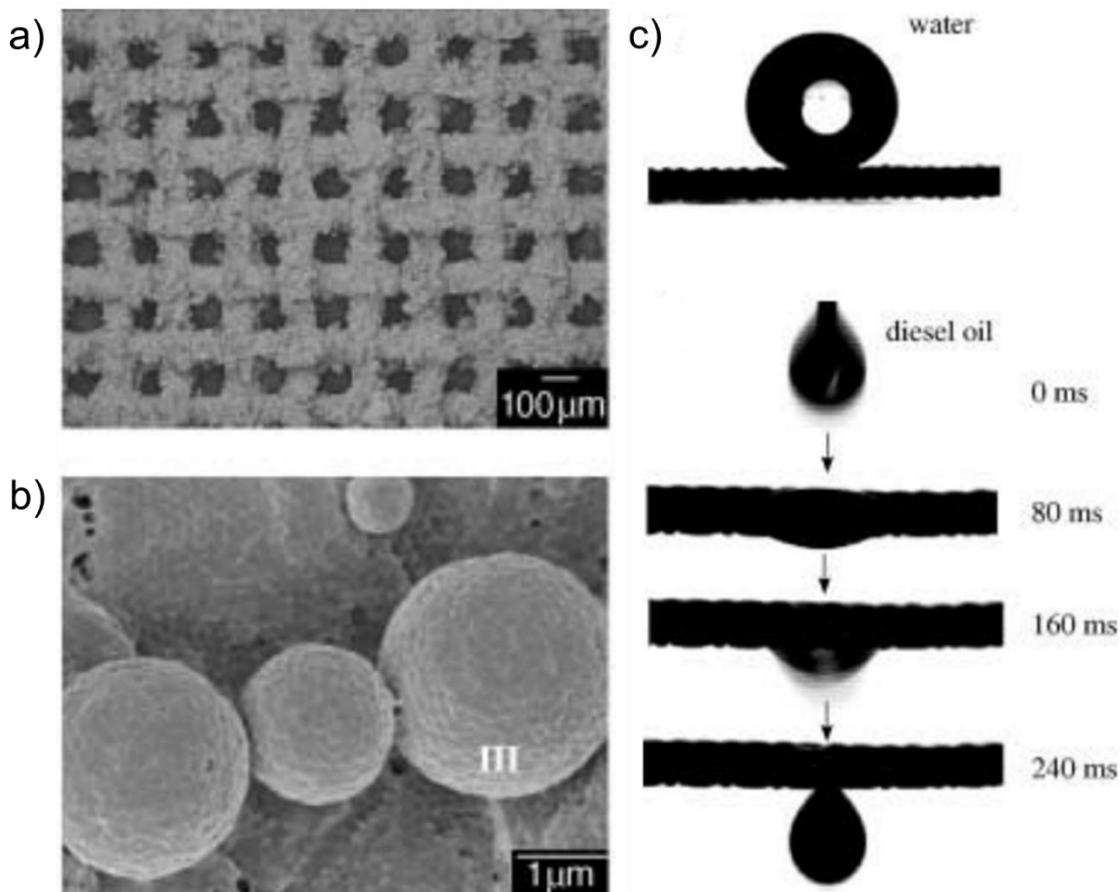


Figure 10. PTFE coated mesh with superhydrophobic and superoleophilic properties. SEM pictures showed morphology of a) coated mesh and b) ball-like PTFE sphere; c) water contact angle and diesel oil contact angle of PTFE mesh. Reproduced from Feng, L.; Zhu, D. et al., *Angew. Chem. Int. Ed.* 2004, 43, 2012.⁵ With permission from John Wiley and Sons.

Many people have been inspired by the work of Feng et al.⁵ with an efficient water/oil separation membrane composed of a stainless steel mesh coated with PTFE. A homogenous emulsion containing PTFE, adhesive, and surfactant was spray coated onto a mesh with pore size of 115 μm (**Figure 10**). The coated PTFE film exhibited ball-like morphology with diameter ranging from 2 ~ 5 μm . The surfaces of PTFE particles were filled with craterlike nanostructure around 70 nm. Such rough surfaces elevated the water contact angle (WCA) of PTFE from 121° to 156°, while decreased the contact angle of diesel oil from 11° to 0°. The PTFE coated meshes became superhydrophobic and superoleophilic rejecting water and permeating oil.

Water removing materials with hydrophilic and oleophobic surfaces are advantageous in many aspects. First, they prevent fouling issues from dirty oil, which have been a formidable challenge for oil removing materials. Second, water is heavier than most oil and sits at the bottom of water/oil mixture. Water block the path of oil transportation. Furthermore, water permeation is more efficient than oil permeation in cases such as fuel purification. However, the hydrophilic and oleophobic materials do not exist in nature and are expensive to produce.⁷⁷

In practical application, waste oil/water mixture emitted from engines or plants usually contains bulky impurities at elevated temperature. Oil removing membranes with hydrophobic coating integrating cost-effectiveness, anti-scratching, and thermal stability are highly desired. Such a challenge will be addressed in Chapter 4.

CHAPTER II

COST EFFECTIVE SYNTHESIS AND SOLUTION PROCESSING OF POROUS
POLYMER NETWORKS THROUGH METHANESULFONIC ACID MEDIATED
ALDOL TRIPLE CONDENSATION*

2.1 Introduction

Bottom-up synthesized microporous materials, such as metal–organic frameworks (MOFs),^{78,79} covalent organic frameworks (COFs)^{80,81} and porous polymer networks (PPNs),⁸²⁻⁸⁵ are promising candidates for gas storage,⁸⁶ catalysis⁸⁷⁻⁸⁹, sensing⁹⁰, environmental remediation,^{21,32} and molecular/ion separation.^{4,79,91,92} Among them, non-crystalline PPNs are usually constructed by irreversible cross-coupling of multi-functional monomers.^{84,93-96} The kinetically formed, conjugated rigid backbones of PPNs endow them with permanent porosity and extraordinary stability, in contrast to the crystalline frameworks (such as MOFs and COFs) that are built through dynamic bond formation.^{89,97} PPNs are therefore more suitable for processes and operations under harsh conditions. The large-scale production and applications of PPNs, however, still confronts two major challenges: (i) Most of the commonly used reactions for highly porous PPN syntheses require expensive metal catalysts/reagents and demanding operation procedures, adding cost and risk to potential mass production; (ii) The insoluble and cross-linked nature of

* Reprinted with permission from “Cost-effective synthesis and solution processing of porous polymer networks through methanesulfonic acid-mediated aldol triple condensation” Guo, Z.-H.; Wang, C.; Zhang, Q.; Che, S.; Zhou, H.-C.; Fang, L. *Mater. Chem. Front.* **2018**, 2, 396. Copyright 2018 The Royal Society of Chemistry.

PPNs often prohibits feasible processing of these materials into forms relevant to practical applications, such as thin films and composites.⁹⁸⁻¹⁰⁰

In this context, synthetic methods¹⁰¹⁻¹⁰³ that allow for mass production and feasible solution-processing are in urgent demand for wider practical applications of PPNs. In order to achieve these objectives, several design principles should be followed: (1) The PPN backbone should be composed of rigid aromatic sp^2 bonds, which give rise to persistent porous architecture as well as high chemical and thermal stability. (2) The starting materials, reagents/catalysts, and solvents should be of low cost and environmentally benign while the reaction should tolerate the exposure to moisture and air. (3) Liquid-phase reaction with minimum number of reagents/catalysts is preferred, so that the reaction mixture could be used directly as the precursor for solution processing. Only a few literature examples could meet all the three requirements.^{104,105} We report herein a cost-effective, scalable synthesis of PPNs through aldol triple condensation reaction. It offers a green strategy for the mass production of highly stable PPNs that are able to adsorb organic molecules quickly and selectively, meanwhile enables solution-phase processing of these materials into microporous composite for advanced applications.

2.2 Synthesis

It was reported in 1991¹⁰⁶ that tandem aldol triple condensation (ATC) reaction can convert 3 acetyl groups into a benzene ring under acidic condition, through two aldol condensations followed by [3+3] electrocyclic reaction and aromatization. Due to its high

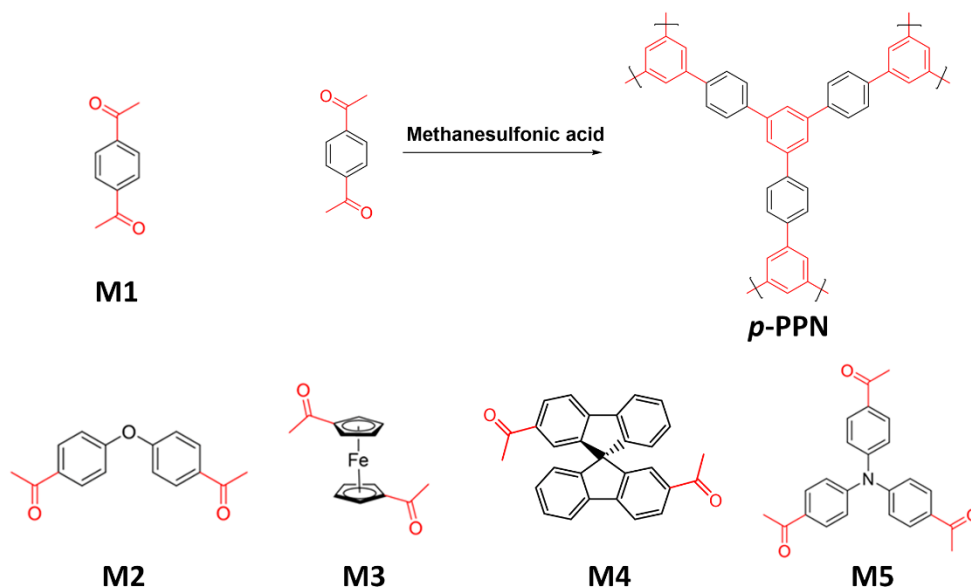


Figure 11. Structural formula of the monomers M1 - M5 and methanesulfonic acid catalyzed ATC reaction for *p*-PPN.

efficiency and the C₃ symmetry of the products, ATC has been widely used in the synthesis of star-shaped molecules^{107,108} and dendrimers¹⁰⁹. Recently, this reaction was also employed in the preparation of organic microporous materials.¹¹⁰⁻¹¹³ In these reported reactions, however, either expensive reagents were used or the acids were easily decomposed under the reaction condition.^{106,111-113} Furthermore, most of these methods required air-tight procedures to protect the reaction from oxygen and moisture. Therefore, large-scale ATC synthesis of PPN was still limited, not to mention the desired feasible solution processing of composite membranes. We envisioned that methanesulfonic acid (MSA) could be an ideal liquid medium for the ATC reactions. MSA is non-toxic and thermally stable under 150 °C.^{114,115} Meanwhile, the inexpensive and environmentally benign nature of MSA allows it to serve not only as the reagent but also as the solvent for ATC reactions and solution-processing.

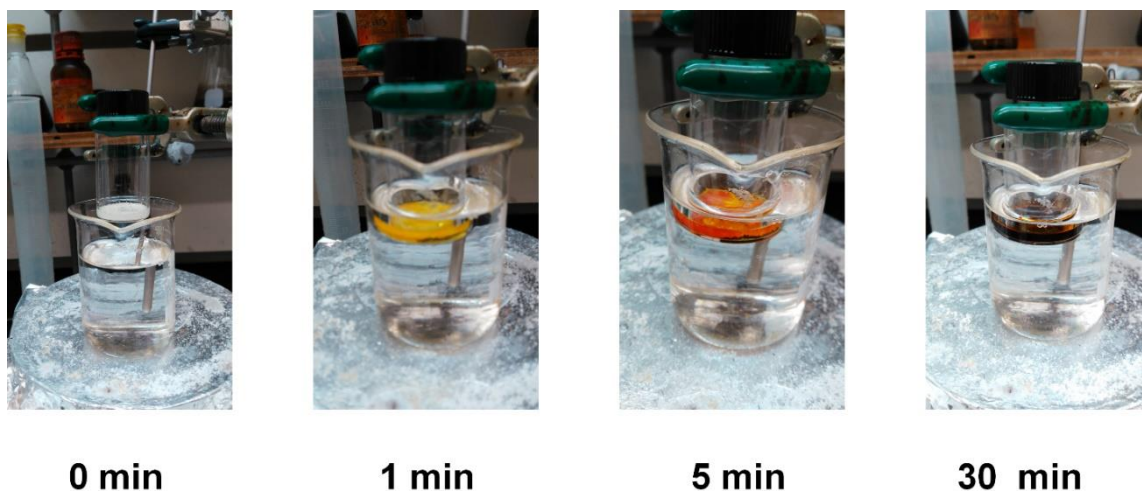


Figure 12. Photos of reaction process for *p*-PPN synthesis.

In a model reaction on acetophenone, ATC reaction was conducted at 130 °C with catalytic amount of MSA (0.2 eq) without additional solvent or reagent. The product 1, 3, 5-triphenylbenzene was isolated in 86% yield. Compared to previously reported ATC reactions and commonly used metal catalyzed cross-coupling reactions, this method was highly efficient, easy to handle, and free of solvent. In this context, PPN syntheses were conducted using aromatic monomers (M1 ~ M5, **Figure 11**) functionalized with multiple acetyl groups by this MSA mediated ATC method.

The ATC polymerization of 1,4-diacetylbenzene (M1) was first carried out as a model (**Figure 11**). M1 was suspended in MSA (10 eq) in an open reaction vessel. Upon heating for several minutes, a homogenous solution was obtained and the color gradually turned from yellow to orange (**Figure 12**), suggesting that the ATC reaction started to afford an extended conjugated π -system. After heating for 12 hours and work up, an insoluble red solid (*p*-PPN) was isolated. The yields for *p*-PPN, PPN3, PPN4 and PPN5 were almost quantitative, ranging from 90% to 99%. The yield of PPN2 was relatively

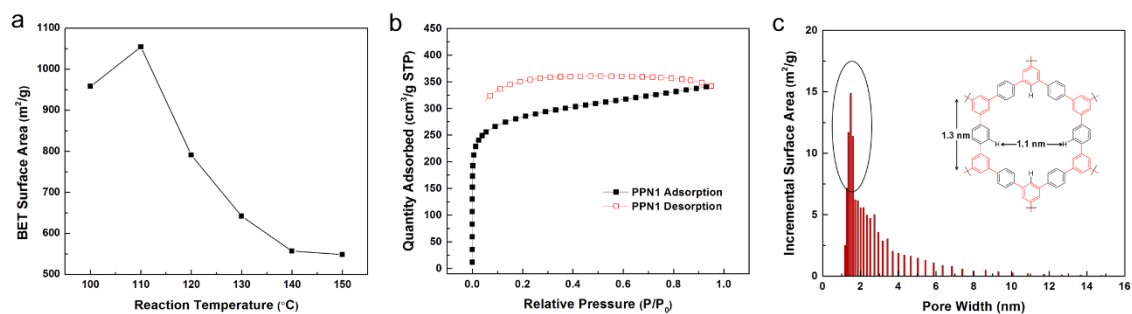


Figure 13. a) BET surface areas of *p*-PPN synthesized at different reaction temperatures; b) 77 K N₂ sorption isotherms and c) Pore size distribution of the *p*-PPN sample synthesized at 110 °C.

low, ranging from 60%-80%, due to instability of the ester group in acidic condition. It was important to note that no extra protective procedure was needed during the entire procedure, demonstrating the insensitive nature of MSA mediated ATC reaction to oxygen or moisture.

2.3 Characterization

A series of samples of *p*-PPN were produced at different reaction temperatures ranging from 100 to 150 °C. N₂ adsorption-desorption isotherm measurements at 77K and Brunauer-Emmet-Teller (BET) surface area analysis were conducted on these samples to screen the reaction conditions for high porosity. The BET surface area obtained at different reaction temperatures are shown in **Figure 13c**. An optimized BET surface area of 1054 m²/g was obtained at a reaction temperature of 110 °C, representing the highest value among PPNs synthesized by ATC methods.^{111,113,116} At lower temperature, the reaction rate was slow and the solubility of reaction intermediates were poor, leading to a lower conversion and hence lower porosity in the product. Above 110 °C, the monotonous

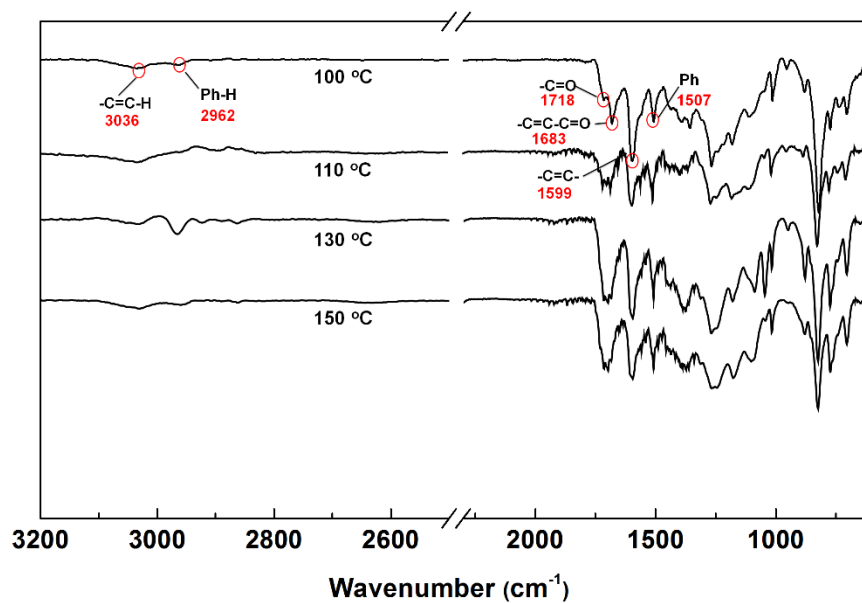


Figure 14. FT-IR spectroscopy of *p*-PPN samples obtained from different reaction temperatures (100 °C, 110 °C, 130 °C and 150 °C).

decrease of BET surface areas of the products was attributed to the formation of defects: under higher temperature, the microporous network grew too quickly so that more defects were formed to lower the microporosity⁸⁴. With the optimized reaction temperature of 110°C, pore volume of the product was 0.42 cm³/g. Pore size distribution analysis (**Figure**

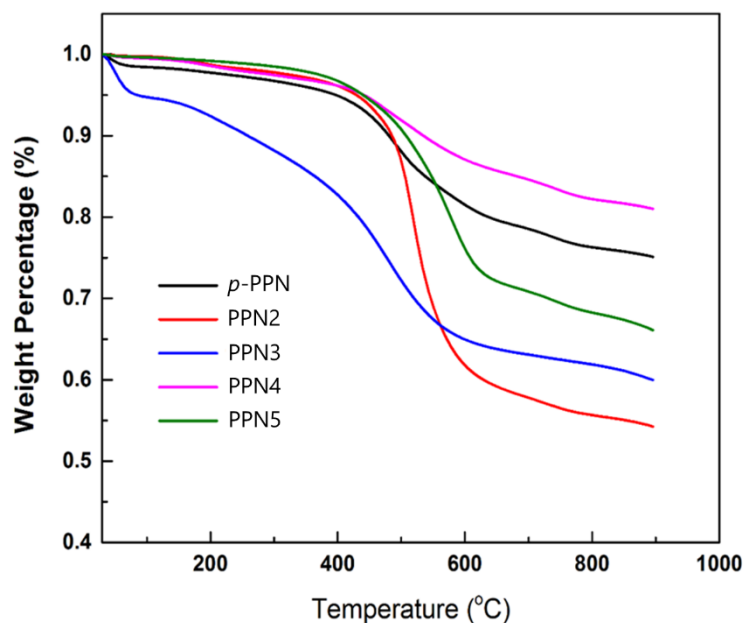


Figure 15. TGA traces of PPNs.

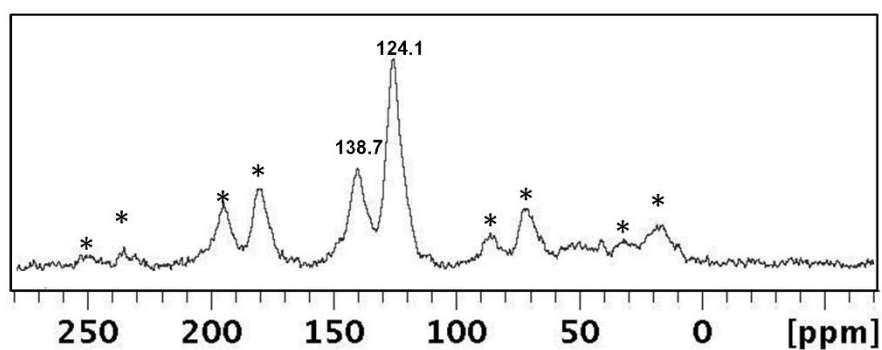


Figure 16. ^{13}C CP/MAS NMR spectra of the *p*-PPN (from 110 °C reaction temperature) recorded at magic-angle spinning (MAS) rate of 5 kHz, asterisks (*) indicate rotational sidebands.

13 c) showed that the majority of the pores were with diameters in the range of 1 ~ 2 nm, matching the theoretically calculated diameter of the smallest repeating cyclic structure. A small amount of larger pores (<10 nm) also presented, likely a result of the kinetically trapped defects in this sample.

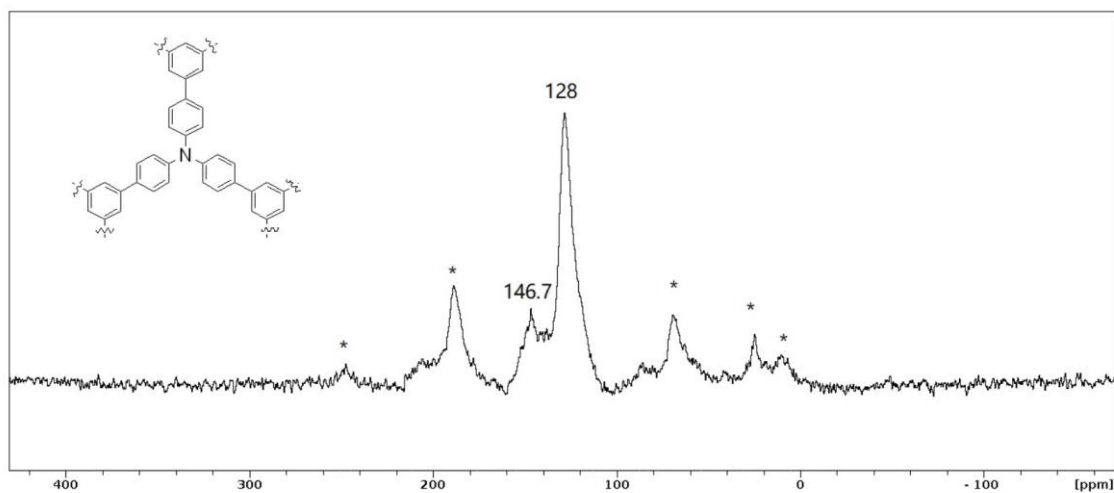


Figure 17. ^{13}C CP/MAS NMR spectra of the PPN5 recorded at a rate of 5 kHz, asterisks (*) indicate rotational sidebands. The major two signals at 146.7 ppm and 128 ppm correspond to the carbon connected to nitrogen and other aromatic carbons, respectively.

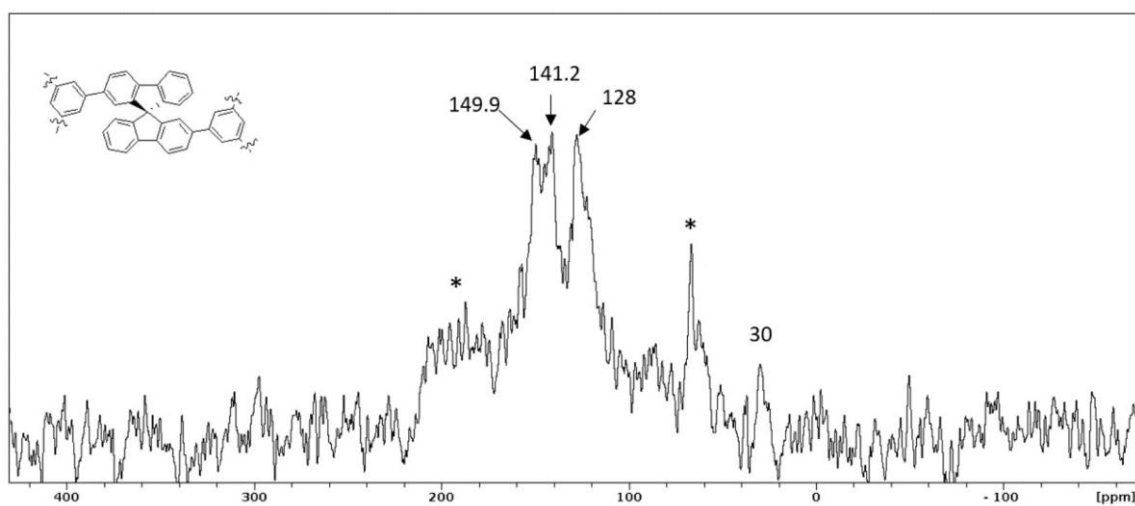


Figure 18. ^{13}C CP/MAS NMR spectra of the PPN4 recorded at a rate of 5 kHz, asterisks (*) indicate rotational sidebands. the signals at 149.9 ppm and 141.2 ppm correspond to substituted aromatic carbons, the signal at 128 ppm corresponds to unsubstituted aromatic carbons. The signal at 30 ppm corresponds to the carbon at

the center of spirofluorene. Note that the signal/noise ratio of was still low despite 27,000 scans.

The structure of *p*-PPN was also investigated with FT-IR spectroscopy (**Figure 14**). There were two peaks around 1700 cm⁻¹ corresponding to the carbonyl stretching of unreacted acetyl (1718 cm⁻¹) and α , β -unsaturated ketone (1683 cm⁻¹). For the *p*-PPN formed at a lower temperature (100 °C), the stronger peak at 1718 cm⁻¹ indicated that a larger fraction of the acetyl groups were unreacted due to the relatively lower conversion. At higher temperatures, the signal of acetyl stretching was weakened significantly while the intensity of the α , β -unsaturated ketone peak increased, giving rise to a broad peak centred at around 1700 cm⁻¹. The relative intensity of the benzene stretching peak (1507 cm⁻¹) compared to

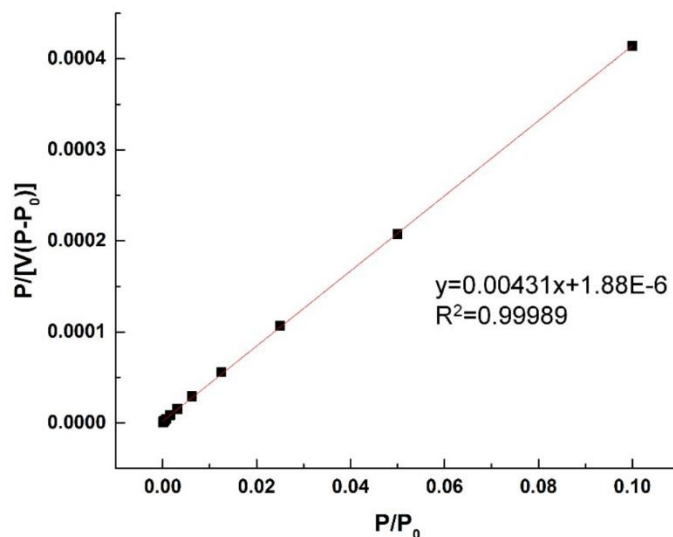


Figure 19. Plot of the linear region on the N₂ isotherm of *p*-PPN sample synthesized at 110 °C for BET

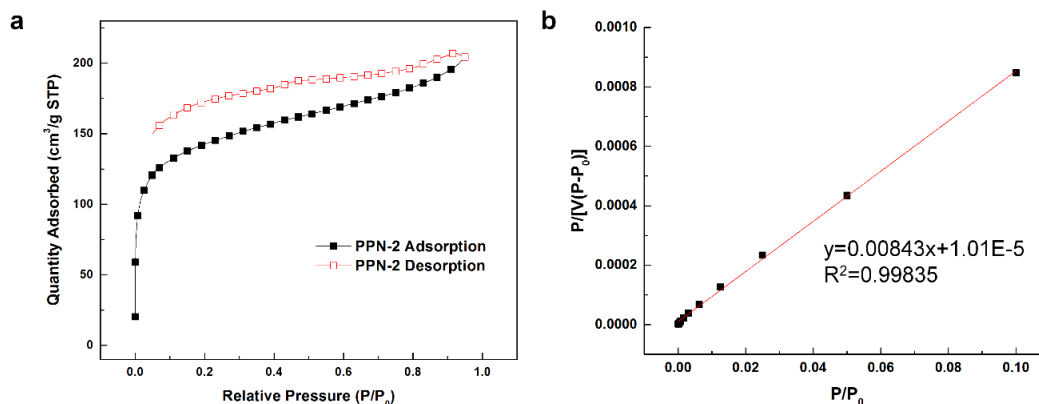


Figure 20. (a) N₂ Adsorption Isotherms of PPN2 at 77K; (b) plot of the linear region on the N₂ isotherm of PPN2.

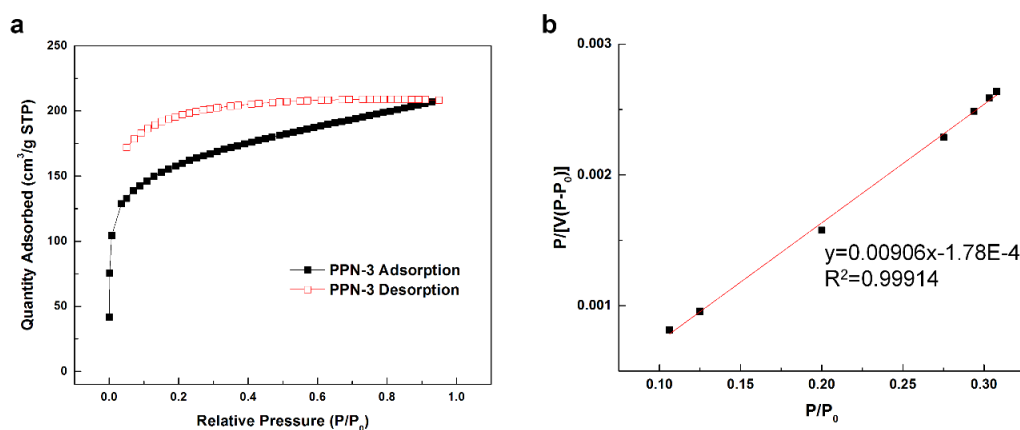


Figure 21. (a) N₂ Adsorption Isotherms of PPN3 at 77K; (b) plot of the linear region on the N₂ isotherm of PPN3 for BET.

that of the broad peak at 1700 cm⁻¹ was firstly increased from 100 °C to 110 °C then decreased from 110 °C to 150 °C, indicating that 110 °C was the optimized temperature for highest conversion and lowest defect level. These results agreed well with the BET surface area measurements (**Figure 13a**) and the corresponding hypothesis. In addition, solid-state ¹³C CP/MAS NMR spectroscopy (**Figure 16**) revealed two major signals

(138.7 and 124.1 ppm) corresponding to unsubstituted aromatic carbons, substituted benzene carbon, respectively, agreeing with the proposed backbone

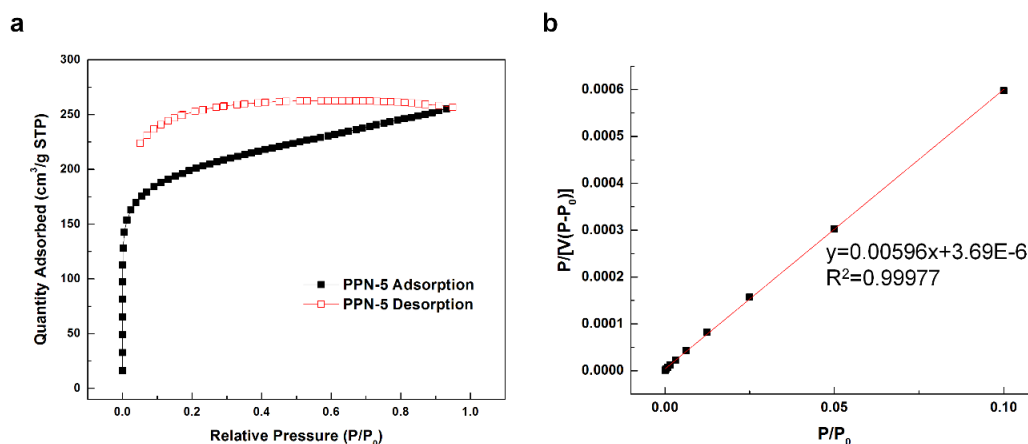


Figure 22. (a) N₂ Adsorption Isotherms of PPN5 at 77K; (b) plot of the linear region on the N₂ isotherm of PPN5 for BET.

Table 1. Surface area and pore volume of PPNs, and the CFP/*p*-PPN composite.

Microporous polymer	Monomer	S _{BET} (m ² /g) ^[a]	V _{Micro} (cm ³ /g) ^[b]	V _{total} (cm ³ /g) ^[c]
<i>p</i> -PPN	M1	1054	0.28	0.42
PPN2	M2	515	0.04	0.20
PPN3	M3	699	0.04	0.25
PPN5	M5	729	0.17	0.31
CFP/ <i>p</i> -PPN	M1	216	N/A	N/A

[a] Surface area calculated from N₂ adsorption-desorption isotherm at 77K using the BET method. [b] Micropore volume calculated from N₂ adsorption isotherm using the t-plot method. [c] Total pore volume at P/P₀ = 0.97

Table 2. Results of the elemental analysis of PPNs.

	C(%)	H(%)	N(%)	O(%)
<i>p</i>-PPN (experiment)	84.64	4.95	N/A	10.41 ^a
<i>p</i>-PPN (theoretical)	95.21	4.79	0	0
PPN2 (experiment)	79.91	5.14	N/A	14.95 ^a
PPN2 (theoretical)	88.05	4.62	0	7.33
PPN3 (experiment)	71.23	4.92	N/A	N/A
PPN3 (theoretical)	71.85	4.31	0	0
PPN4 (experiment)	85.70	4.78	N/A	9.52 ^a
PPN4 (theoretical)	95.57	4.43	0	0
PPN5 (experiment)	81.55	4.98	3.98	9.49 ^a
PPN5 (theoretical)	90.82	4.76	4.41	0

a. Estimated from C, H and N atoms

constitution of *p*-PPN (**Figure 11**). Due to the low sensitivity of this method, however, the expected peaks corresponding to defects, such as acetyl group and α , β -unsaturated ketone, were not identifiable. In contrast, elementary analysis (**Table 2**) showed trace amount of oxygen left over in *p*-PPN, corresponding to the unreacted defects.

PPN2 to PPN5 were synthesized from monomers M2~M5 under the optimized condition (**Table 1**). The BET surface areas of PPN2, PPN3 and PPN5 were lower than that of *p*-PPN. The decrease in porosity was attributed to (i) the higher flexibility of these monomer, and (ii) network interpenetration due to their longer molecular lengths.⁷ PPN4 showed extremely low porosity, likely because of the bulkiness of the spirofluorene that filled up the pores. N₂ sorption isotherms for *p*-PPN, 2, 3 and 5 at 77K (**Figure 13b**, **Figure 19-22**) all showed high gas uptake at low relative pressures and a flat course in the intermediate section, representing typical Type I adsorption-desorption isotherms. Thermogravimetric analyses (TGA) (**Figure 15**) demonstrated good thermal stability of *p*-PPN, PPN2, PPN4, and PPN5 with decomposition temperature over 400 °C, owing to the robust nature of their rigid sp² rich backbones. The only exception, PPN3, showed a distinctive weight loss before 200 °C, likely a result of the lower intrinsic thermal stability of the ferrocene unit.¹¹⁷ The morphology of PPNs powder samples were studied using SEM (**Figure 23**). *p*-PPN and PPN3 showed bulky structure while PPN2 and PPN4 showed nanoparticles morphology. PPN5 showed relatively smooth morphology.

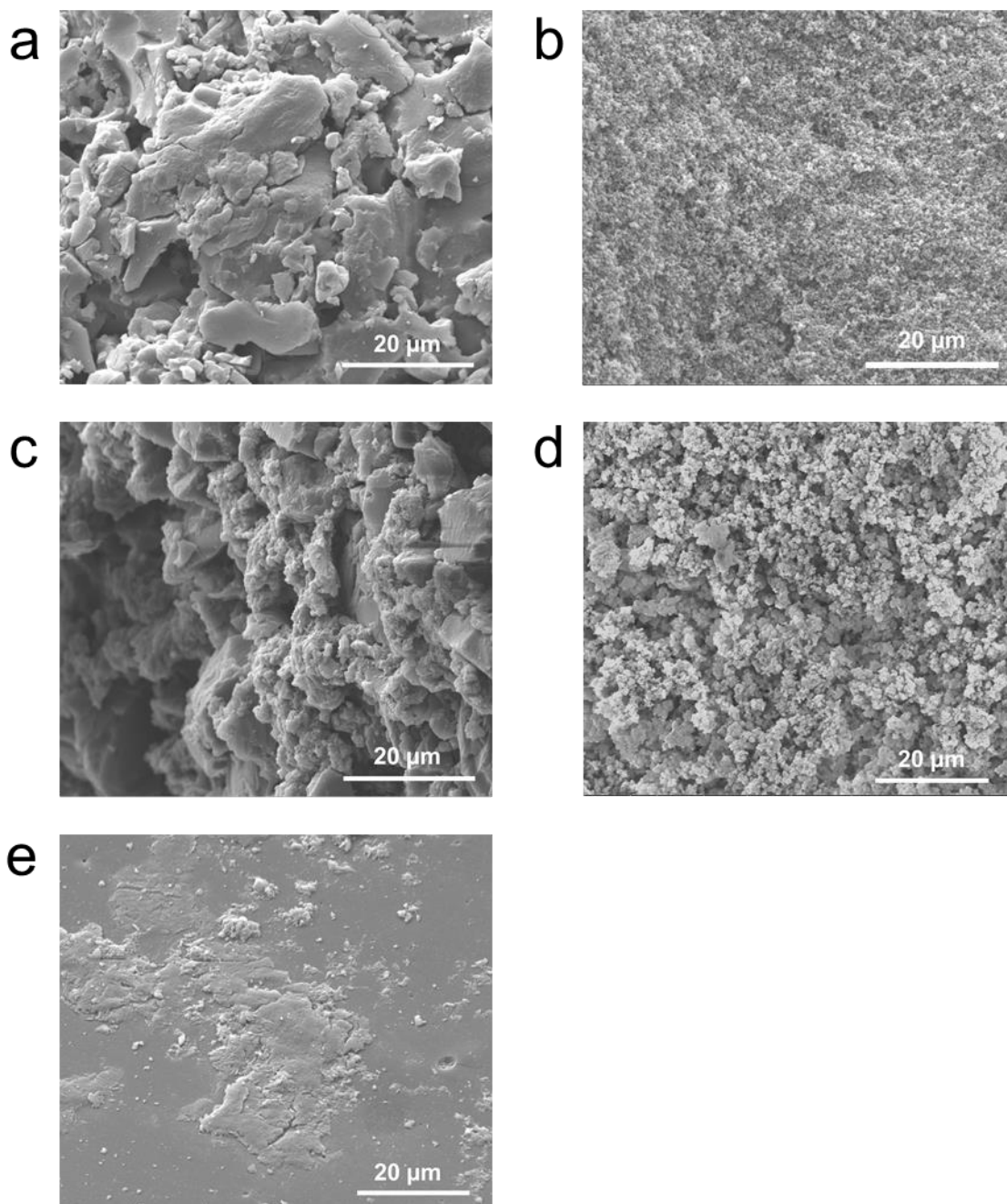


Figure 23. SEM pictures showed morphology of powder samples of a) *p*-PPN, b) PPN2, c) PPN3, d) PPN4, e) PPN5.

2.4 Selective Adsorption

Despite the amorphous nature of *p*-PPN, the large pore volume and narrow pore size dispersion promises its application in size-selective adsorption of molecular solutes in solution.^{4,118,119} To test the efficiency and selectivity of *p*-PPN in adsorbing organic molecules, aqueous solutions of organic compounds (15-23 ppm in 4 mL water) with

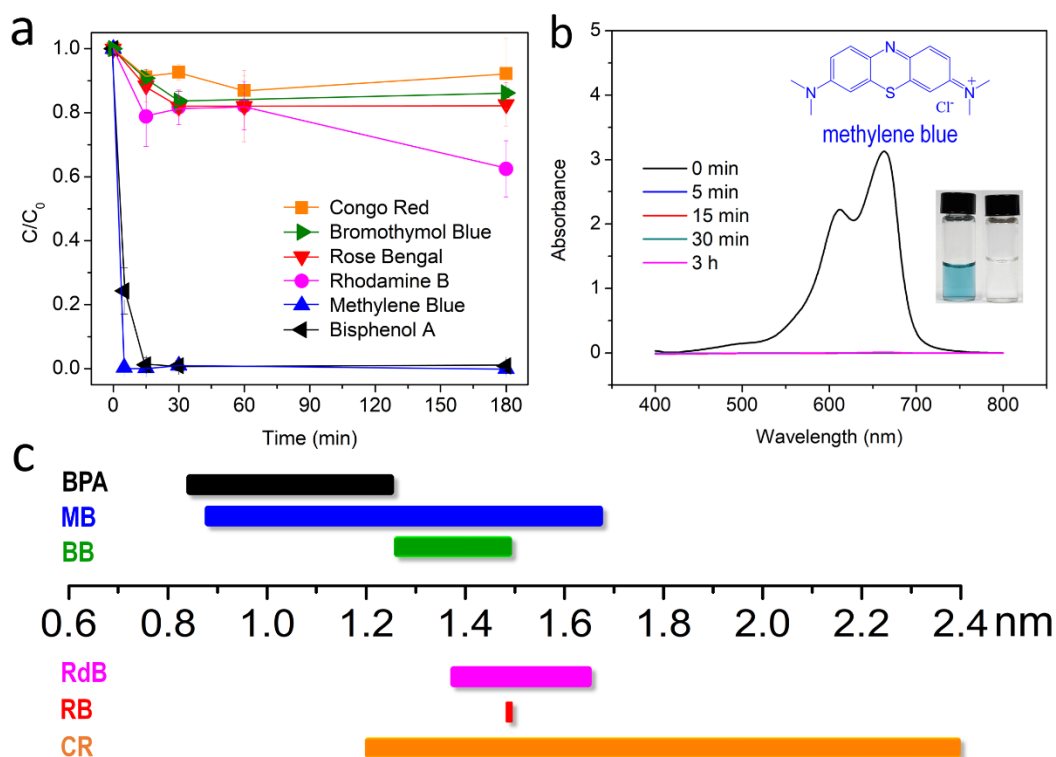


Figure 24. (a) Plot of relative concentration changes of different dye solutions versus time upon treating with *p*-PPN; (b) example UV-vis spectra of MB solution at different time after the addition of *p*-PPN, inset shows the photo of MB solution before and 5 min after adsorption process started; (c) molecular sizes of the tested dye molecules, the bars range from the minimal projection diameters to maximal projection diameters of the solutes.

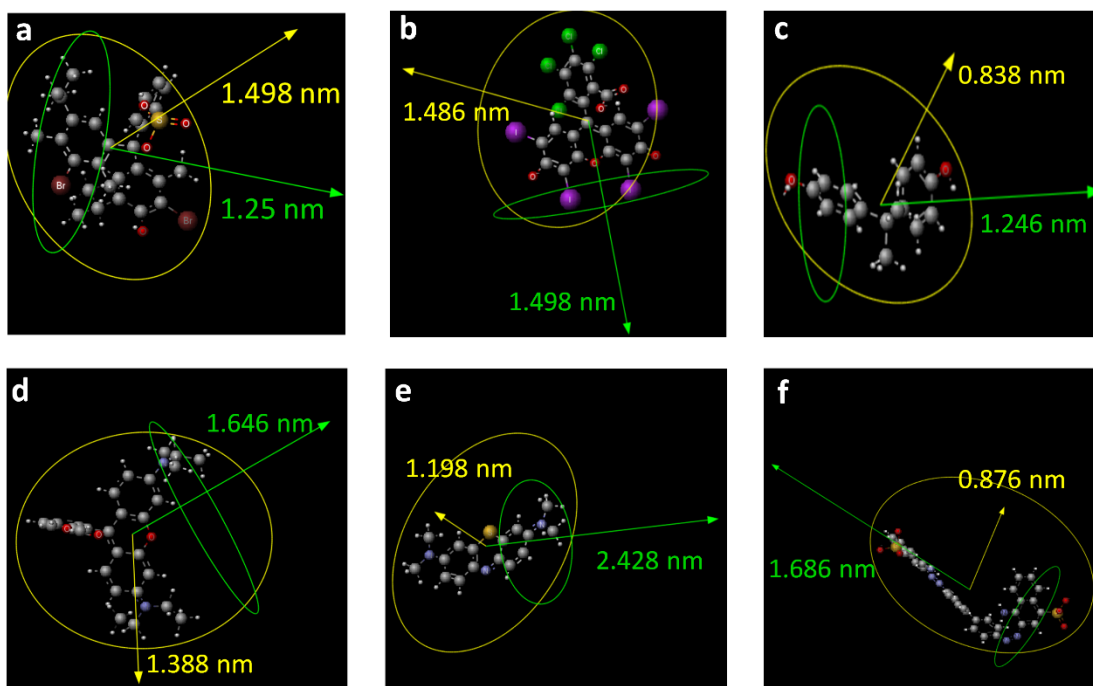


Figure 25. Maximal and minimal projection radius of (a) bromothymol blue, (b) rose bengal, (c) bisphenol A, (d) rhodamine B, (e) congo red, (f) methylene blue.

different Van der Waals size, ranging from 0.8 nm to 2.5 nm (**Figure 24c, 25**), were treated with 10 mg *p*-PPN powder. These organic samples are either dyes or UV absorbing, so that UV-visible absorption spectroscopy can be employed to test the adsorption efficiency (**Figure 24b, 26**). After adding *p*-PPN to the solution, dye molecules with small Van der Waals diameters, such as bisphenol A (BPA) and methylene blue (MB), were fully adsorbed in very short time (5 minutes for MB and 15 minutes for BPA), leading to diminished UV-vis absorption in the solution (**Figure 24a**). In contrast, for rhodamine B (RdB), bromothymol blue (BB), congo red (CR) and rose bengal (RB) that possess Van der Waals diameters matching or larger than the maximum pore size of *p*-PPN, the solution concentration remained at a high level even after 3 hours. The fast adsorption of BPA and

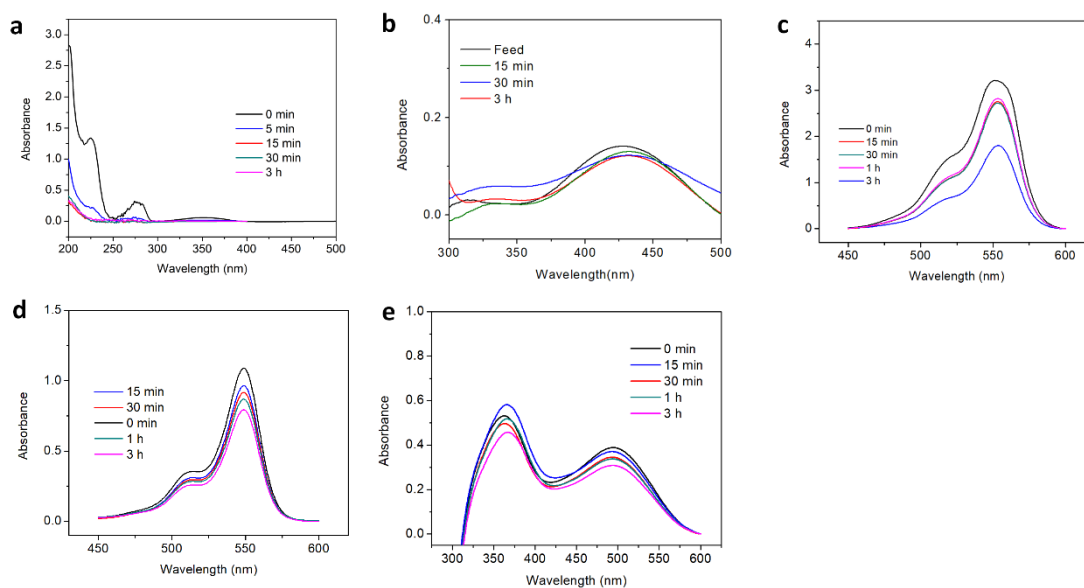


Figure 26. UV-vis spectrum of organic molecules: (a) bisphenol A, (b) bromothymol blue, (c) rhodamine B, (d) rose Bengal, (e) congo red in water absorbed by *p*-PPN

MB by *p*-PPN in mild agitation shows its potential for rapid and selective removal of small organic molecules in water.²¹ Adsorption selectivity of *p*-PPN is comparable with those porous materials containing specific supramolecular receptors^{21,120} and outperformed prevalent commercial porous materials, such as active carbon and zeolite.⁴ These high performances can be attributed to the strong hydrophobicity and the narrow size distribution of the pores in *p*-PPN.⁸⁴ In addition, the fact that the size-selectivity was not sensitive to the charge of the molecules indicated that the selectivity was mainly a result of the size matching effect but not electrostatic interactions. Furthermore, through Langmuir isotherm plot, a high value of maximum adsorption capacity (139 mg/g) of *p*-

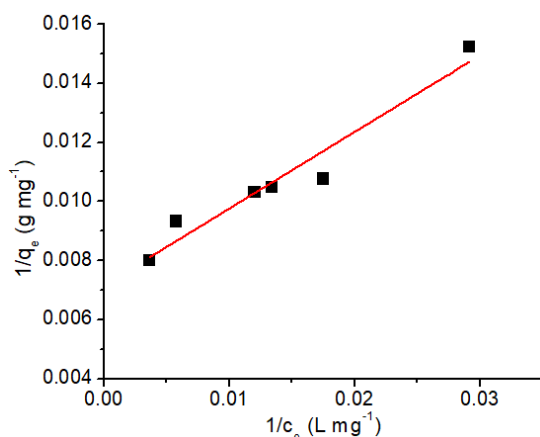


Figure 27. Maximum adsorption capacity of *p*-PPN to methylene blue solution indicated by Langmuir adsorption isotherm.

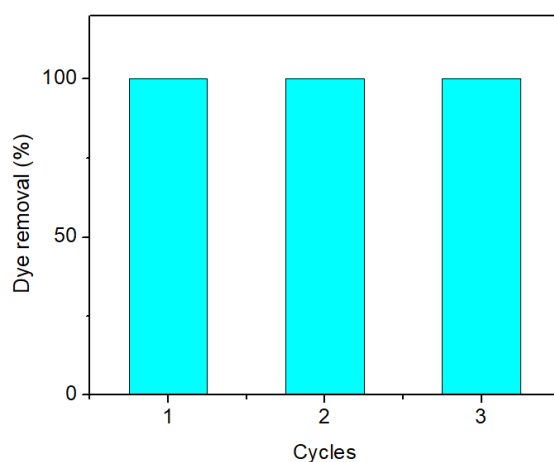


Figure 28. Recycling of *p*-PPN for methylene blue adsorption.

PPN to MB solution was obtained (**Figure 27**). The adsorption capability of *p*-PPN can be feasibly regenerated for at least 3 times, after simply bath sonicating the *p*-PPN in acetone for 10 min at room temperature (**Figure 28**). Although the rigid and cross-linked nature endowed PPNs with excellent stability and solvent resistance, it also means that processing of such materials could be challenging.^{104,121,122} Using MSA mediated ATC

synthesis, however, this problem can be addressed by taking advantage of the pristine nature of the reaction mixture^{104,105}, because no other reagent was added into the reaction

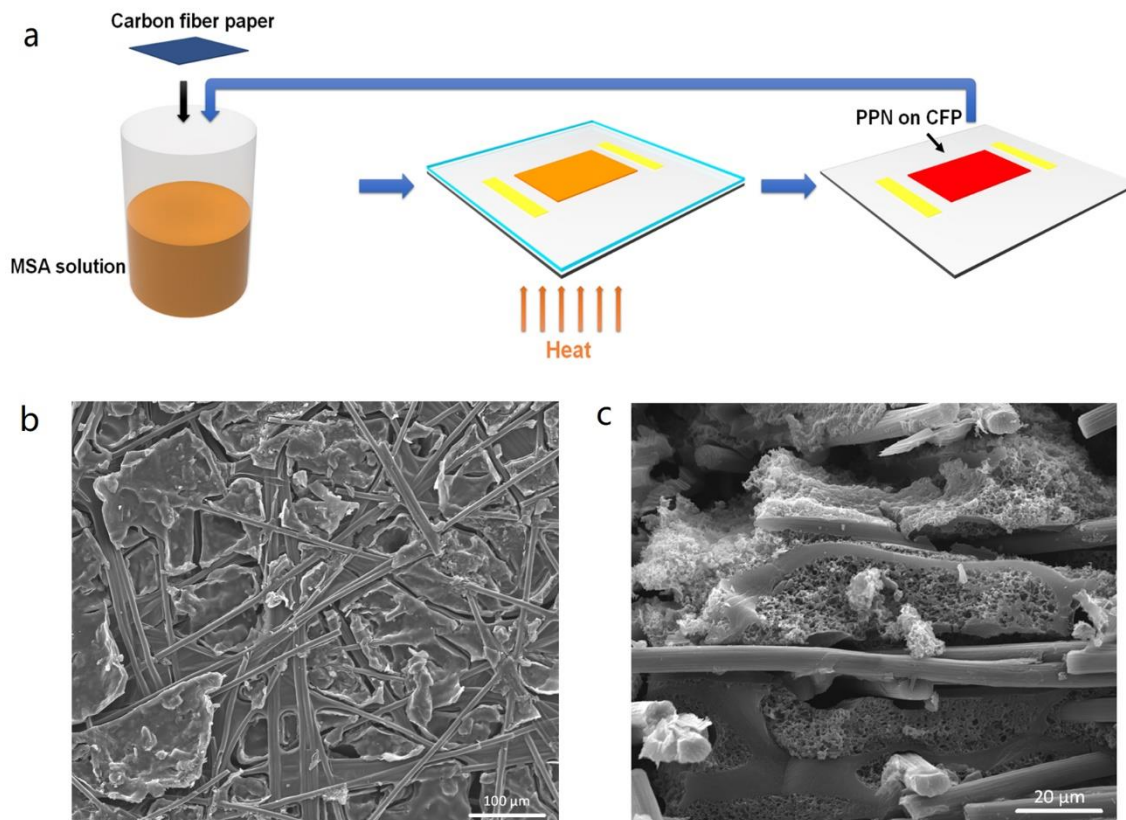


Figure 29. (a) “Soaking-heating-washing” cycles for the fabrication of CFP/*p*-PPN composite membrane; scanning electron microscopy (b) top view and (c) cross-section view of CFP/*p*-PPN composite membrane.

other than MSA. Using this method, it was possible to produce PPN composite with a supporting matrix, to integrate important properties related to practical applications, such as mechanical robustness and electrical conductivity. For example, in-situ ATC reaction of M1 solution in MSA can be performed in the present of carbon fiber paper (CFP), to afford porous *p*-PPN /CFP composite. In this composite, the voids and holes in CFP matrix

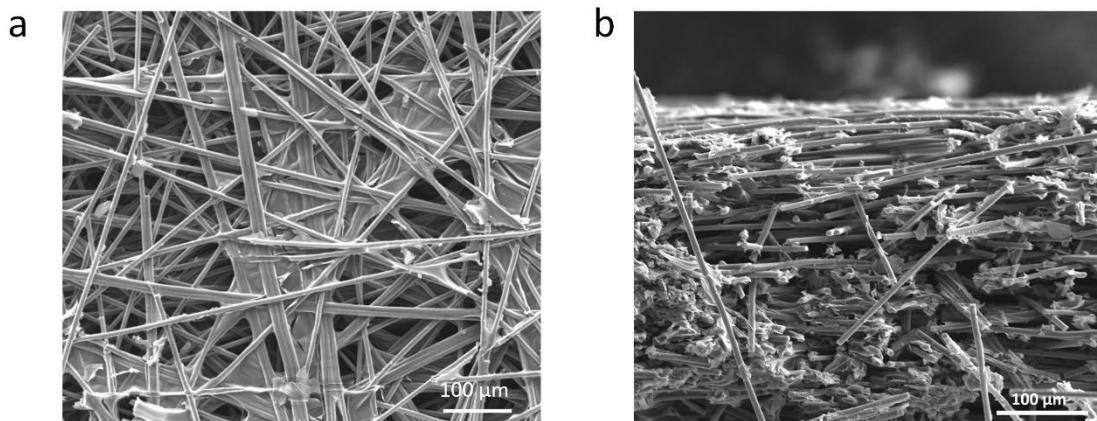


Figure 30. (a) Surface view and (b) cross-section view of CFP.

were filled up with *p*-PPN. In order to fill up all the space in CFP paper, 4 cycles of “soaking-heating-washing” procedure were performed (**Figure 29a**), leading to a 55 % weight increase of the composite after the incorporation of PPN (**Figure 31**). Cross section

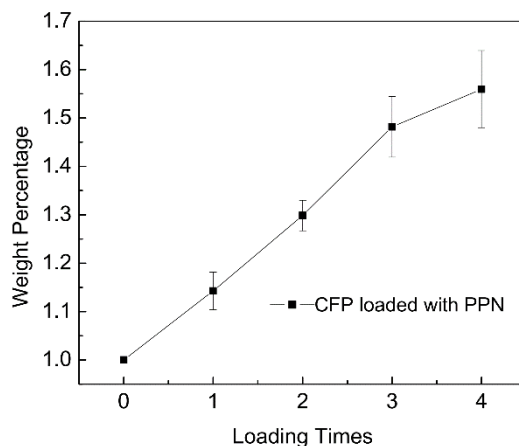


Figure 31. Weight change of CFP/*p*-PPN composite membranes

and top view SEM images of CFP and CFP/ *p*-PPN showed (**Figure 29 b, c, Figure 30**) that the PPN infiltrated deep into the CFP. N_2 sorption isotherm measurement demonstrated the porous nature of the composite (BET surface area $216 \text{ m}^2/\text{g}$) despite the large composition of carbon fiber matrix¹²³ (**Figure 31**). The CFP/ *p*-PPN composite also

possessed an excellent methylene blue removal efficiency (97.7%) (**Figure 32**), although the adsorption kinetics was slower than that of *p*-PPN powder. Overall, this method enables the fabrication of functional PPN products mechanically supported by a strong fiber matrix.

2.5 Conclusion

In summary, cost effective bottom-up syntheses of organic microporous polymer networks were achieved by using methanesulfonic acid mediated aldol triple condensation reaction. This method features low cost, inexpensive starting materials and reagents, as well as simple reaction procedure. The hydrophobic nature and narrow size distribution of

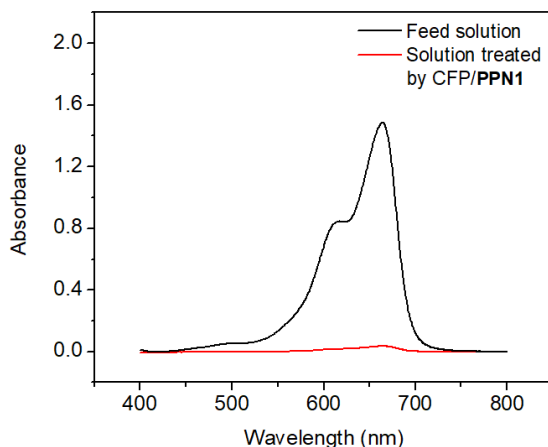


Figure 32. UV-vis spectrum of methylene blue solution treated by CFP/*p*-PPN composite membranes

the pores of the resulting material enabled quick and selective adsorption of organic molecules in aqueous environment. Pristine composition of the reaction precursor allows solution processing of porous composite membranes of this insoluble PPNs through a "soaking-heating-washing" strategy, enable the application of composite PPN materials

with supporting materials. Overall, this work paves the way for large-scale, practical applications of PPN materials for purification, filtration, catalysis and sensing.

2.6 Experimental Section

2.6.1 General Information

M2,¹²⁴ M3,¹²⁵ M4¹²⁶ and M5¹²⁷ were synthesized according to procedure reported in the literature. M1 and other starting reagents were purchased from Aldrich, and Alfa-Aesar, and used as received without further purification. All dye molecules used in adsorption tests were purchased from Aldrich, TCI or The Science Company. The glass substrate was first rinsed by acetone. Subsequently, a thin layer of PTFE (purchased from Miller-Stephenson) was spray-coated on substrate. After that, the substrate was placed in an oven at 315 °C for 1h. Carbon fiber paper (Toray 090) was purchased from Fuelcell store.

Thermogravimetric analysis (TGA) data were collected on Mettler-Toledo TGA-DSC-1 with heating rate 10 °C/min from 30 °C to 900 °C under N₂ atmosphere. Solid state nuclear magnetic resonance (NMR) data were collected on Bruker Advance-400 Solids NMR spectrometer. N₂ adsorption data were collected on a Micrometrics ASAP 2020 accelerated surface area and porosimetry system at 77K. Samples were activated under vacuum at 120 °C for 12h with the activation port equipped on ASAP 2020. Field-emission scanning electron microscopy images were collected on FEI Quanta 600 FE-SEM. UV-vis absorption spectra were recorded on Shimadzu UV-2600 Spectrophotometer. Van del Waals diameters of dye molecules were calculated by MarvinSketch(version 17.23).

2.6.2 Synthesis

1, 3, 5-triphenylbenzene. In a 25 mL round-bottom flask, acetophenone (500 mg, 4.17 mmol) and methanesulfonic acid (80 mg, 0.83mmol) were heated and stirred at 130 °C for 12 h. It was subsequently neutralized by saturated NaHCO₃ and extracted with CH₂Cl₂ (3 × 20 mL). The combined organic layers were dried by MgSO₄, filtered, and concentrated in vacuum. The residue was purified by flash column chromatography (SiO₂, hexane) to give the product as white solid (364 mg, 1.19 mmol, 85.7%).

General procedure of PPN synthesis by MSA catalyzed ATC reaction. To a 20 mL glass vial with cap, the monomer (1 equivalent) and methanesulfonic acid (10 to 20 equivalents) was added and heated at 110 °C for 12 hours. A dark colored monolithic solid was obtained. After washing with water extensively, the solid was washed with ethanol for 24 hours in a Soxhlet extractor. The product was dried under vacuum at 120 °C for 12 hours.

2.6.3 Adsorption Test

In each test, 10 mg *p*-PPN sample was added into 4 mL aqueous solution with organic solute. The concentration of solution was set to be 15 ppm except for that of bisphenol A solution which was 22.8 ppm. The mixture was stirred at 150 r/min using a magnetic stir bar. At different time point, the solution was filtrated by syringe filter for concentration test under UV-vis absorption spectroscopy. The concentration of solution was determined by UV-vis spectrum at a wavelength of absorbance (274 nm for BPA, 663

nm for MB, 432 nm for BthB, 550 nm for RdB, 550 nm for RB, 495 nm for CR). The following equation was used to calculate the percentage of absorbed organic molecules:

$$\text{Absorption percentage} = (C_0 - C_t) / C_0 \times 100\%$$

Each measurement was repeated twice to obtain the standard deviation.

Regeneration of *p*-PPN was achieved by sonication in acetone for 10 mins. The regenerated material was then recovered by filtration for further dye removal test.

Thermodynamic parameters of the adsorption process was studied. Methylene blue solutions with different concentration were treated by *p*-PPN samples. The relationship of the amount of dye absorbed at equilibrium, q_e , (mg g^{-1}), and the residual dye concentration at equilibrium, c_e (mg L^{-1}) was plotted following Langmuir isotherm model:

$$\frac{1}{q_e} = \frac{1}{q_{max}} + \frac{1}{q_{max}Kc_e}$$

where q_{max} (mg g^{-1}) is the maximum adsorption capacity of adsorbent at equilibrium, and K (L mg^{-1}) is the equilibrium constant of the adsorption process.

2.6.4 Carbon Fiber Paper/ p-PPN Composite Membrane Fabrication

A piece of carbon fiber paper (CFP) was soaked in monomer 1 solution in MSA (90 mg/mL), which was then heated at 45 °C for 6 hours to allow the formation of a gel. The soaked CFP was then taken out and the gel on the surface of CFP was wiped off.

After that, this CFP was further heated at 110 °C for 12 h to trigger the in-situ polymerization of PPN inside the voids of CFP. After the reaction was done, this sample was washed by DMF and ethanol. This sample was then soaked in the 1/MSA solution again and heated to 110 °C after 6 hours of pre-treatment. Such “soaking-heating-

washing” cycles were performed for 4 times to reach a reasonable high loading of PPN in the CFP matrix.

The methylene blue removal performance of CFP/ *p*-PPN was evaluated by stirring 10 mg of CFP/ *p*-PPN with 4 mL aqueous solution containing 10 ppm methylene blue for 12 h.

CHAPTER III

AROMATIC POROUS POLYMER NETWORK MEMBRANES FOR ORGANIC

SOLVENT NANOFILTRATION UNDER EXTREME CONDITIONS*

3.1 Introduction

Organic solvent nanofiltration (OSN) through membranes have emerged as an environmentally and energetically favorable strategy to purify, separate, and concentrate organic solutions for a wide range of applications.^{1,8,11,128,129} To date, various types of membranes, including polymeric, inorganic and mixed matrix membranes, have been developed for OSN.^{1,11,128,130-133} Among them, polymeric membranes^{134,135}, especially those ones with high permeability and selectivity^{67,136}, are particularly promising due to their feasible manufacturing, mechanical adaptability, and synthetic versatility. Most commercial polymeric membranes for OSN are dense membranes with low or no porosity^{1,67} and usually suffer from low permeability. Moreover, their non-cross-linked nature also lowers their resistance to strong organic solvents or harsh chemical environments.^{137,138} In contrast, cross-linked porous polymeric membranes are promising in terms of permeability because of the presence of interconnected pores and channels which assist molecular transportation.⁶⁷ Cross-linked membranes also exhibit desired solvent resistance compared to non-cross-linked alternatives.^{139,140} In addition, recently

* Reprinted with permission from “Aromatic porous polymer network membranes for organic solvent nanofiltration under extreme conditions” Wang, C.; Li, C.; Rutledge, E.; Che, S.; Lee, J.; Kalin, A.; Zhang, C.; Zhou, H.-C.; Guo, Z.-H.; Fang, L. *J. Mater. Chem. A*, **2019**, DOI: 10.1039/C9TA10190J. Copyright 2019 The Royal Society of Chemistry.

developed crystalline covalent organic framework (COF) membranes, which are covalently cross-linked and highly porous, have shown excellent selectivity and extraordinary permeance in OSN with various solvents on account of the long range order of their pore structures.^{3,44,71,141-143} In comparison, an amorphous cross-linked porous polymer network (PPN) can be prepared via a wide range of synthetic methods, creating a diverse library of PPNs with different cross-linking chemistries and backbone constitutions.^{82,84,85,144-146} A number of high-performance, PPN-derived OSN membranes have been successfully developed, including polyarylate membranes⁷⁰, cyclodextrin membranes^{68,69}, and conjugated microporous polymer (CMP) membranes.^{7,72}

Despite the significant advances in the field of polymeric OSN membranes, it is still a formidable challenge to achieve an ideal polymeric membrane possessing simultaneously chemical/structural stability, molecular-sieving selectivity, and high permeability/permeance. In particular, the performance and structural integrity of most polymer membranes tend to decline rapidly in harsh chemical environments, which are often unavoidable in practical applications.^{1,11,147-149} Many of the key chemical bonds in polymeric membranes (such as ester bonds, imine bonds) are labile in strong acidic or basic conditions. Highly permeable and selective polymeric OSN membranes that can perform reliably with chemically aggressive feeds are still extremely rare. In order to achieve a stable, selective, and permeable membrane for OSN, one must simultaneously impart good chemical stability, high porosity, and narrow pore size distribution into polymeric OSN membranes.^{147,150,151} We hypothesized that organic membranes

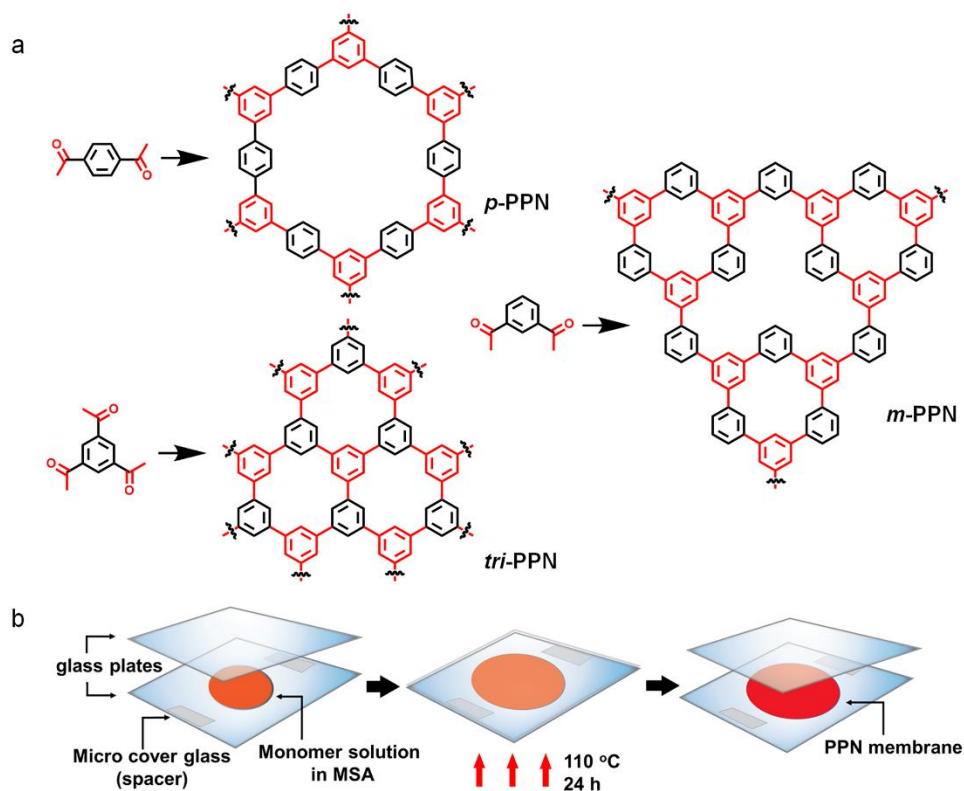


Figure 33. a) Synthetic scheme of cross-linked conjugated PPNs (*p*-PPN, *m*-PPN, and *tri*-PPN) through aldol triple condensation reaction; b) graphic representation of the membrane fabrication using an MSA solution of the monomer.

constituted of a fully aromatic network could potentially fulfil these demands. Herein, we report the fabrication of a class of aromatic PPN membranes possessing extraordinary stability, excellent permeability and molecular-sieving selectivity, as well as highly robust OSN performance in strong acid and base condition.

3.2 Fabrication of PPN membranes

The PPN membranes reported in this work are fabricated by cross-linking using an aldol triple condensation (ATC) reaction. In our previous work, a feasible ATC method

based on methanesulfonic acid (MSA) was developed to efficiently produce amorphous aromatic PPNs in the form of powders with high porosity.¹⁵² In this reaction, MSA acted as both the catalyst and the solvent so that no other reagent is needed for the “pristine” cross-linking. We envisioned that this unique feature could allow for fabrication of PPN membranes through an *in situ* cross-linking procedure using MSA as the solvent. It is also noteworthy that small amount of reaction defects, such as unreacted acetyl groups and α,β -unsaturated ketone units, are unavoidable in the product due to the less than 100% conversion and irreversible nature of the ATC reaction.¹⁵³ Based on this reaction, *p*-PPN, *m*-PPN, and *tri*-PPN membranes were fabricated using pristine solutions of 1,4-diacetylbenzene, 1,3-diacetylbenzene or 1,3,5-triacetylbenzene in MSA solvent, respectively (**Figure 33**). These benzene-derived monomers are all commercially available. They were selected so that the ATC reaction led to PPNs with aromatic backbone with the desired stability and microporosity. The different substitute patterns of para-, meta- and tri-acetyl functionalized monomers allows for the construction of variable pore structure. The reaction yields for *p*-PPN, *m*-PPN, and *tri*-PPN membranes were 88%, 84% and 91%, respectively.

A series of PPN membranes with different thicknesses, ranging from 150 nm to 120 μm , were prepared by this method with excellent quality. The membrane thickness was simply controlled by tuning the concentration of the initial monomer solution and the thickness of the spacer. For example, a membrane with sub-micrometer thickness was prepared from a 15 mg/mL monomer solution with no spacer between the two glass slides. After the heating process, the as-prepared membrane was removed from the glass slide

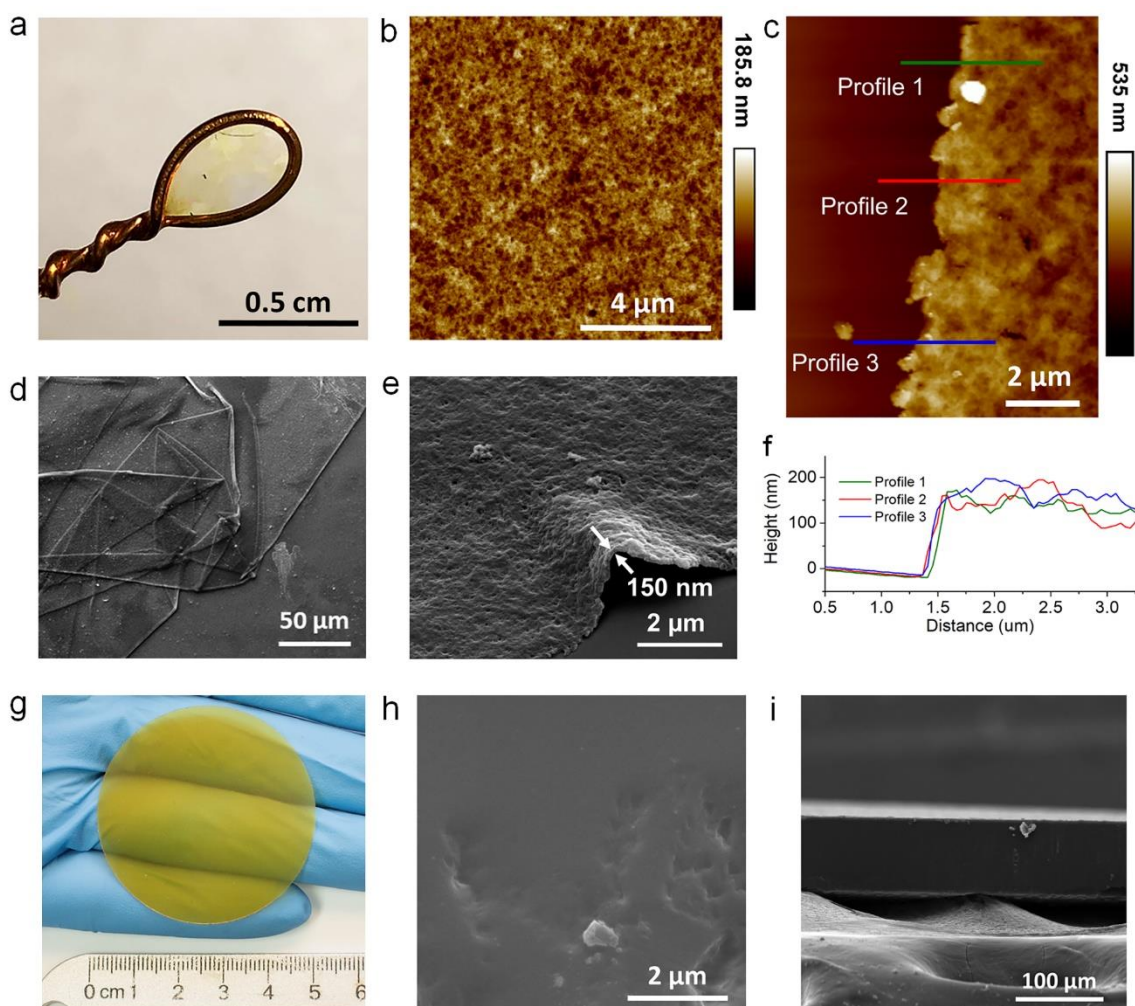


Figure 34. a) Photographic image of a free-standing thin *tri*-PPN membrane with ~200 nm thickness on a copper loop; b,c,f) AFM images showing the surface morphology and thickness of the thin *tri*-PPN membrane; d,e) SEM images showing the flexible nature and the cross section of the thin *tri*-PPN membrane. g) photographic image of a thick *p*-PPN membrane for OSN with thickness of ~100 μm; h,i) SEM images of the surface and cross-section view of the thick *p*-PPN membrane.

with adhesive tape and separated from the tape by soaking in THF. The resulting free-standing membrane floats on the surface of the THF and can be picked up by a copper

wired loop (**Figure 34a**). The freestanding PPN membrane was transferred onto a silicon wafer for atomic force microscopy (AFM) and scanning electron microscopy (SEM) characterization. The surface of these membranes have RMS roughnesses ranging from 15.9 nm to 19.1 nm (**Figure 34b, Figure 37** and **Table 3**), which is similar to other PPN membranes prepared by surface-initiated method⁷ but smaller than COF

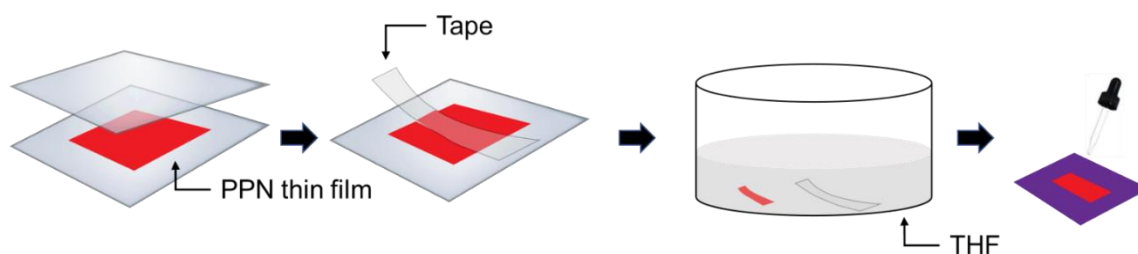


Figure 35. Transfer a PPN thin film from glass substrate onto a silica wafer.

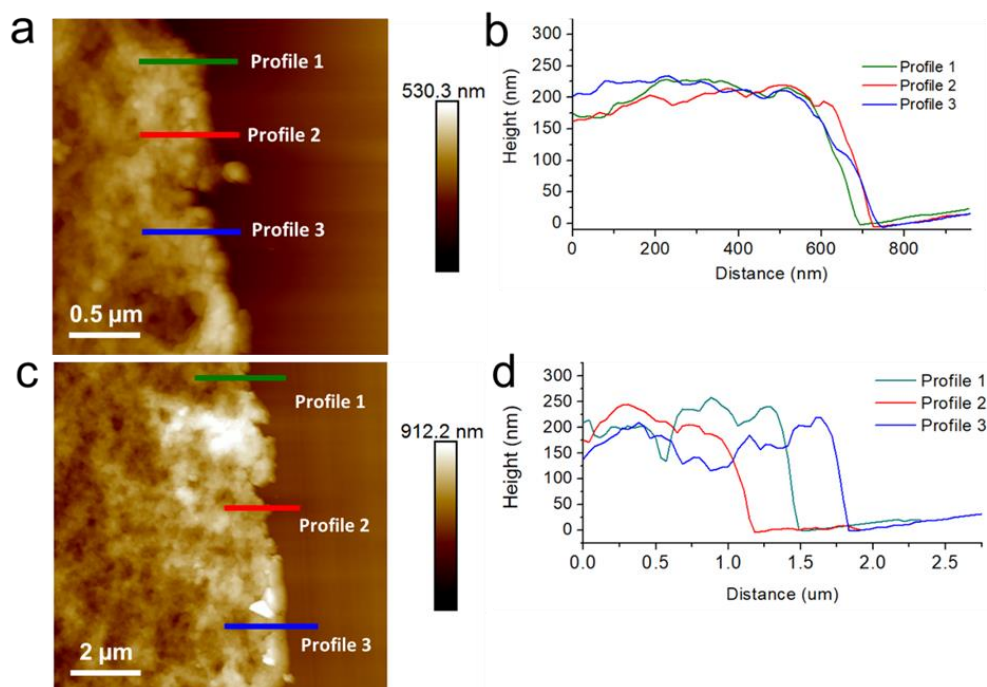


Figure 36. Thickness of a, b) *p*-PPN and c, d) *m*-PPN thin membranes measured by AFM.

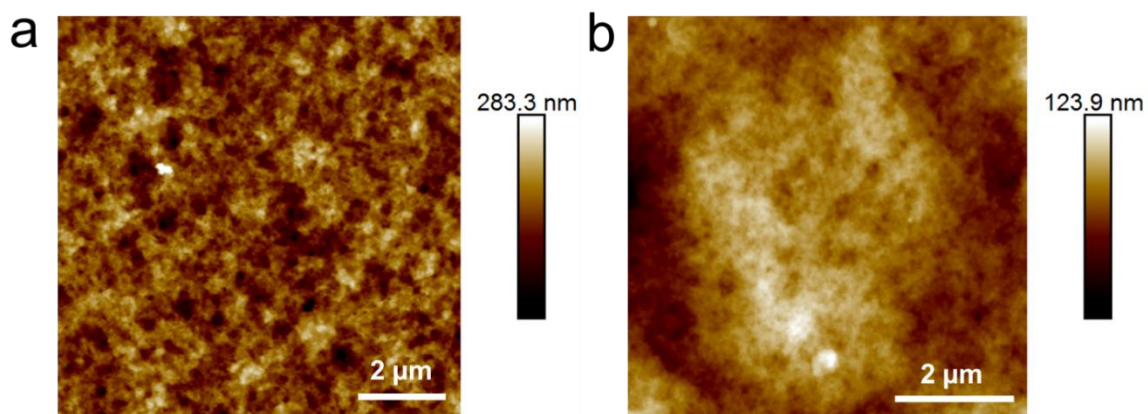


Figure 37. Top-view AFM of a) *p*-PPN and b) *m*-PPN membranes

Table 3. Roughness of *p*-PPN, *m*-PPN, *tri*-PPN membranes measured by AFM

	Rq	Ra
<i>p</i> -PPN	19 nm	15.1 nm
<i>m</i> -PPN	15.9 nm	12.8 nm
<i>tri</i> -PPN	19.1 nm	16.55 nm

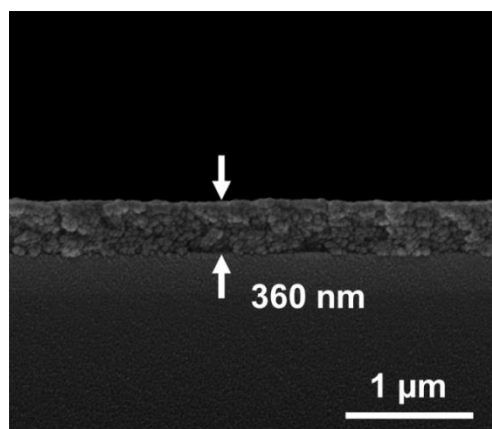


Figure 38. Cross section SEM image of *tri*-PPN membrane fabricated from 30 mg/mL of 1,3,5-triacetylbenzene solution.

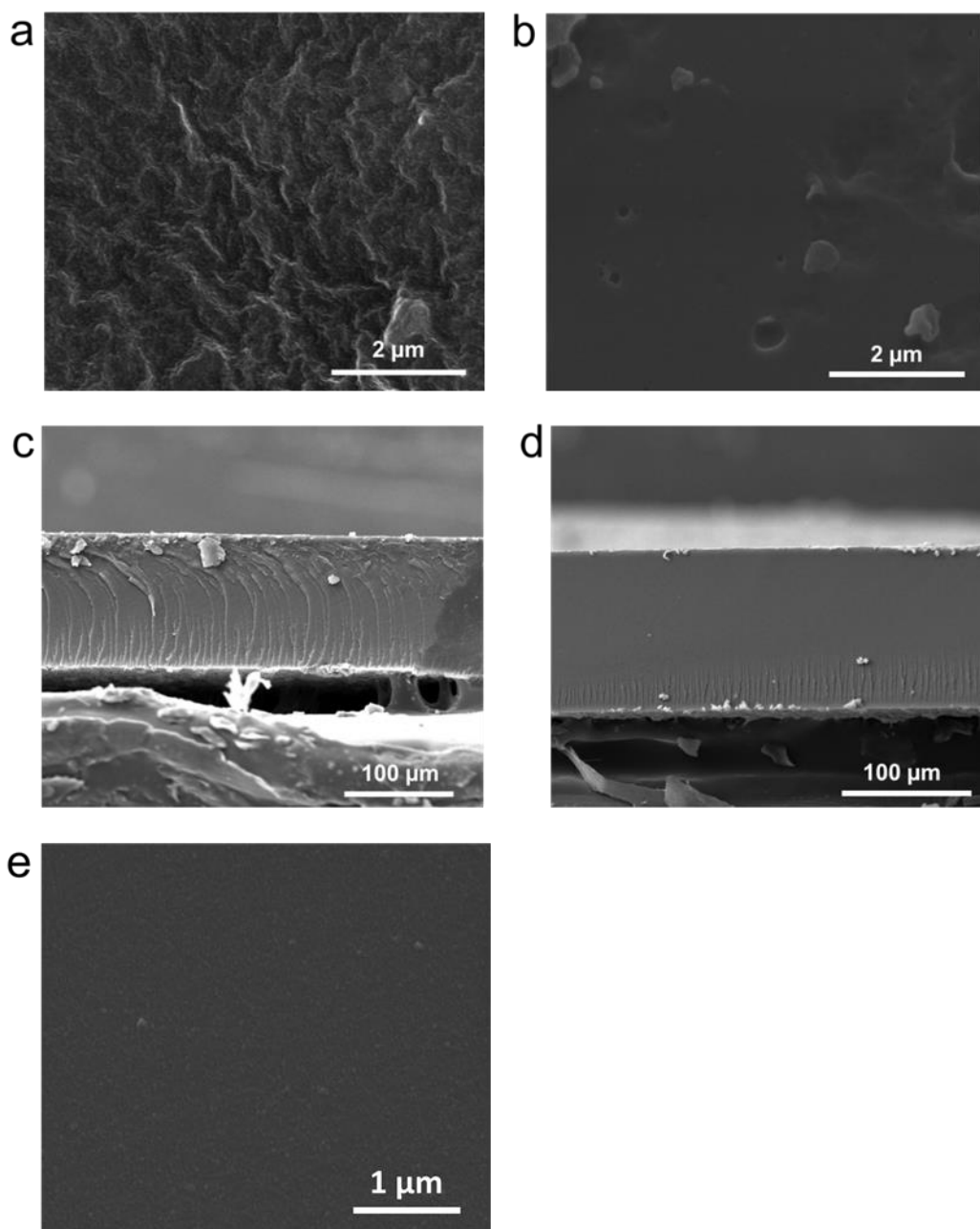


Figure 39. Top and cross-section views of a, c) *m*-PPN and b, d) *tri*-PPN membranes for OSN tests. Cross-section view of e) *p*-PPN membrane with high magnification.

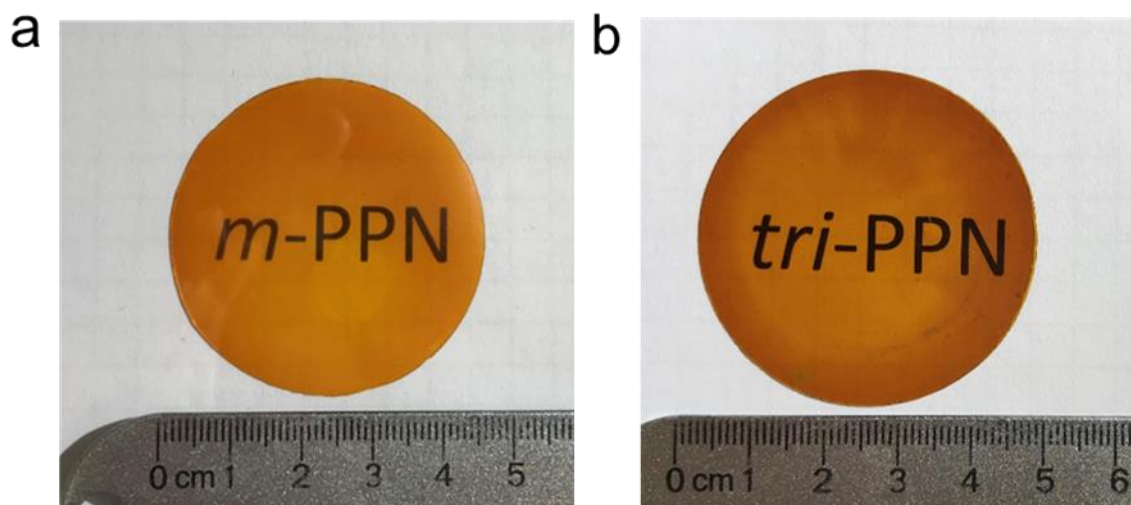


Figure 40. Photographic images of the freestanding a) *m*-PPN and b) *tri*-PPN membranes (4.7 cm in diameter) on top of worded white paper.

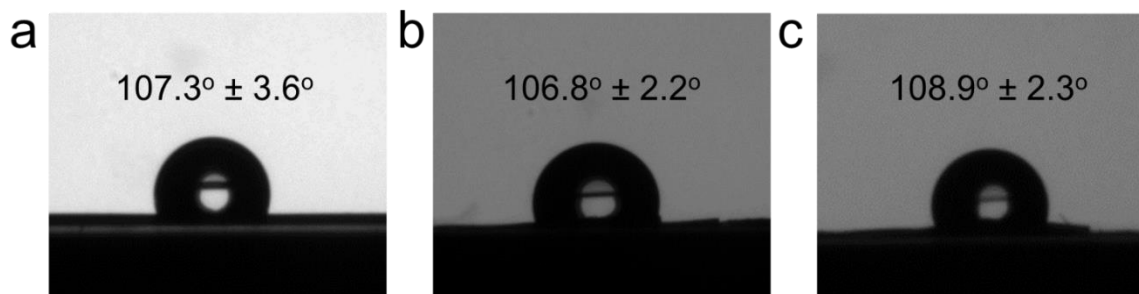


Figure 41. Contact angle of a) *p*-PPN, b) *m*-PPN, and c) *tri*-PPN membranes.

membranes obtained from drop-casting method.³ AFM height profiles (**Figure 34c** and **Figure 36**) show that the thicknesses of *p*-PPN, *m*-PPN, and *tri*-PPN prepared by this method are around 150-200 nm. These thin membranes appeared to be highly flexible and able to crumple and fold on the wafer as visualized by SEM (**Figure 34d**). The thickness of the membrane can be controlled simply by tuning the concentration of the monomer solution. For example, when using a 30 mg/mL 1,3,5-triacetylbenzene solution for the process, it afforded a *tri*-PPN membrane with 360 nm thickness (**Figure 38**). Although these thin membranes were too fragile and small to be tested in a centimetre-sized OSN device, the successful synthesis mentioned above demonstrated the promising potential of the *in situ* cross-linking method in fabricating conjugated PPN membranes for various application including OSN.

In order to fabricate PPN membranes with adequate mechanical strength and size that can be feasibly handled for OSN in a 4.7-cm-diameter cell, higher concentration monomer solutions (90 mg/mL) and 200 μ m-thick glass spacers were used to prepare a series of much thicker and larger membranes (5~6 cm in diameter), which can be easily peeled from the glass slides without the assistance of tape. The surface morphology of these membranes was smooth and unremarkable (**Figure 34 h, i** and **Figure 39**). According to cross-section SEM images, the thicknesses of the *p*-PPN, *m*-PPN, and *tri*-PPN membranes were 121 ± 12 , 118 ± 20 , and 102 ± 19 μ m, respectively. They were washed with methanol and subsequently preserved with polyethylene glycol (PEG) 600 to prevent over-drying. These easy-to-handle, free-standing PPN membranes were cut into

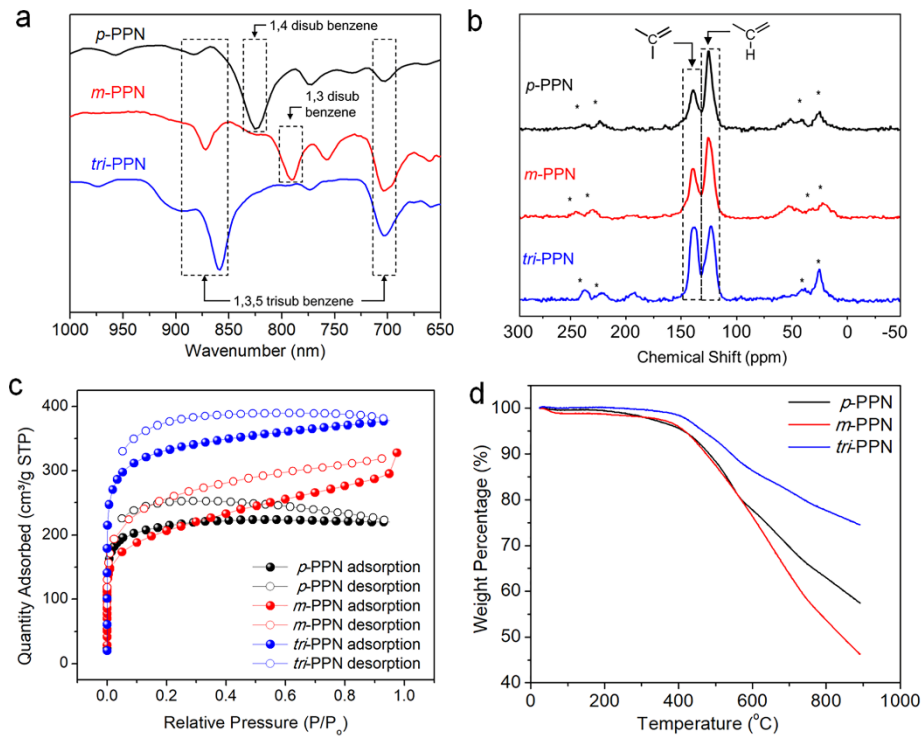


Figure 42. Characterization data of *p*-PPN, *m*-PPN, and *tri*-PPN membranes: a) Aromatic fingerprint region of FTIR spectra; b) SSNMR spectra; c) N₂ adsorption isotherms; d) TGA traces.

round pieces with diameter of 4.7 cm for further OSN measurements (**Figure 34g** and **Figure 40**). Contact angle tests showed the hydrophobic nature of PPN membranes (**Figure 41**).

3.3 Characterization

Chemical characterization of these PPN membranes were performed by using Fourier-transform infrared spectroscopy (FTIR) and solid-state ¹³C CP/MAS nuclear

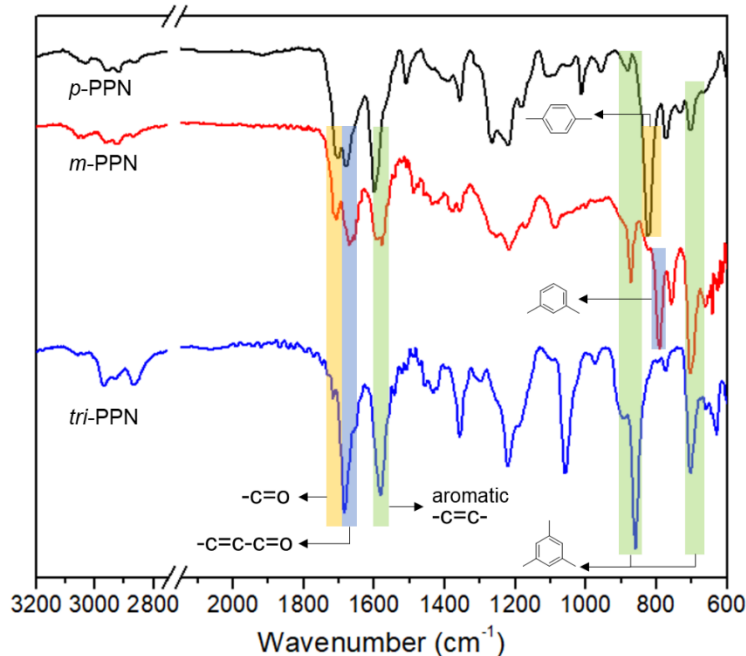


Figure 43. Full FTIR spectra of membranes of a) *p*-PPN, b) *m*-PPN, and c) *tri*-PPN.

magnetic resonance (SSNMR) (**Figure 42 a, b**). FTIR spectra of these membranes were identical to the corresponding powder samples as reported previously.¹⁵² As anticipated, the finger print feature of a 1,4-disubstituted benzene ring at 825 cm^{-1} was observed in the spectrum of *p*-PPN, while that of 1,3-disubstituted benzene ring at 790 cm^{-1} was identified in that of *m*-PPN. In addition, the characteristic features of 1,3,5-trisubstituted benzene rings at 858 – 879 cm^{-1} and 700 cm^{-1} were observed in all of these spectra. FTIR peaks corresponding to aromatic alkenes at 1577 - 1600 cm^{-1} and carbonyl groups at 1670 - 1707 cm^{-1} were also observed (**Figure 43**), indicating the presence of functional group defects resulting from incomplete conversion of the ATC reaction. In the SSNMR spectra, the sp^2 carbons substituted with hydrogen and those without hydrogen can be distinguished into

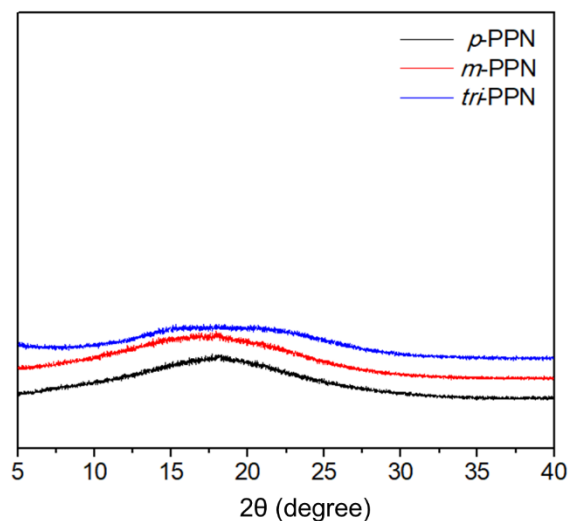


Figure 44. Powder X-ray diffraction of *p*-PPN, *m*-PPN and *tri*-PPN.

two major resonance signals at 124.6 – 126.9 ppm and 140.7 ppm, respectively. Notably, in *p*-PPN and *m*-PPN, the ratio of signal intensities between the hydrogen substituted carbons and the non-hydrogen carbons were similar and significantly higher than that in *tri*-PPN, in accordance to the theoretical compositions of these different types of carbons in the products. The amorphous structure of PPN membranes was confirmed by powder X-ray diffraction tests where no distinct diffraction peak was observed (**Figure 44**).

The porosity of these PPN membranes was characterized by N₂ adsorption tests at 77 K. The N₂ adsorption data showed type I isotherms, revealing microporosity in the PPN membranes (**Figure 42c**), similar to the corresponding powder samples¹⁵². Despite their amorphous nature and defects, these PPN membranes showed narrowly distributed pore sizes with a majority of the pores smaller than 1.5 nm (**Figure 45**). Particularly, *p*-PPN showed a major peak at 1.2 nm in the pore size distribution diagram, in agreement with

Table 4. Porosity of *p*-PPN, *m*-PPN, *tri*-PPN membranes

Membranes	BET surface area	Langmuir surface area	Pore volume
<i>p</i> -PPN	802 m ² /g	928 m ² /g	0.28 cm ³ /g
<i>m</i> -PPN	734 m ² /g	1071 m ² /g	0.33 cm ³ /g
<i>tri</i> -PPN	1235 m ² /g	1440 m ² /g	0.47 cm ³ /g

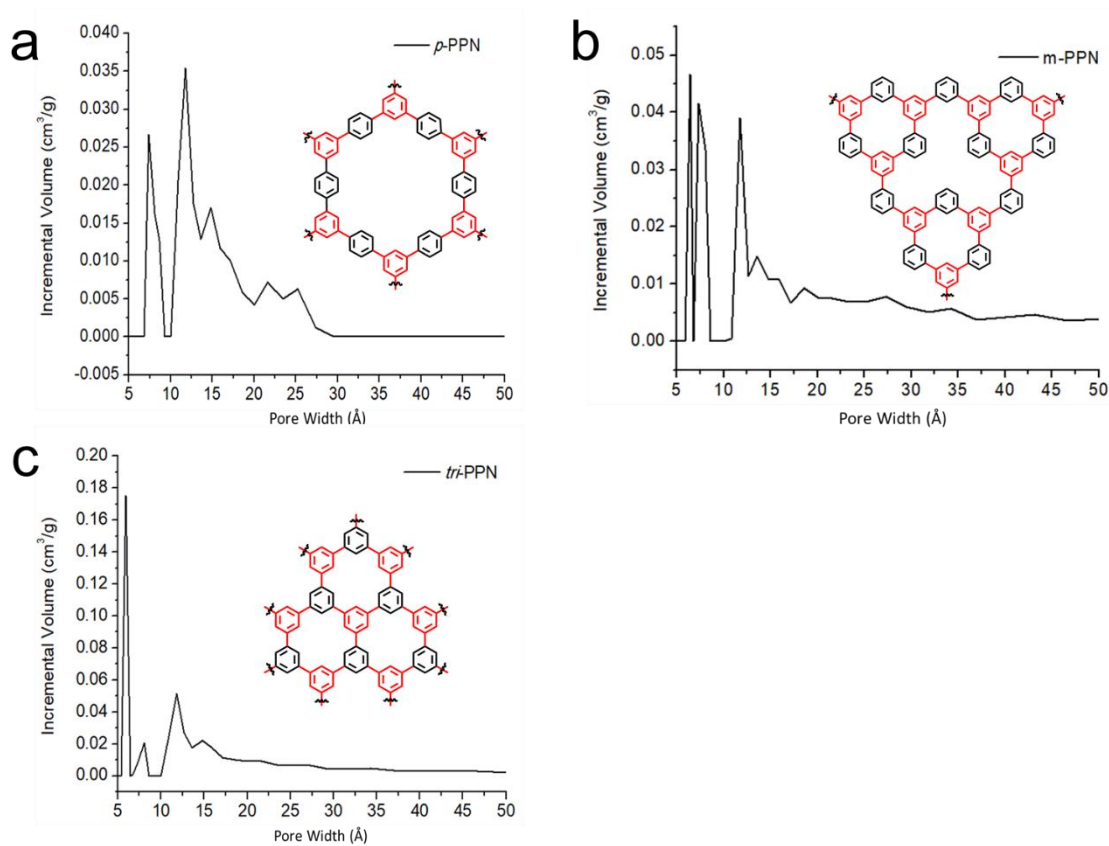


Figure 45. Pore size distribution of membranes of a) *p*-PPN, b) *m*-PPN, and c) *tri*-PPN, calculated based on DFT method.

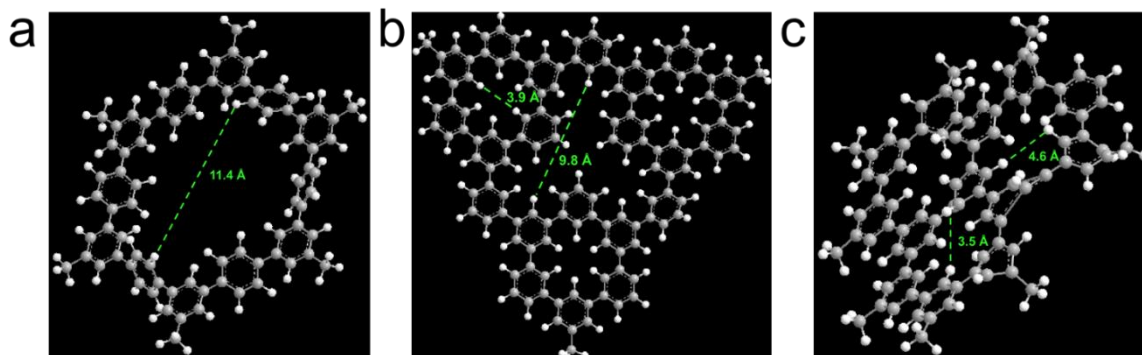


Figure 46. Estimated pore size from ideal structure of a) *p*-PPN b) *m*-PPN, and c) *tri*-PPN by Chem3D.

the estimated pore size from the ideal structure shown in **Figure 45, 46**. The measured pore sizes of *m*-PPN and *tri*-PPN, however, were slightly larger than the estimated values, likely a result of bigger steric hindrance of the backbone around the smaller pores. Nevertheless, *tri*-PPN, composed of only tri-substituted benzene rings, exhibited the smallest average pore size among these samples. The major peak in pore size distribution diagram of *tri*-PPN is located at 0.6 nm. Also as expected, broader pore size distribution of *m*-PPN was observed with the major peak ranging from 0.7 nm to 1.2 nm resulting from the less symmetrical 1,3-disubstituted monomer. The Brunauer-Emmett-Teller (BET) surface areas of *p*-PPN, *m*-PPN, and *tri*-PPN membranes were determined to be 802, 734, and 1235 m²/g, respectively (**Table 4**). The BET surface area of *p*-PPN membrane was also close to that of the bulk powder sample of *p*-PPN¹⁵², indicating the high efficiency of the *in situ* ATC cross-linking reaction in the membrane. Benefiting from the rigid framework, *tri*-PPN demonstrated a high BET surface area compared to CMP membranes with similar pore size.⁷ The thermal stability of PPN membranes was characterized by thermogravimetric analysis (TGA, **Figure 42d**). The 5% weight loss onset temperatures

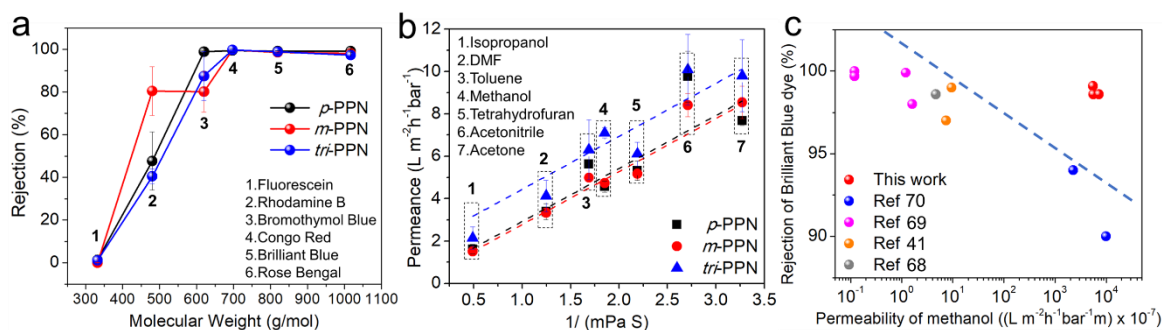


Figure 47. OSN performance of *p*-PPN, *m*-PPN, *tri*-PPN membranes: a) rejection rate as a function of the molecular weight of the dye solute; b) membrane permeance values as a function of the solvent viscosity; c) rejection of brilliant blue verses permeability of methanol for PPN membranes, comparing with reported microporous polymer membranes, including COFs, polyarylate, CMPs, and cyclodextrin. The dash line indicates an upper bond.

for *p*-PPN, *m*-PPN, and *tri*-PPN were all above 410 °C. Especially, *tri*-PPN was stable with less than 10% weight loss until 543 °C. The outstanding thermal stability of these PPN membranes can be attributed to the aromatic nature of the backbone. It enables potential application of these membranes in some high temperature conditions that were conventionally only possible with ceramic membranes.¹⁵⁴

3.4 Organic Solvent Nanofiltration Performance

With high porosity and narrowly distributed pore size, *p*-PPN and *tri*-PPN membranes were expected to possess high permeability and good selectivity for efficient OSN. To test their OSN performances, pinhole-free PPN membranes with thickness around 100 μm and diameter of 4.7 cm were tested by using a dead-end solvent resistant



Figure 48. Photographic image of a *p*-PPN membrane performing OSN in a solvent resistant

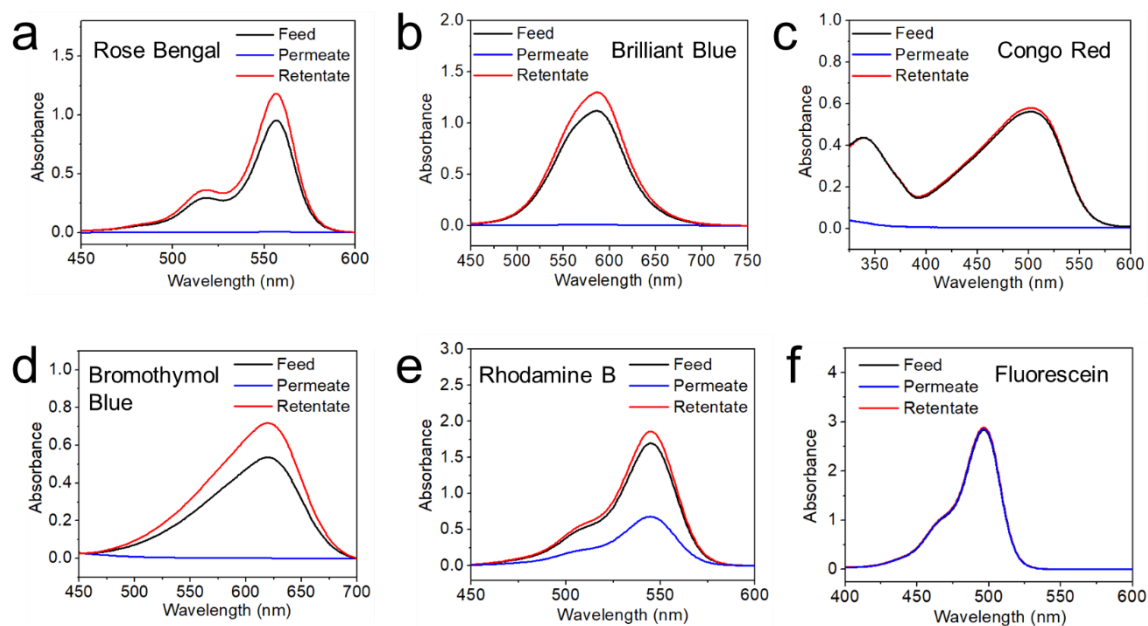
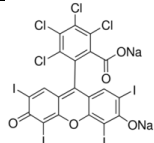
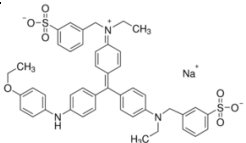
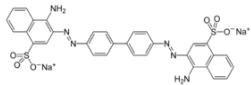
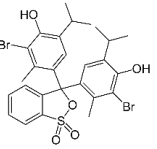
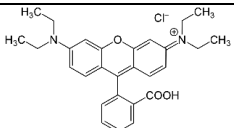
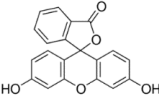


Figure 49. UV-vis spectra of feed permeate and retentate of dye molecules before and after OSN by *p*-PPN membranes. a) rose bengal, b) brilliant blue, c) congo red, d) bromothymol blue, e) rhodamine B, f) fluorescein

Table 5. Summary of dye molecules size and average rejection of PPN membranes

Dye Molecules	Structure	Molecular weight (g/mol)	Dimension (Å)	Rejection (<i>p</i> -PPN)	Rejection (<i>m</i> -PPN)	Rejection (<i>tri</i> -PPN)
Rose Bengal		1017	14.9 × 14.9	99.2 %	98.1 %	97.3 %
Brilliant Blue		820	23.0 × 28.0	99.1 %	98.6 %	98.9 %
Congo Red		697	12.9 × 28.3	99.5 %	99.7 %	99.7 %
Bromothymol Blue		624	12.0 × 14.8	98.9 %	80.2 %	87.5 %
Rhodamine B		479	13.9 × 16.5	47.7 %	80.5 %	40.5 %
Fluorescein		332	11.8 × 12.4	1.3 %	3.9 %	1.2 %

stirred cell (**Figure 48**). Methanol solutions of various organic dyes, with molecular weight ranging from 332 g/mol to 1017 g/mol to meet the nanofiltration requirements (200-1000 g/mol), were used as feed solutions to be filtered through the membranes under a transmembrane pressure (TMP) of 1 bar. The dyes used are fluorescein, rhodamine B, bromothymol blue, congo red, brilliant blue, and rose bengal (see **Table 5** for chemical structures and molecular sizes). The rejection rate of PPN membranes to each dye was defined as one minus the percentage ratio of the concentration between the permeate and the feed solutions compared with the original feed concentration, all measured by UV-vis absorption spectroscopy following the Beer-Lambert law (**Figure 49**). The rejection rates were plotted against the molecular weights of the dyes (**Figure 47a**). As expected, *p*-PPN, *m*-PPN, and *tri*-PPN membranes showed almost complete rejection (98 – 99.7%) to larger dyes such as congo red (687 g/mol), brilliant blue (820 g/mol) and rose bengal (1017 g/mol). Neutral compound bromothymol blue (624 g/mol) was also completely rejected by *p*-PPN membranes. Considering the charge-neutral and non-polar nature of the backbone as well as the negligible electrostatic repulsion/interaction between the solute molecules and the membrane backbone in organic solvent,⁴⁴ the rejection mechanism was attributed to size exclusion instead of charge repulsion or polar interaction. The molecular weight cut-off (MWCO) of *p*-PPN, *m*-PPN, and *tri*-PPN membranes were approximately 600, 660, and 630 g/mol, respectively, which are similar to those of CMP membranes with similar pore size.⁷ The rejection rate decreased drastically as the molecular weight of the dyes decreased. The molecular weight retention onset (MWRO), where the rejection is 10%, of all the PPN membranes were around 350 g/mol. Selectivity measured based on

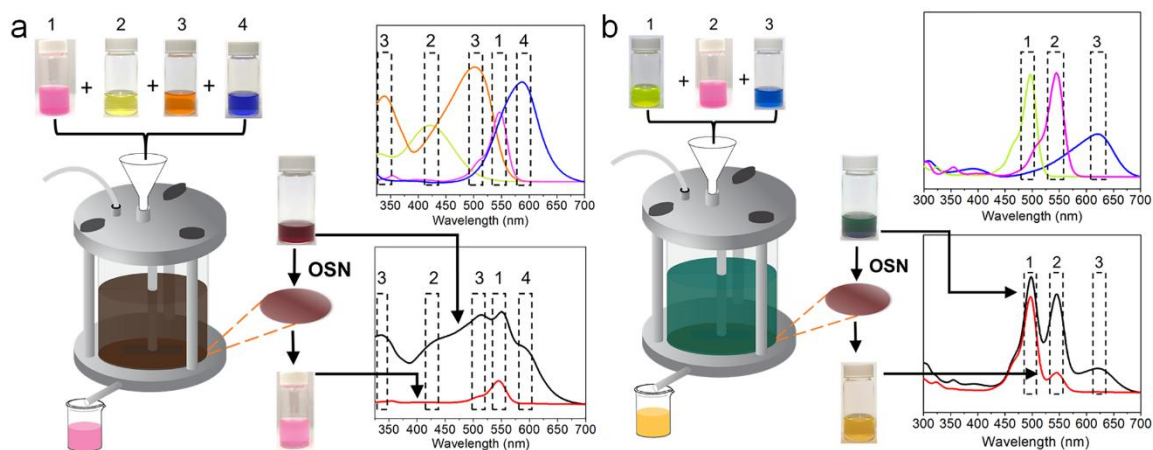


Figure 50. Scheme of dye separation performance of *p*-PPN membrane and UV-vis absorption spectra of the feed solution and the permeate: a) separating (1) rhodamine B from (2) bromothymol blue, (3) congo red and (4) brilliant blue; b) separating (1) fluorescein and (2) rhodamine B from (3) bromothymol blue.

MWRO and MWCO of *p*-PPN and *tri*-PPN membranes are comparable to those of highly crystalline COF membranes⁴⁴. Such a good selectivity was attributed to the narrowly distributed pore sizes of the PPN membranes. It is also noteworthy that *m*-PPN membrane showed an anticipated lower selectivity, a result of its broader pore size distribution. It is also noteworthy that the adsorption of the dye molecules to the membrane was possible¹⁵⁵⁻¹⁵⁷ but was not significant at the concentration used in the OSN experiments, indicated by the comparable concentration of the permeated small dyes and increased concentration of the rejected retentate (**Figure 49**). The sharp OSN selectivity allowed for efficient separation of organic compounds that are only moderately different from each other in size, which has been a challenging task for membrane separation. For example, in a test of separating a complex mixture of four dyes, rhodamine B (479 g/mol) can be isolated efficiently from bromothymol blue (624 g/mol), congo red (697 g/mol) and brilliant blue

(820 g/mol) through a *p*-PPN membrane (**Figure 50a**). After a standard OSN operation of the feed solution containing the aforementioned four dyes, the permeate solution contained only rhodamine B while the three larger dyes were rejected. The UV-vis spectrum of the permeate showed that the absorption peak of bromothymol blue at 620 nm was completely removed after OSN. Similarly, in another OSN test of a three-dye mixture of fluorescein, rhodamine B and bromothymol blue, only bromothymol blue (624 g/mol) was rejected by *p*-PPN membrane while the smaller dyes fluorescein (332 g/mol) and rhodamine B (479 g/mol) permeated (**Figure 50b**). By using this method, dyes smaller than the MWCO could be separated from dyes larger than the MWCO in mixed solutions in a highly efficient manner without tedious chromatography, demonstrating the advantages of using microporous membrane to perform size-selective OSN separation over the conventional dense membrane of which separation mainly depends on different permeability and diffusivity.⁶⁷

The cross-linked network and the aromatic hydrocarbon backbone make these PPN membranes suitable for OSN of a wide range of organic solvents, including nonpolar, polar aprotic, and polar protic solvents. Permeance of a wide range of organic solvents through these membranes was found to be linearly related with the reciprocal of solvent viscosity rather than molecular diameter, solubility parameter or dielectric constant (**Figure 47b**, **Figure 51**), suggesting that the diffusion of solvent through these PPN membranes followed a pore flow model.^{37,158} It also indicated that solvent permeance was not significantly impacted by possible chemical interaction of the solvent molecules

Table 6. Summary of OSN performance of aromatic PPN membranes compared with other state-of-art polymer membranes

Membrane	Name	Rejection to Brilliant Blue (%)	Permeance of methanol (L m ⁻² h ⁻¹ bar ⁻¹)	Thickness	Permeability (L m ⁻² h ⁻¹ bar ⁻¹ m x 10 ⁻⁷)	Ref
Aromatic PPN	<i>p</i> -PPN	99.1	4.57	121 μm	5530	This work
	<i>m</i> -PPN	98.6	4.47	118 μm	5593	
	<i>tri</i> -PPN	98.6	7.10	102 μm	7242	
CMP	<i>p</i> -CMP	99	22.5	42 nm	9.45	1
	<i>m</i> -CMP	97	16.4	45 nm	7.38	
	<i>o</i> -CMP	85	21	44 nm	9.24	
Polyarylate	PAR-BHF	98	8.0	20 nm	1.6	2
	PAR-TTSBI	99.9	6.0	20 nm	1.2	
	PAR-DHAQ	100	0.6	20 nm	0.12	
	PAR-RES	99.7	0.6	20 nm	0.12	
CD	β-CD	98.6	4.9	95 nm	4.66	3
COF	TpBpy	94	108	2.1 μm	2270	4
	TpAzo	90	188	5.3 μm	9964	

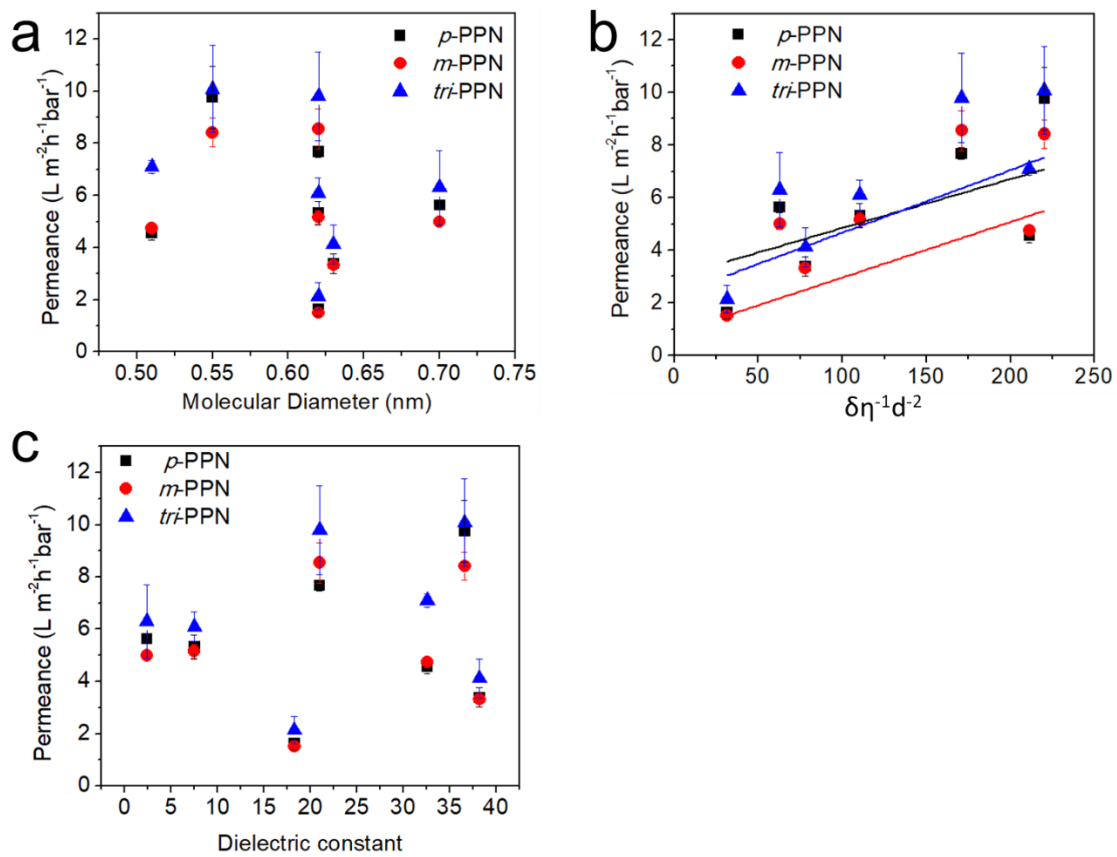


Figure 51. Plot of permeance of solvent against a) molecular diameter of solvents, b) combined solvent properties (Hansen solubility parameter \times $1/\text{viscosity} \times 1/(\text{molecular diameter})^2$), and c) dielectric constant.

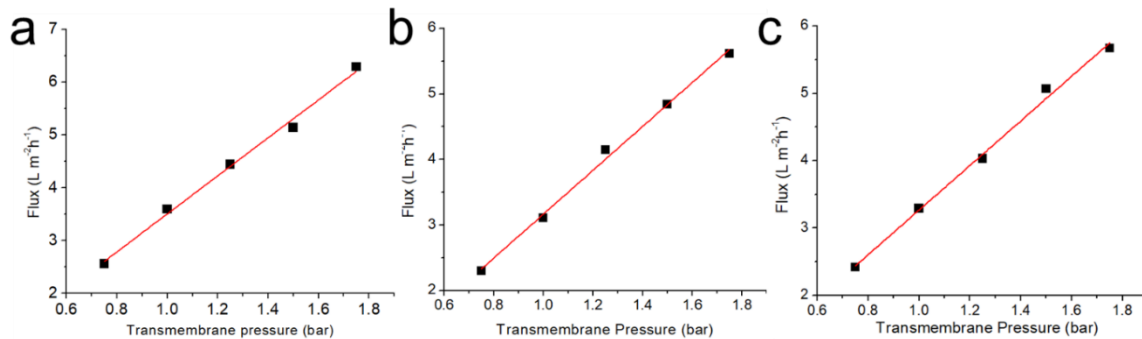


Figure 52. Flux of a) methanol, b) toluene, and c) THF vs transmembrane pressure relationship of *p*-PPN membrane.

with the membrane backbone or with the defect sites.⁴⁴ The pressure normalized permeance of methanol, toluene, and THF all remained constant under different TMPs (Figure 52). The permeance of *tri*-PPN membrane was consistently higher than that of *p*-PPN and *m*-PPN membranes, benefitting from its higher porosity. Notably, the permeance of toluene for these PPN membranes ($5 - 6.3 \text{ L m}^{-2} \text{ h}^{-1} \text{ bar}^{-1}$) was higher than that of CMP membranes ($4.2 \text{ L m}^{-2} \text{ h}^{-1} \text{ bar}^{-1}$)⁷ with similar MWCO even though these measured PPN membranes were much larger in size and three orders of magnitude thicker. The intrinsic permeability values of methanol through *p*-PPN, *m*-PPN, and *tri*-PPN were 5.53×10^{-4} , 5.593×10^{-4} , and $7.242 \times 10^{-4} \text{ L m}^{-2} \text{ h}^{-1} \text{ bar}^{-1} \text{ m}$, respectively, significantly higher than many benchmark polymeric OSN membranes.¹³⁶ For microporous polymer membranes, the permeability typically remains constant from thicknesses between 100 nm and 30 μm with a TMP as high as 15 bar.¹⁴⁰ The rejection performance against brilliant blue (a widely studied model dye for OSN) and permeability of these PPN membranes in methanol are plotted in comparison with those of representative cohorts of polymeric OSN membranes

(**Figure 47c**, **Table 6**). These literature examples including membrane of COFs,⁷¹ polyarylate,⁷⁰ conjugated microporous polymers,⁷ and cyclodextrin⁶⁹. The plot showed a trade-off relationship between permeability and selectivity, so that an upper bound was observed.^{65,66} Compared with these literature data, the PPN membranes in this work are situated well above the upper bound with excellent solvent permeability while remaining a high solute rejection rate. This remarkable combination of properties was attributed to the highly porous and non-interactive nature of the aromatic backbone of these PPN membranes.

3.5 Stability Test

The rigid cross-linked aromatic framework also imparted the PPN membranes with extraordinary chemical stability and robust porous structure, which is critical for OSN performance in extreme conditions. The stability of aromatic PPN membranes were studied extensively. First, *p*-PPN membranes were soaked in a variety of solutions with harsh conditions for 5 days: 18 M H₂SO₄, 0.1 M chromic acid, 14 M NaOH in water/methanol, and 2 M NaBH₄ in methanol. FTIR spectra of these treated samples all showed similar peak positions and retained features for 1,4- and 1,3,5-substituted benzene rings, indicating that the PPN backbone was mostly intact during these treatments. Minor changes on certain IR peaks were observed on the samples treated with NaBH₄, H₂SO₄ and chromic acid, likely a result of reduction or oxidation of the residual defect sites (*e.g.*, the ketone and α,β -unsaturated ketone groups). (**Figure 53**). The surface morphology of those PPN membranes were also maintained well after these treatments according to SEM

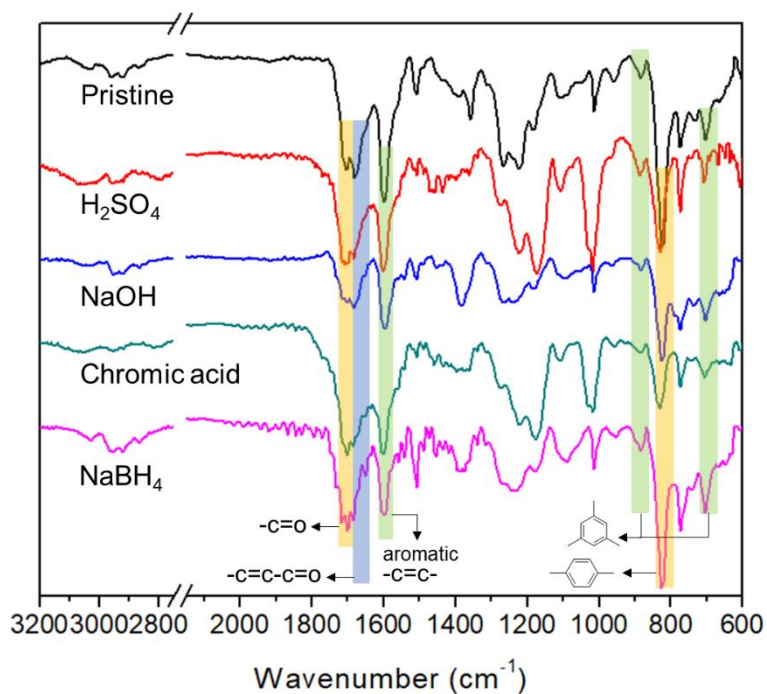


Figure 53. FTIR of pristine *p*-PPN membrane and *p*-PPN membranes treated by extreme conditions for 5 days. The conditions were 18 M H_2SO_4 , 14 M NaOH in water/methanol, 0.1 M chromic acid, and 2 M NaBH_4 in methanol.

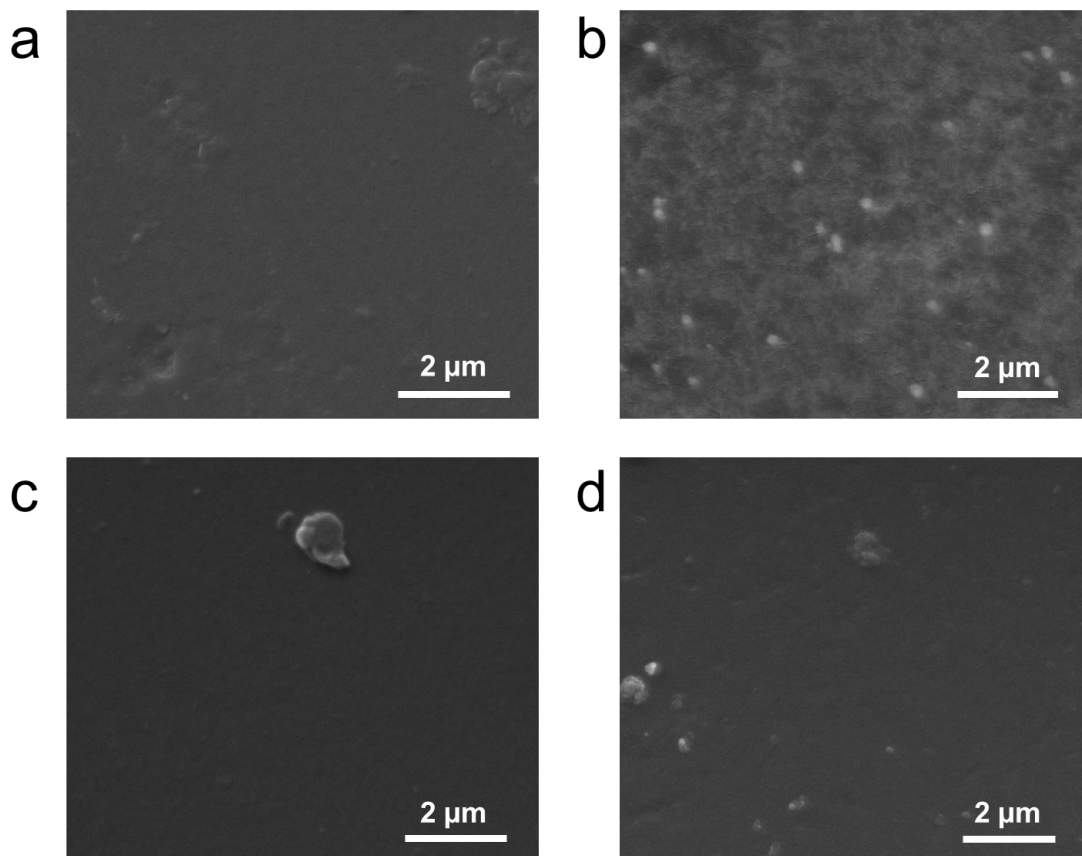


Figure 54. Surface morphology of and *p*-PPN membranes treated by extreme conditions for 5 days. The conditions are 18 M H₂SO₄, 14 M NaOH in water/methanol, 0.1 M chromic acid, and 2M NaBH₄ in methanol.

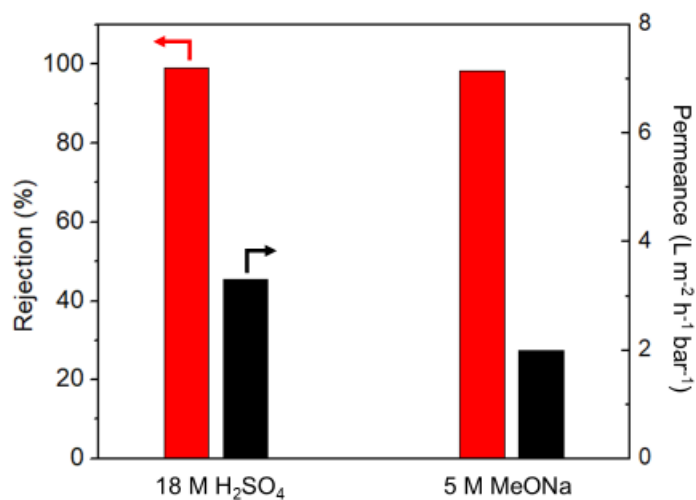


Figure 55. The rejection and permeance of congo red in methanol after *p*-PPN membrane soaking in 18 M H₂SO₄ for 2 days and the rejection and permeance of rose bengal in methanol after *p*-PPN membrane soaking in 5M MeONa for 2 days.

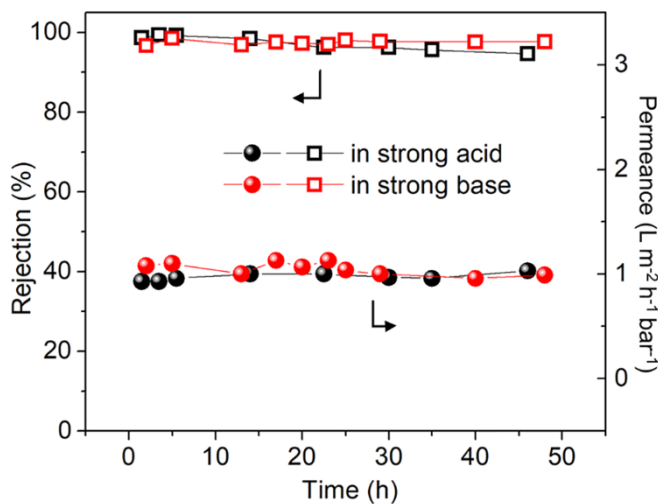


Figure 56. Long-term OSN test of *p*-PPN membrane filtrating isopropanol solutions of brilliant blue in the presence of PTSA and rose bengal in the presence of NaOH.

Table 7. Summary of OSN performance in harsh condition of aromatic PPN membranes compared with commercial membranes

OSN membrane	polymer	MWCO (g/mol)	Solvent / permeance (L m ⁻² h ⁻¹ bar ⁻¹)	Continuous operation	Clean tolerance
PPN membrane	PPN	600	MeOH / 4.6	10 mM NaOH / PTSA in IPA	18 M H ₂ SO ₄ / 5M NaOMe
Puramem® S600	polyimide	600	MeOH / 0.23 ⁷	pH =7	-
Duramem® 500	polyimide	500	MeOH / 1.46 ⁷	pH =7	-
Duramem® 500	polyimide	900	MeOH / 1.56 ⁷	pH =7	-
Solsep® NF 030705	PDMS	500	ACN / 0.2 ⁸	pH = 2-10.5	-
Solsep® NF 090801	PDMS	350	ACN / 0.9 ⁸	-	-
Filmtec™ NF270	polyamide	200-400	ACN / 11 ⁸	pH = 2-11 *	pH = 1-12 *
Starmem® 240	polyimide	400	Ethanol / <1 ⁹	-	-

* The performance of Filmtec NF270 was tested in aqueous solution instead of in organic solution.

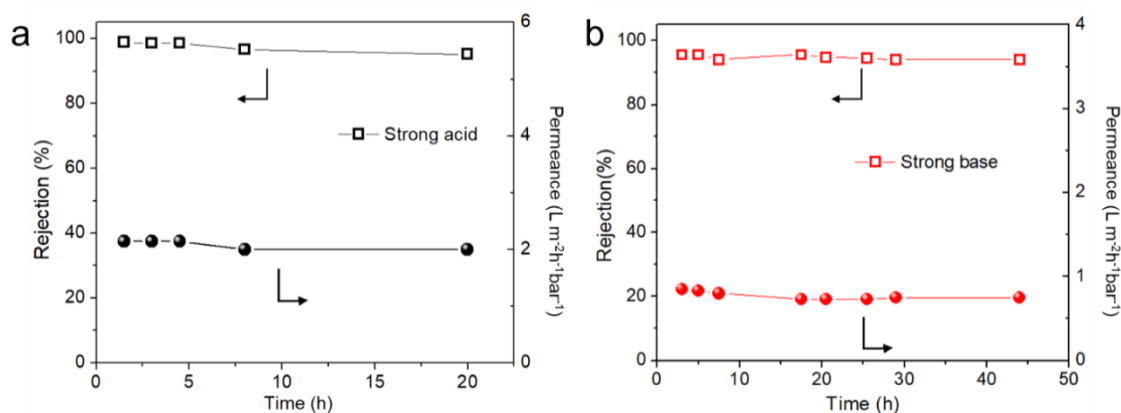


Figure 57. Long-term OSN test of *p*-PPN membrane filtrating ethanol solutions of a) brilliant blue in the presence of PTSA and b) congo red in the presence of NaOH.

(**Figure 54**). OSN of *p*-PPN membranes after soaking in 18 M H₂SO₄ and in 5 M NaOMe in methanol for 2 days were investigated. The rejection of congo red and rose bengal of these treated *p*-PPN membranes remained at 99.0% and 98.2%, respectively (**Figure 55**). Long-term OSN performance of *p*-PPN membrane under harsh conditions was examined through OSN of strong acid and strong base solutions for 48 h. Specifically, brilliant blue in isopropanol with 10 mM *p*-toluenesulfonic acid (PTSA) was used to test acidic condition, while rose bengal in isopropanol with 10 mM NaOH was used for basic conditions. In both cases, the rejection. of the dye remained over 95% and the permeance of isopropanol was steady over 48 h (**Figure 56, 57**). Such a remarkable stability outperforms most commercial organic OSN membranes¹⁵⁹⁻¹⁶¹ (**Table 7**) and is comparable to some of the most stable OSN membranes reported to date^{3,147,162,163}. This work also represents an unprecedented example of a polymer membrane whose OSN performance could be remained extensively while a strongly acidic or basic organic solution is used as the feed. The chemical stability and robust porous structure of *p*-PPN membranes can be

attributed to the rigid and inert aromatic nature of its backbone. The stable OSN performance of *p*-PPN in strong acid/base conditions not only makes it suitable for practical applications in these harsh environments, but also allows for treatment of the membranes with strong acid or base to tackle potential fouling problems.

3.6 Conclusion

In summary, aromatic PPN membranes were synthesized through a highly efficient ATC reaction using MSA as both the catalyst and the solvent, via simple drop-casting followed by *in situ* polymerization. These membranes can be fabricated from different monomers with controllable thicknesses. Despite their amorphous nature, the non-polar micropores are narrowly distributed in terms of sizes, enabling molecular-sieving effect in OSN with high intrinsic permeability and good selectivity. Benefiting from the aromatic framework, these PPN membranes exhibited outstanding thermal and chemical stability and consequently possess durable long-term OSN performance in either strong acid or strong base conditions. The combined merits of these membranes not only afford an outstanding potential OSN performance, but also provide opportunities to tackle the practical challenges in OSN in terms of extreme chemical conditions and membrane fouling.

3.7 Experimental Section

3.7.1 General Information

1,4-diacetylbenzene, 1,3-diacetyl-benzene and 1,3,5-triacetylbenzene were purchased from TCI America. Methanesulfonic acid (MSA) was purchased from Oakwood Chemical. All dye molecules were purchased from TCI or Sigma-Aldrich. All purchased starting materials were used without further purification. Field-emission scanning electron microscopic (SEM) images were collected using the FEI Quanta 600 FE-SEM at 20 kV. Film samples were taped on double side carbon tape and were coated with iridium prior tests. Atomic Force Microscopy (AFM) images were collected with a Bruker Dimension S4 Icon AFM in tapping mode and processed by NanoScope Analysis. In order to measure the thickness of film, a scratch was applied on the surface of film to expose the silicon wafer. N₂ adsorption data were collected from activated samples using the Micrometrics ASAP 2020 at 77 K from 0-1 bar. The porosity data including Brunauer–Emmett–Teller (BET) surface area were calculated by density functional theory (DFT) method. The ideal pore size of PPN membranes were calculated based on ideal scheme in Chem3D. Thermogravimetric analysis (TGA) was carried on with a TA Q500 thermogravimetric analyzer from 30-900 °C at a heating rate of 20 °C min⁻¹ under N₂ atmosphere. Fourier transform infrared spectroscopy (FTIR) spectra were recorded by ZnSe attenuated total reflection with a Shimadzu IRAffinity-1S spectrometer. Powder X-ray diffraction (PXRD) was obtained with a Bruker D8-Focus Bragg-Brentano X-ray Powder Diffractometer equipped with a Cu sealed tube ($\lambda = 1.54178 \text{ \AA}$) at 40 kV and 40 mA. Solid-state C¹³ nuclear magnetic resonance (NMR) data were obtained using Bruker

Advance-400 Solids NMR spectrometer. Membrane samples were ground into powder and purified by soxhlet extraction using ethanol before TGA, FTIR and solid-state NMR tests. UV-Vis absorption spectra were recorded with a Shimadzu UV-2600 UV-Vis spectrophotometer. Contact angles were measured using a CAM 200 Optical Goniometer. A drop size of 10 μ L was used to apply the test liquids. Dimension of dye molecules indicated by Van der Waals diameters were calculated by MarvinSketch.

3.7.2 Fabrication of PPN Thin Film.

The monomer (1,4-diacetylbenzene, 1,3-diacetylbenzene or 1,3,5-triacetylbenzene) was dissolved in MSA at 50 °C to form a 15 mg/mL solution. The solution was drop casted onto a micro cover glass and sandwiched by another micro cover glass, followed by heating at 110 °C for 24 h. After the reaction was completed, the micro cover glasses were separated and PPN film was adhered to one of glass pieces. A pressure-sensitive tape was used to tape off the film from the glass surface (**Figure 35**). The tape was then soaked in THF where the polyacrylate adhesive was dissolved and PPN thin film was released into THF, and subsequently transferred onto a silicon wafer by using a pipette, and rinsed with THF for further tests.

3.7.3 Fabrication of PPN Membranes for OSN.

The monomer (90 mg) was dissolved in MSA (1 mL) at 50 °C to form the reaction solution. The solution was drop casted onto a 6 \times 6 inches glass substrate and sandwiched by another piece of glass with the same size. These glass substrates were pre-treated by

spray-coating a thin layer of PTFE to prevent undesired adhesion of the membrane onto the glass. Two pieces of 200 μm -thick micro cover glass slides were placed in between (**Figure 33b**). The sandwiched system was heated at 110 $^{\circ}\text{C}$ for 24 h. After the reaction, the freestanding PPN membrane was detached from the glass substrate and soaked in methanol for 45 min. It was then taken out and soaked in another batch of clean methanol. After repeating for twice, the membrane was either used directly for subsequent experiments, or preserved by soaking in PEG 600/methanol solution (weight ratio = 1:1) overnight and dry in the air for long-term storage.

3.7.4 OSN Tests of PPN Membranes.

A piece of PPN membrane was washed thoroughly by methanol and cut by a round cutter with diameter of 4.7 cm. The membrane was transferred into a dead-end solvent-resistant stirred cell (Millipore, effective diameter 4.7 cm) with a Nylon filtration membrane (Whatman, 0.45 μm pore size) underneath as a cushion (**Figure 48**). Kalrez[®] solvent-resistant O-ring (outside diameter 4.7 cm) was placed on the PPN membrane to seal the cell. All experiments were repeated for at least three times. In a typical dye rejection test, dye solution (30 mL, 10 ppm) was charged into the cell as the feed solution. A transmembrane pressure of 1 bar was applied by using compressed nitrogen gas. The feed solution was stirred at 400 rpm to minimize concentration polarization effect close to the membrane. The first 3 mL of permeate was discarded and the following permeate was collected for measurements. After the test, the solution remained in the cell was collected as the retentate. The concentration of feed, permeate, and retentate was measured by UV-

vis spectrophotometer. The rejection R was calculated using Equation (1), where C_f and C_p is the concentration of feed and permeate, respectively.

$$R = \left[1 - \left(\frac{C_p}{C_f} \right) \right] \times 100\% \quad (1)$$

In a pure solvent permeance test, 30 mL pure organic solvent (acetonitrile, acetone, methanol, tetrahydrofuran, toluene, dimethylformamide, or isopropanol) was used as the feed. The permeation test was conducted under transmembrane pressure of 1 bar with stirring rate of 400 rpm. The first 3 mL was discarded and the permeation time and solvent volume of the following permeate was recorded. The permeance p of PPN membrane was calculated using Equation (2), where V is solvent volume, A is effective area of membrane, t is time, Δp is TMP.

$$p = \frac{V}{A \cdot t \cdot \Delta p} \quad [unit: L m^{-2} h^{-1} bar^{-1}] \quad (2)$$

The permeability P , which reveals the intrinsic property of materials, of PPN membrane was calculated using Equation (3), where p is permeance and l is thickness of membrane.

$$P = pl \quad [unit: L m^{-2} h^{-1} bar^{-1} m] \quad (3)$$

CHAPTER IV

ZNIC OXIDE / PDMS HYBRID MEMBRANE FOR WATER / OIL SEPARATION

4.1 Introduction

Water/oil separation is an urgent task in energy and environmental fields all over the world including industrial oil emulsions, wastewater treatment, and oil spill accidents in oceans.¹⁶⁴⁻¹⁶⁸ Catastrophic oil spills, such as Deepwater Horizon oil spill in Gulf of Mexico in 2010, impacted over 8000 biological species with economic impact exceeding \$23 billion.¹⁶⁹ Conventional oil removing methods, such as gravity methods, coagulation, and biological treatments, have been used for decades with relative low separation efficiency.¹⁶⁷ Alternative strategies with high separation factors, such as membrane filtration, were applied in the water/oil separation field recently. Hydrophobic membranes with pore size of 10 μm or smaller were designed for separating water/oil emulsion with water droplet size around 10 μm .¹⁷⁰⁻¹⁷² However, such small pore size led to low permeance of viscous oil. A higher feeding pressure was required for a higher flux, which increased the size fluctuation of water droplets and the selectivity was compromised.

Special wettable materials, on the other hand, perform separation based on their distinct affinities to water and oil.^{166,168} Hydrophobic and oleophilic materials could filtrate water while hydrophilic and oleophobic materials could filtrate oil. Feng et al.⁵ fabricated superhydrophobic membranes coated with PTFE, which increased surface roughness and amplified hydrophobicity of surface. Since then, many people were inspired to obtain rough surface by microstructural morphology, such as needle-like,^{173,174}

vertical array,¹⁷⁵ *etc.* Such a combination achieved superhydrophobicity in the membranes with pore size larger than 100 μm , allowing both high separation factor of water/oil and high oil permeance.

ZnO tetrapod crystals with size of 1-10 μm could be used as a coating to roughen surface. They were synthesized by a feasible rapid oxidation reaction in air with a starting material of zinc metal.^{77,165,176,177} The ZnO crystals were then spray-coated onto a stainless-steel mesh forming a layer of needle-like microstructure facing upward. The resulted needle bed created a rough substrate which further amplified the hydrophobicity of a SiO_2 layer coated afterwards. A solution of tetraethyl orthosilicate (TEOS) was spray coated onto the membrane followed by hydrolysis and condensation *in-situ* to form a SiO_2 layer. The superhydrophobic membranes with water contact angle (CA) over 150° separated water and oil efficiently.

Here, we demonstrated a modified procedure that produced ZnO tetrapod crystals continuously. The ZnO tetrapod crystals and a commercially available polydimethylsiloxane (PDMS) Sylgard® 184 were spray coated on a stainless-steel mesh with excellent hydrophobicity and oleophilicity that performed efficient water/oil separation.

4.2 Synthesis of Zinc Oxide Tetrapod Crystals

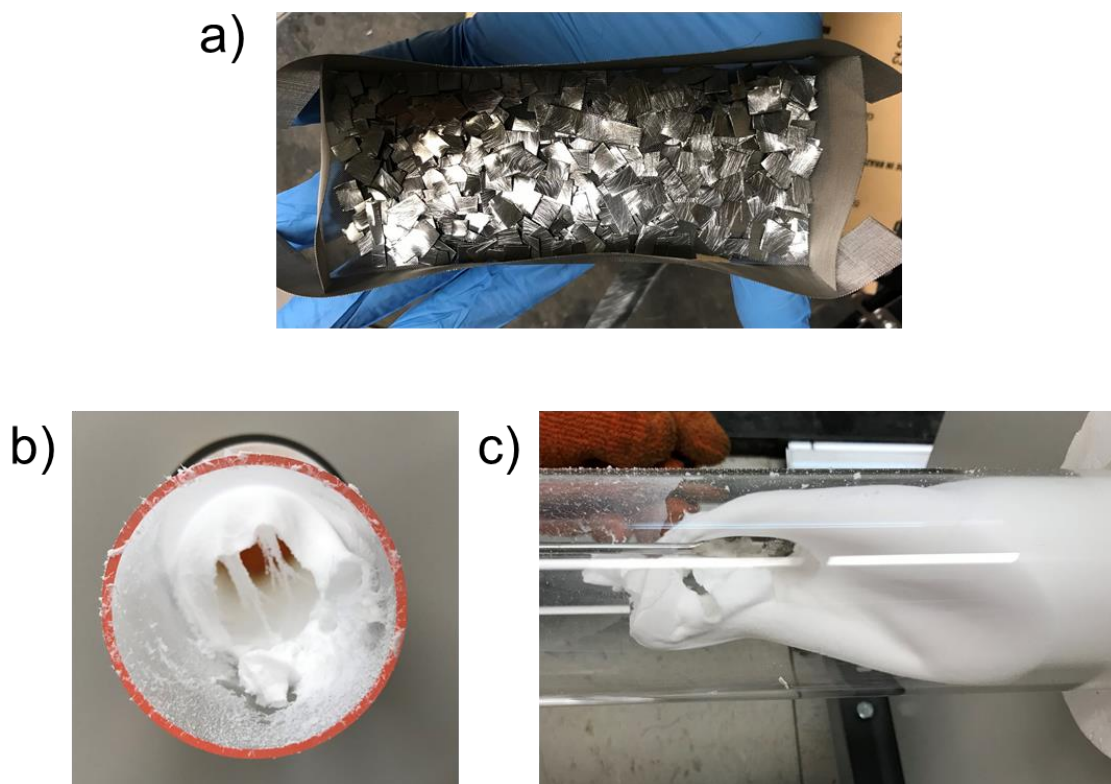


Figure 58. a) Pretreated zinc samples in a sample boat made of stainless-steel mesh; b) and c) white fluffy zinc oxide products in tube.

Zinc oxide tetrapod crystals were synthesized using 99% zinc by an open-end tube furnace. The surface of zinc was sanded in advance to increase surface roughness facilitating the nucleation of crystals. A “sample boat” made of a stainless-steel mesh filled with pretreated zinc samples (**Figure 58 a**) was placed in the center of quartz tube. Air was blown into the tube from one end to trigger the oxidation reaction. The other end of tube was covered by a piece of aluminum foil to prevent zinc vapor (zinc boiling point

907 °C) and zinc oxide product being blown away. The foil paper was punched with pinholes for air circulation.

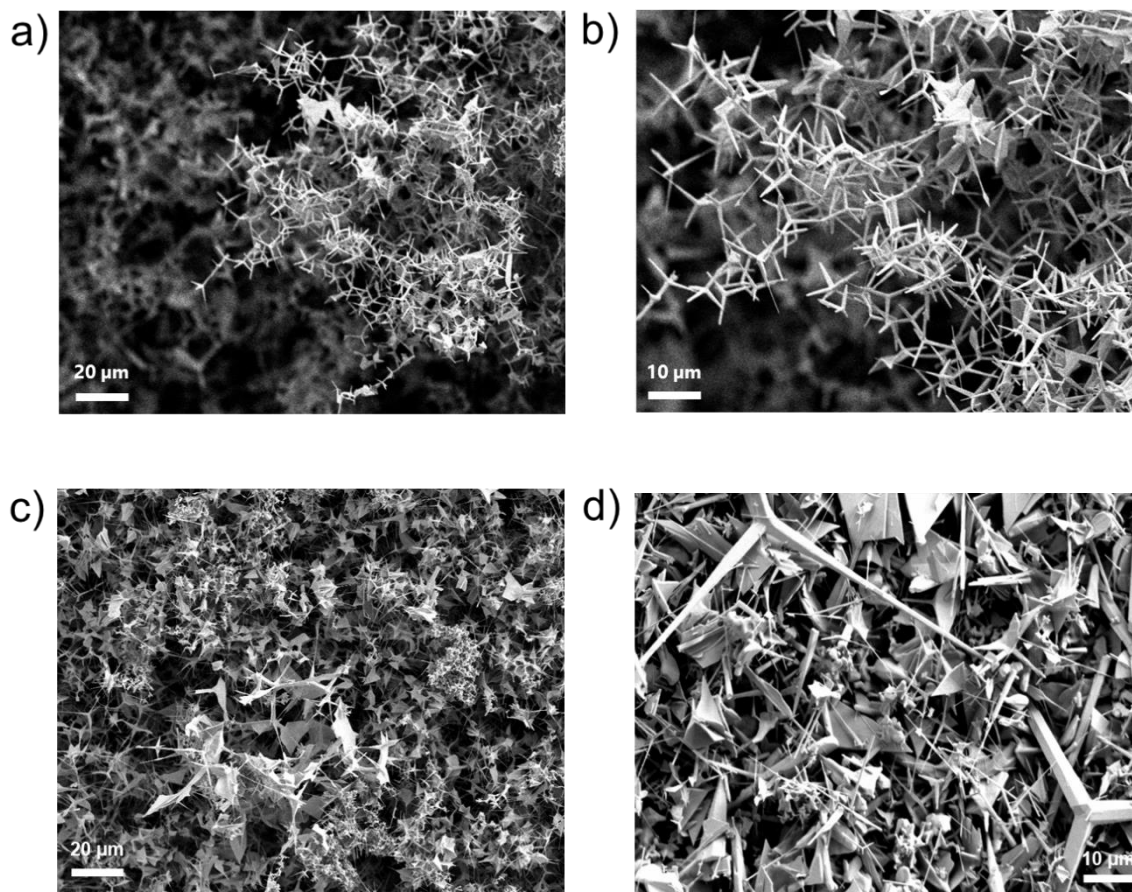


Figure 59. SEM pictures of ZnO crystals. a) tetrapod crystalline structure and b) the zoomed-in SEM picture of a); c) lamella crystalline structure; d) commercially ZnO crystals

The quality of zinc oxide tetrapod crystal is determined by reaction temperature and time. The reaction temperature was set at 930 °C. Above 900 °C, zinc was ignited indicating rapid nucleation of zinc oxide crystal. However, the reaction would proceed too fast to be controlled with produced crystals larger than desired size when the temperature was above 950 °C. The reaction time was controlled to be 3 min. Shorter duration led to

low conversion while longer reaction time resulted into overgrowth of the zinc oxide crystals. In the latter case, the tetrapod crystals (**Figure 59 a, b**) turned into lamella type crystals (**Figure 59 c**). With proper reaction temperature and time as well as assistance of air, white fluffy zinc oxide with tetrapod crystals and size of 5-10 μm (**Figure 58 b, c** and **Figure 59 a, b**) were synthesized. In comparison, commercially available zinc oxide tetrapod crystals showed a much broader size distribution, containing crystals as large as 70 μm (**Figure 58 d**), which could cause clogging problem during spray coating process.

Although the reaction time of zinc oxide crystal was as short as 3 min, the overall production rate of zinc oxide crystals was low because of the small loading capacity of the sample holder and slow heating and cooling cycle of the tube furnace from room temperature to 930 °C. A better production process design was in demand for continuous production. Two strategies were proposed. In the first strategy, the furnace was kept at 930 °C. A tube loaded with zinc pieces was put in the furnace. The reaction was kept for 3 min after zinc was ignited. The tube was then moved out of furnace and another tube loaded with zinc pieces was put in to start the next cycle. The advantage of this strategy is that the tube was used as sample holder, which increased the loading capacity of zinc samples significantly. However, the operational safety risk to move a 3-inch tube out of furnace at 930 °C is still too high for large scale industrial production.

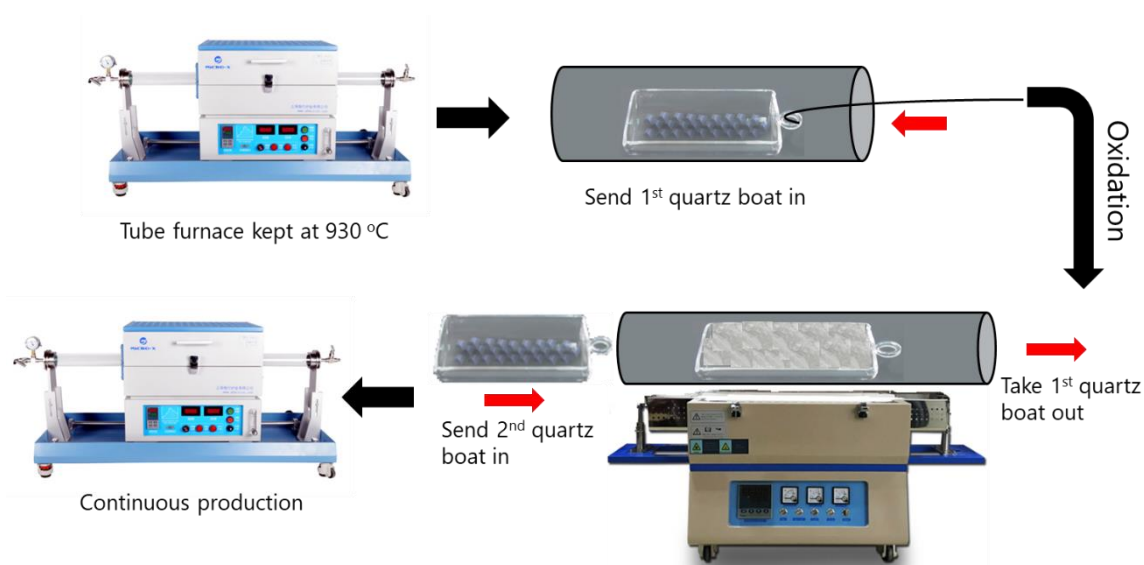


Figure 60. Continuous production cycle of zinc oxide tetrapod crystals

In the second strategy, the tube was kept in furnace at 930 °C. A sample boat loaded with zinc was put into the tube. After the 3-min reaction, the sample boat was moved out of furnace and another sample boat loaded with zinc was put in to start the next cycle (**Figure 60**). Quartz sample boats were used because the sample holders made of stainless steel or aluminum oxide couldn't survive during such a temperature drop. This design would prevent the safety risk of operating the large hot tube. This strategy has limitation that commercially available quartz boats were not big enough fully utilize the space in the tube. Customized quartz boats could solve this problem. In a typical zinc oxide production using this design, 5 batches of zinc oxide were synthesized in a row with yield ranging from 40.9% – 56.2% with products in each batch ranging from 5.6 g to 7.7 g.

4.3 Spray Coating of Hydrophobic Hybrid Membranes

Prior to spray coating, zinc oxide crystals produced from the procedure described in section 4.2 were suspended in isopropanol and sonicated in water bath for 5 min. By sonication, zinc oxide tetrapods were dispersed and formed a uniform suspension. All zinc oxide crystals would precipitate at the bottom of the vessel after several minutes. However, the temporarily suspended zinc oxide could be separated from impurities in the sample, such as unreacted zinc metal, and oversize crystals, by pouring the upper layer of the suspension into another container. The sonication was controlled within 5 mins in a water-bath sonicator to prevent breaking of the tetrapod crystals.

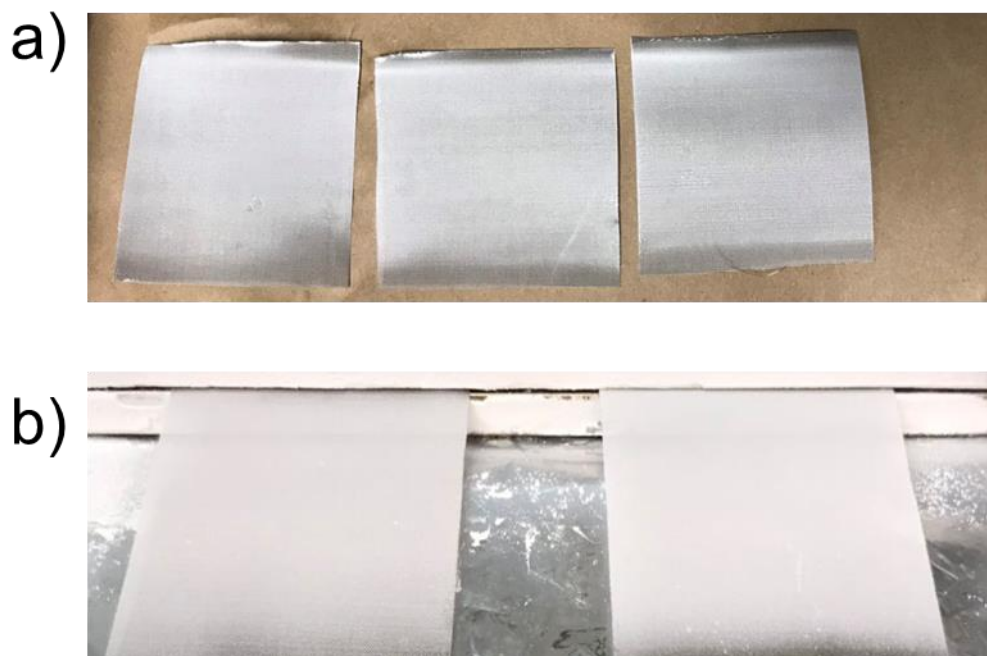


Figure 61. Spray coating of ZnO on stainless steel mesh with density of a) 7 mg/cm² and b) 21 mg/cm².

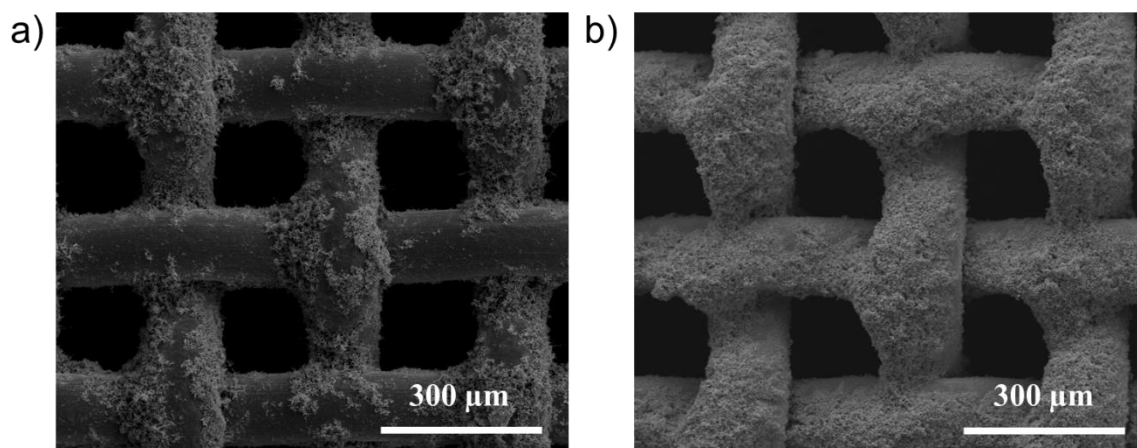


Figure 62. SEM pictures of spray-coated membranes (80 x80) with zinc oxide density a) 7 mg/cm² and b) 21 mg/cm².

The suspension of zinc oxide in isopropanol was then transferred into an airbrush and spray coated onto a stainless-steel mesh over a hot plate. The hot plate was heated to 180 °C to accelerate evaporation of isopropanol. The factors that determined the quality of the coated membrane, such as spray coating density, spray pressure and pore size of the membrane, were studied. Spray coating density is the amount of zinc oxide coated on the membrane per unit area. It was calculated by the weight of coated zinc oxide divided by the area of membrane. Spray pressure is the outlet pressure of pump. The coverage of zinc oxide on an 80 × 80 membrane (180 µm pore size) with spray coating density of 7 mg/cm² and 21 mg/cm² were shown in **Figure 61**. The membrane with spray coating density of 21 mg/cm² clearly exhibited a much better coverage than that of 7 mg/cm², confirmed by SEM pictures in **Figure 62**. As the pore size of the membrane was decreased from 180 µm to 120 µm (120x120 mesh size) to 105 µm (150x150 mesh size), the coated zinc oxide

crystals with same coating density 21 mg/cm^2 partially or fully covered the pores in membrane (**Figure 63**), which diminished the permeance of oil.

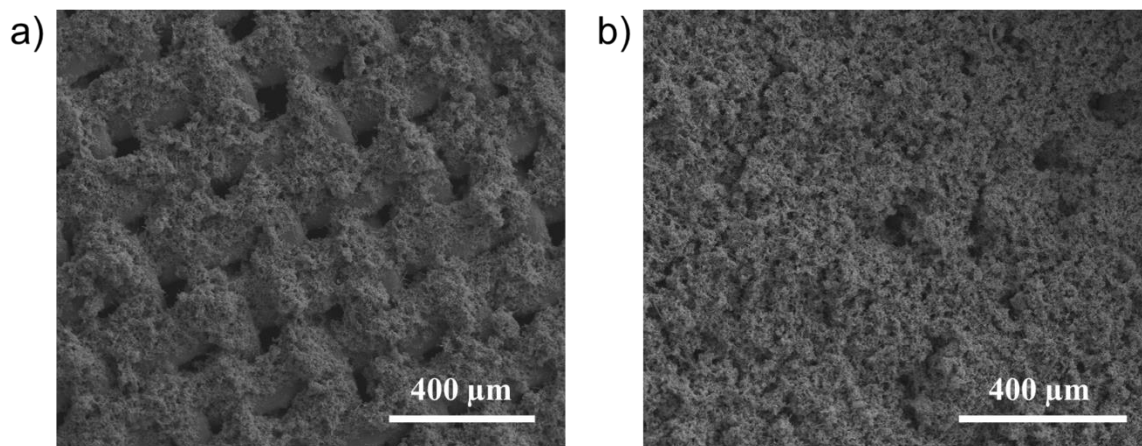


Figure 63. SEM pictures of coated a) 120×120 mesh and b) 150×150 mesh with zinc oxide density of 21 mg/cm^2

After coating of the zinc oxide crystals, TEOS dissolved in a solution of ethanol / water with ammonia was then spray-coated onto the membrane by airbrush. A layer of TEOS covered on the zinc oxide crystals underwent hydrolysis reaction, followed by condensation and polycondensation reactions to form SiO_2 network eventually (**Figure 64**).¹⁷⁸ The SiO_2 network was supposed to be hydrophobic and provided anti-scratch properties for the coated membrane. Spray coating pressure was tuned at 10 psi. Higher pressure blew the zinc oxide away from the membrane surface (**Figure 66**).

In some cases, the freshly prepared membranes coated with zinc oxide crystals and TEOS were hydrophilic (**Figure 67**). This was probably a result of unreacted hydroxy groups left on the silica surface. The rough surface of zinc oxide tetrapod crystals amplified the surface hydrophilicity. Post-treatment was required. The coated membrane

was soaked in toluene several times to remove organics, unreacted monomers and intermediates left on the membrane. Afterwards, the membrane was dried at 100 °C for 24 h in oven to complete the polycondensation of silanol. The WCA after post treatment was $148.7^\circ \pm 3.3^\circ$ for 120×120 mesh and $146.7^\circ \pm 1.3^\circ$ for 150×150 mesh (**Figure 68 a, b**).

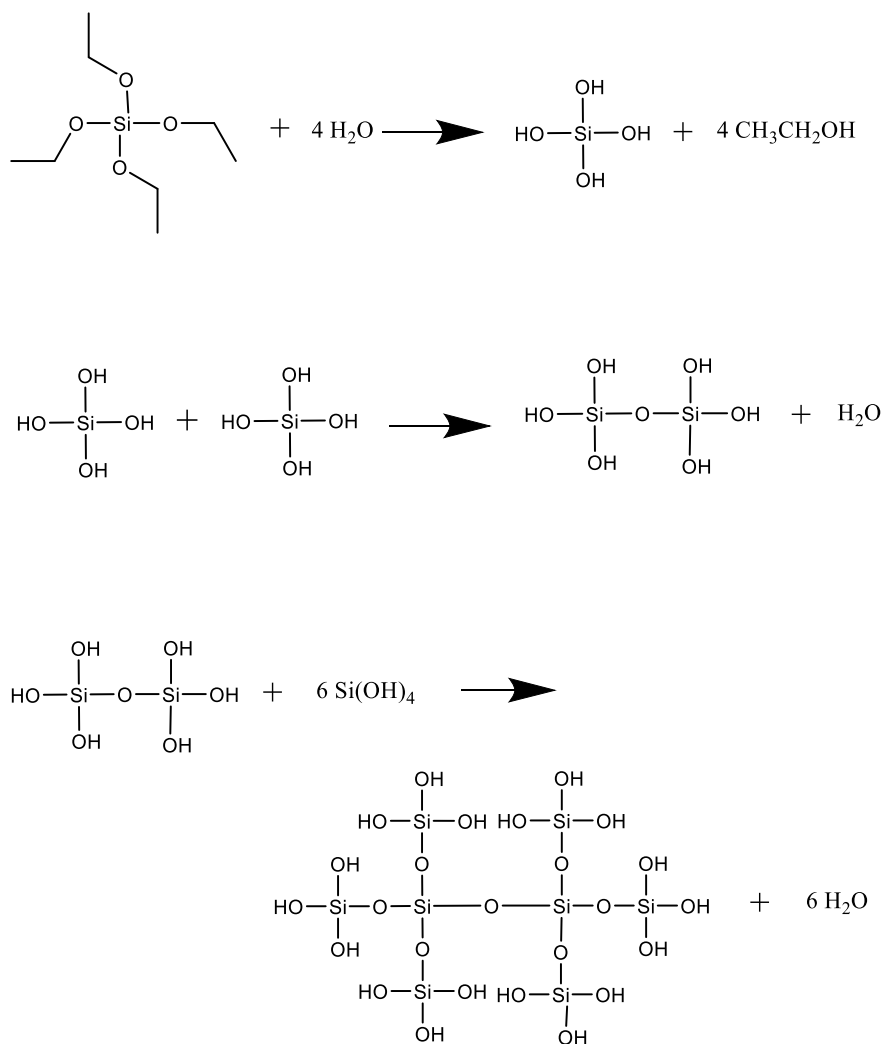


Figure 64. Hydrolysis, condensation and polycondensation of tetraethyl orthosilicate to SiO_2 network

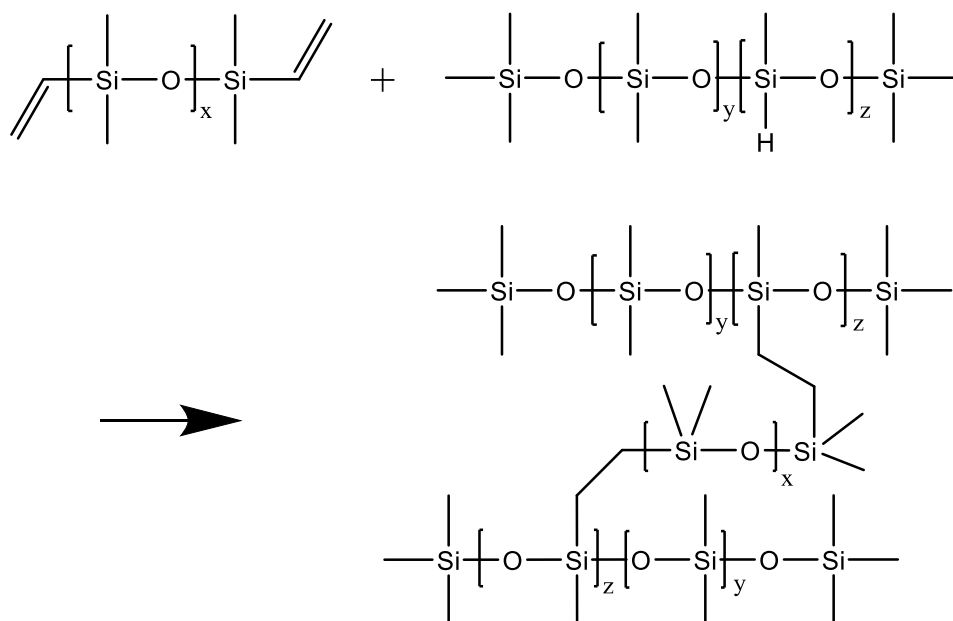


Figure 65. Hydrosilylation of PDMS (Sylgard® 184) precursors.

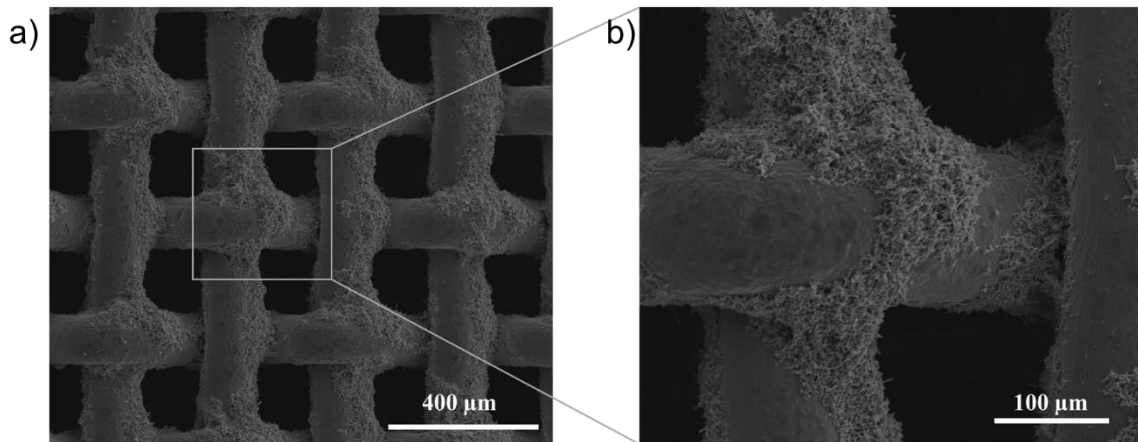


Figure 66. SEM pictures of zinc oxide coated on membrane blew away during spray coating of TEOS with large spray pressure.

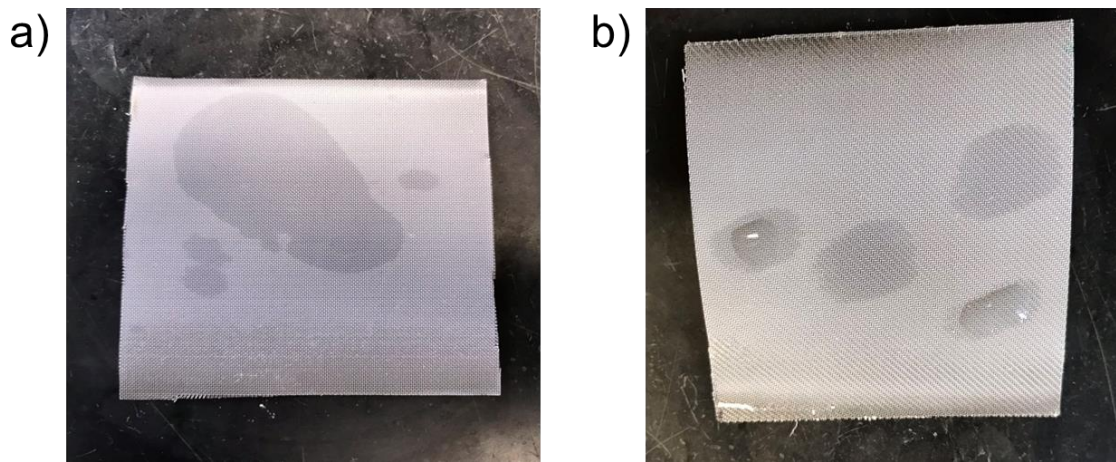


Figure 67. As-coated ZnO / TEOS membrane wetted by water. a) 80×80 mesh and b) 120×120 mesh. Spray coating density 21 mg/cm².

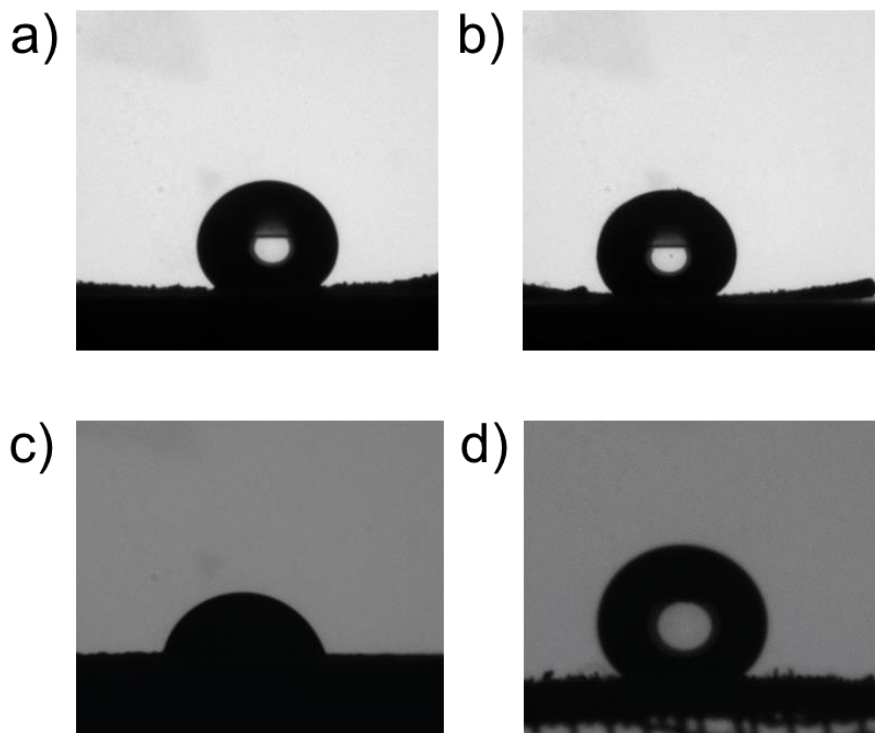


Figure 68. Water contact angle of a) 120×120 ZnO / TEOS membrane ($148.7^\circ \pm 3.3^\circ$); b) 150×150 ZnO / TEOS membrane ($146.7^\circ \pm 1.3^\circ$); c) bare 80×80 stainless-steel mesh (75.9°) and d) 80×80 ZnO / PDMS membrane ($146.2^\circ \pm 1.2^\circ$)

Due to the tedious post treatment procedure and poor anti-scratch properties of ZnO / TEOS membranes, an alternative hydrophobic coating on top of the ZnO crystals was explored. PDMS, a silicon-based polymer with methyl end groups, is a hydrophobic silicone with good thermal and chemical stability and anti-aging properties.^{179,180} Sylgard® 184 is a two-part silicone elastomer and could be cured at room temperature or elevated temperature with less time through a hydrosilylation reaction (**Figure 65**).¹⁸¹ Sylgard® 184 dissolved in hexane was spray-coated onto a mesh coated with ZnO crystals to replace coating of TEOS. After curing, the water contact angle of the ZnO / PDMS membrane was 146.2° (**Figure 68d**), much higher than WCA of 75.9° for bare a stainless-

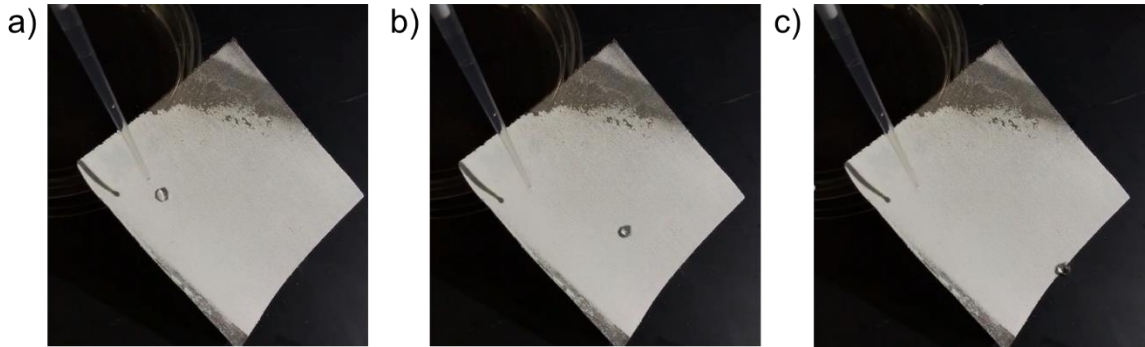


Figure 69. A water droplet rolls off from a tilted ZnO / PDMS membrane within 0.2 seconds. Water shedding angle (WSA) = 8° .

steel mesh (**Figure 68 c**) and WCA of 108° for pristine PDMS (Sylgard® 184)¹⁸², indicating the importance of a rough surface to PDMS. With such a good hydrophobicity, the water shedding angle (WSA) of the membranes, which is the angle of a tilted surface that water could easily roll off,^{164,183} was as low as 8° (**Figure 69**). This indicates the strong water repellent property of the ZnO / PDMS membranes. The anti-scratch properties of ZnO / PDMS membranes were significantly improved due to the efficient curing of PDMS.

Due to the hydrophobic nature of PDMS, ZnO tetrapod crystals with high quality were not strictly required to achieve WCA $> 140^\circ$ for ZnO / PDMS membranes. **Table 8** listed the performances of membranes coated with the ZnO crystals produced in our lab and membranes coated with the ZnO crystals purchased from a commercial source. Commercial ZnO crystals exhibited poor quality in terms of large size variance and more lamella crystal structure than the lab-made ZnO crystals (**Figure 59**). Shown in **Table 8**, the WCA of Membrane #2 and Membrane #4 coated with two kinds of ZnO crystals also showed large difference (140° vs 125°). However, Membrane #3 and Mesh #5 coated with

ZnO crystals from different sources and a layer of PDMS showed improved WCA (146° and 142°). PDMS did not only provide anti-scratch properties to ZnO layer on the membranes but allowed quality variance in ZnO crystals.

Table 8. Contact angle, anti-scratch, and water/oil separation performance of mesh coated with different materials

Mesh #	ZnO crystal	Silicone	CA	Anti-scratch	Water/oil separation
1	N/A	N/A	78°	N/A	N/A
2	Lab made	N/A	140°	Bad	Good
3	Lab made	Sylgard	146°	Good	Good
4	Commercial	N/A	125°	Bad	Good
5	Commercial	Sylgard	142°	Good	Good

In order to demonstrate the possibility of mass production of the membranes, large 1 foot \times 1 foot meshes were spray-coated with ZnO tetrapod crystals followed by a layer of Sylgard® 184 (**Figure 70**). For the 1 ft² membranes, lower spray coating density 14 mg/cm² was required to achieve a good coverage. The resulting large membranes exhibited excellent hydrophobicity and decent anti-scratch properties.



Figure 70. 1 ft² ZnO / PDMS membrane made in lab.

4.4 Application of Water / Oil Separation

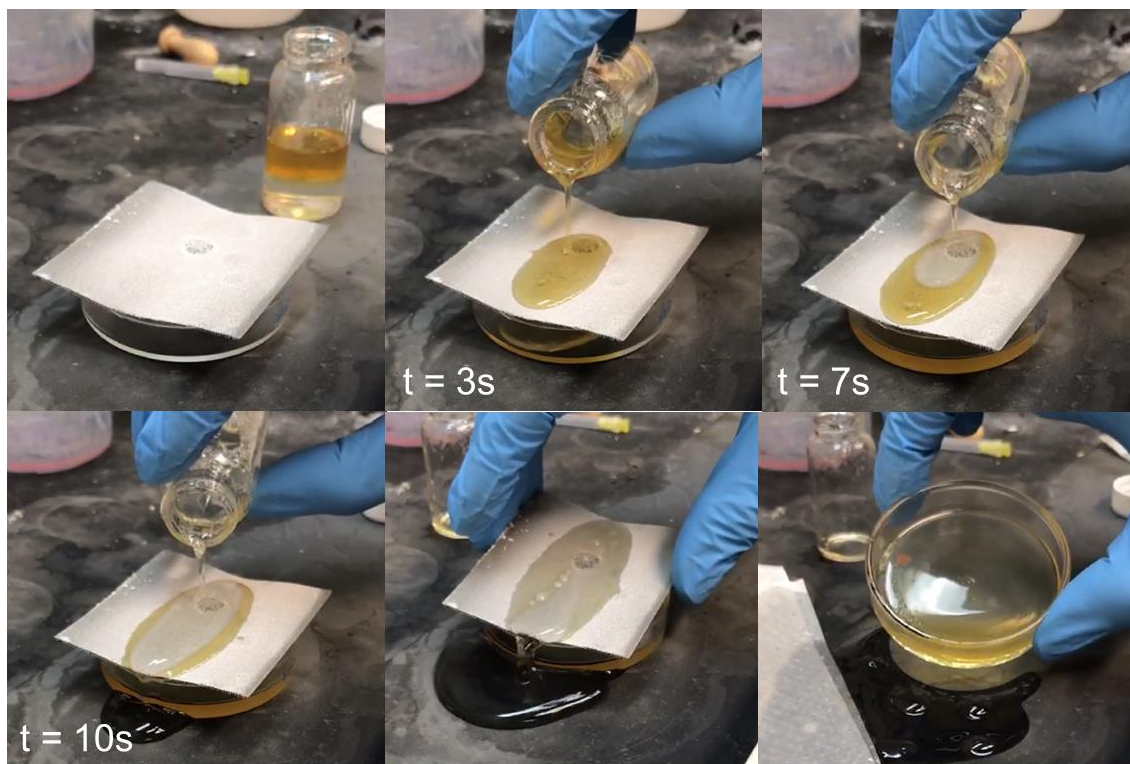


Figure 71. Time lapse images of waste mineral oil / water mixture separated by ZnO / PDMS hybrid membrane. The pore size of the membrane was 180 μm and density of the lab-made ZnO was 21 mg/cm^2 .

The key factors evaluating water/oil separation are the selectivity factors and permeation speed of viscous oil. We expect ZnO / PDMS hybrid membranes to be promising candidates for this type of applications due to the high WCA of the surface and large pore size. The performances of three different hybrid membranes were evaluated: a lab-made ZnO / PDMS membrane (pore size 180 μm , coating density 21 mg/cm^2 , WCA=146°), a commercial ZnO / PDMS membrane (pore size 180 μm , coating density 21 mg/cm^2 , WCA=142°), and a lab-made ZnO / PDMS membrane used for multiple times to test recyclability of hybrid membranes.

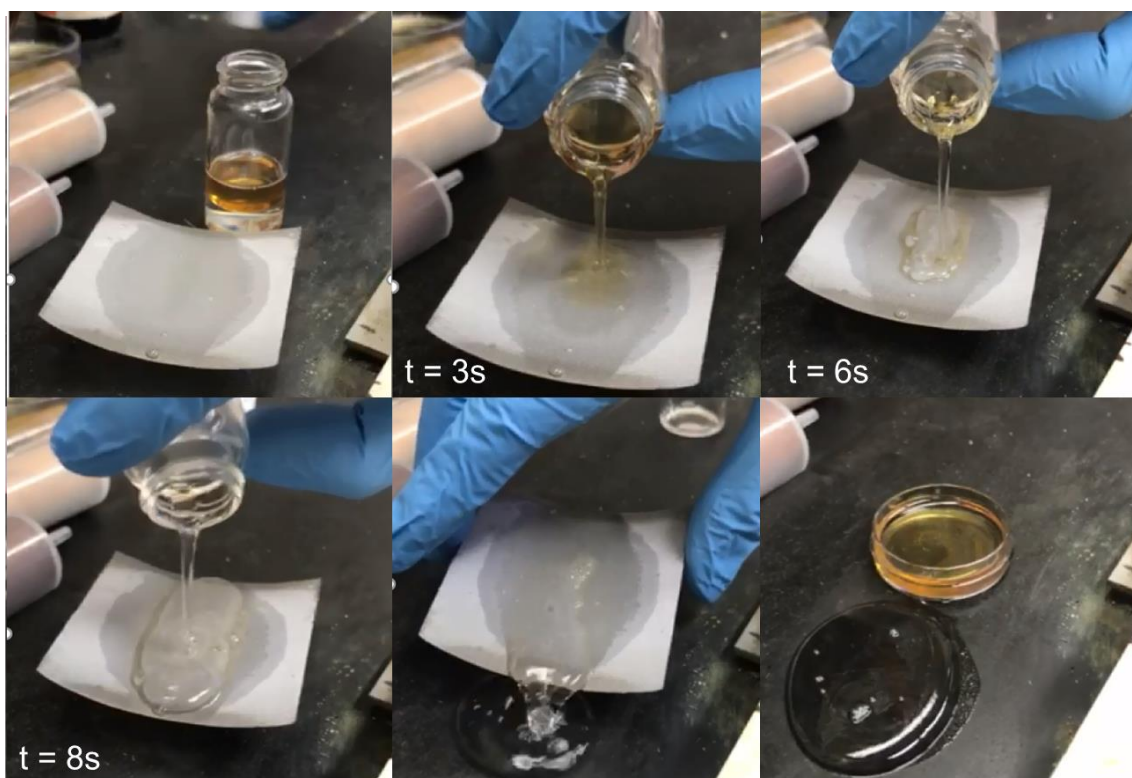


Figure 73. Time lapse images of waste mineral oil / water mixture separated by used lab-made ZnO / PDMS hybrid membrane. The pore size of the membrane was 180 μm and the density of the commercial ZnO was 21 mg/cm^2 .

Inorganic hybrid membranes are advantageous for water/oil separation at elevated temperature due to good thermal stability, which is typically challenging for most polymer membranes. In fact, the hot water/oil mixture is a ubiquitous situation in practical fuel and wastewater separation and recycling in industry.¹⁸⁴⁻¹⁸⁶ Hot water/oil mixture also helps decrease the viscosity of oil to improve oil permeance. Here, waste mineral oil / water mixture at 80 °C was used as the feed in separation tests. As shown in **Figure 71**, the mineral oil with orange color formed a separated layer on top of water. The mixture was poured onto a hybrid membrane coated with the lab-made ZnO crystals. The mineral oil

permeated through the membrane within 7 seconds. Water stayed on top of the membrane. The membrane was then tilted and water rolled off of the surface of the membrane. Furthermore, only mineral oil was collected in the petri dish underneath the hybrid membrane.

Similarly, the mixture of waste mineral oil / water could be efficiently separated using the same method by a commercial ZnO / PDMS membrane and a used ZnO / PDMS membrane (**Figure 72 and 73**). The results indicated that the coating of PDMS allows a better quality tolerance of ZnO crystals in the performance of water/oil separation. The hybrid membranes could also be used multiple times without compromising the separation factors and oil permeation rate.

4.5 Conclusion

A modified procedure that produces ZnO tetrapod crystals in a continuous manner was created, which is essential to scale up the production. The ZnO crystals and TEOS were spray coated onto stainless-steel meshes sequentially and afforded hydrophobic membranes with WCA of 148° . However, the procedure involving polymerizing TEOS to SiO_2 requires demanding dry condition and multiple steps of post treatment. In addition, TEOS requires strict store conditions in N_2 . Alternatively, a commercially available PDMS precursor Sylgard® 184 was used to replace TEOS. PDMS is intrinsically hydrophobic with a simple curing process and anti-scratch property. The ZnO / PDMS hybrid membranes exhibited hydrophobicity with WCA of 146° and WSA of only 8° . The hybrid membranes showed efficient separation towards water/oil mixture at elevated

temperature due to hydrophobicity and large pore size. These membranes could be used in multiple cycles, promising their potential large-scale application.

4.6 Experimental Section

4.6.1 Synthesis of Zinc Oxide Tetrapod Crystals

ZnO tetrapod crystals were synthesized through a modified procedure based on a literature report.¹⁷⁶ 5 g 99% Zn plates were sanded to create nucleation sites before using. The Zn plates were cut into small pieces and placed in an aluminum oxide sample holder and sent into an open-end tube. The other end of tube was covered with aluminum foil paper with pinholes. The furnace was heated up to 950 °C at a rate of 33 °C/min (maximum speed of tube furnace). At temperature around 930 °C, the zinc pieces were ignited. The temperature was kept at 930 °C for 5 min and cooled down automatically. A fan was used to blow air into the tube intermittently. After the temperature was cooled down to RT, the sample holder was taken out of the tube. White, fluffy and soft solid was obtained.

Continuous ZnO production was described as following. The tube furnace was kept at 930 °C and sanded Zinc pieces in a quartz sample boat were sent into the tube. Zinc was first transformed into vapor and caused a temperature drop. After temperature was raised to 930 °C again, zinc was ignited and the oxidation began. Air was blown into the tube intermittently by a fan. After a 3-min reaction, the quartz boat was taken out of the tube and another quartz boat loaded with treated zinc pieces was sent into the tube to start another reaction.

4.6.2 Preparation of ZnO / TEOS and ZnO / PDMS Hybrid Membranes

Generally, to coat a 6 cm × 6 cm steel mesh (pore size 120 μm), 280-800 mg ZnO tetrapod crystals (corresponding to spray coating density 7-21 mg/cm²) were added into 20 mL isopropyl alcohol and bath sonicated for 3 min. The suspension was transferred into another container while the grey and chunky particles that precipitated at the bottom were discarded. The mixture was then transferred into a Master® airbrush with nozzle size of 0.5 mm. A stainless-steel mesh was placed over a hot plate at 180 °C. The hot temperature shortened the evaporation time of isopropanol. ZnO in isopropanol was sprayed on the surface of mesh with the outlet pressure of 10 psi. Proper shaking of airbrush was needed to prevent ZnO from precipitating at the bottom of the airbrush container.

After that, TEOS solution composed of 17 mL ethanol, 0.23 mL ammonium water, 4.5 mL DI water, and 0.112 mL TEOS was transferred into airbrush immediately (TEOS slowly decomposed in water). The temperature of the hot plate was kept at 180 °C. The TEOS solution was sprayed onto the membrane coated with ZnO with an outlet pressure of 8 psi. The spray coating of TEOS solution was slower than that of ZnO in isopropanol as evaporation of water/ethanol required longer time. After spray coating, the membrane was washed by toluene for three times and dried in an oven at 100 °C for 24 h. The completion of polycondensation reaction of TEOS was proven by WCA > 145°.

Sylgard® 184 was used to replace TEOS solution and spray coated onto the membrane coated with ZnO. Precursor and curing agent with a ratio of 10:1 in Sylgard® 184 was dissolved in 10 mL hexane. For 0.75 g ZnO crystals, 0.1g Sylgard® precursor

was used for coating. The Sylgard® was cured at 150 °C for 3h or at RT for 24h. No post-treatment was required.

A large 1 ft² ZnO / PDMS hybrid membrane was prepared using the following procedure. 16 g ZnO was sonicated in 300 mL isopropanol for 5 min. The upper layer of mixture was poured into another beaker and sprayed on to the membrane heated by a hot plate and IR lamps. The spray coating density of ZnO was 14 mg/cm². 0.3 g Sylgard® in hexane was sprayed coated afterwards and cured for a day. The membranes possessed good hydrophobicity.

4.6.3 Water/oil Separation of ZnO / PDMS Hybrid Membrane

A 6 × 6 cm² hybrid membrane made of lab-made ZnO tetrapods, and a 6 × 6 cm² hybrid membrane made from commercial ZnO tetrapods were used for water/oil separation. The membranes were placed on top of a petri dish without any pre-treatment. The waste mineral oil / water mixture in a 20 mL vial was heated at 80 °C before use. The water/oil mixture was poured onto the hybrid membranes. Oil readily permeated through the membranes while water stayed on top of the membranes. After the test, the lab-made ZnO / PDMS hybrid membrane was used for another multiple water/oil separation tests to prove the recyclability.

CHAPTER V

CONCLUSIONS

5.1 Porous Polymer Networks and Their Membranes for Selective Adsorption and Organic Solvent Nanofiltration

5.1.1 Summary

Methanesulfonic acid (MSA) stood as an ideal option to mediate aldol triple condensation (ATC) that converted aromatic diacetyl- or triacetyl- substituted aromatic monomers into porous polymer networks (PPNs). Compared with other reported catalysts of ATC, MSA served as the catalyst and the solvent simultaneously, allowing homogenous reaction to give PPNs with the highest BET surface area. The optimized reaction temperature was identified based on defect level and porosity of the product. Despite the amorphous nature, PPN showed size-dependent selective adsorption to organic molecules in aqueous solution benefiting from the narrow pore size distribution. These PPNs showed distinct adsorption rate and capacity towards organic dyes depending their molecular size with a cut-off size close to the major pore size of PPN. In addition, the pristine mixture of monomer solution made it possible for solution processing PPN through *in situ* crosslinking. A composite membrane with PPN filled in the pores of carbon fiber paper was prepared to demonstrate the possibility of integrating the adsorption ability of PPN and the mechanical strength of carbon fiber.

Furthermore, free-standing PPN membranes were fabricated by casting the di-/tri-acetyl-functionalized monomer solution in MSA on glass substrates followed by *in-situ* polymerization. Membranes as thin as 150 nm were obtained and confirmed by SEM and

AFM. The PPN membranes showed high porosity with BET surface areas as large as 1235 m²/g. The pore size distribution of *p*-PPN, *m*-PPN, and *tri*-PPN membranes were similar and exhibited correlation with their theoretical pore structures. A majority of pores were smaller than 1.5 nm, suitable for adsorbing or separating small molecules. The crosslinked network and aromatic framework of PPN membranes led to excellent thermal and chemical stability which enables organic solvent nanofiltration (OSN). As expected, benefiting from their narrow pore size distribution, PPN membranes showed high selectivity to organic dyes and demonstrated separation of a mixture of three to four molecular dyes based on their size. The high porosity resulted into high solvent permeability. The PPN membranes performed OSN using feed solution with strong acid or strong base for over 50 hours without observable performance decline. They were also able to withstand treatments of 18 M H₂SO₄ and 5M MeONa without compromising OSN performance. The integrated performances of selectivity, permeability and stability under extreme conditions make the PPN membranes promising candidates for challenging OSN applications.

5.1.2 Perspective

In order to obtain large area and mechanically strong membranes for OSN tests, PPN membranes with diameter of 4.7 cm and thickness of 100 μm were prepared. Despite the high intrinsic permeability of the PPN materials, such a thickness limited the permeance of PPN membranes, compared with other reported membranes with nanometer scale thickness. There are two strategies to solve this problem.

The first strategy is to fabricate PPN thin films on ultrafiltration membranes *in-situ* which would provide good mechanical support in OSN. This strategy has been widely applied in many examples of OSN membranes with sub-micrometer thickness. Our membrane fabrication method was able to prepare free-standing PPN membranes with thickness of 150 nm. However, the solvent and catalyst MSA used in the reaction at 110 °C would destroy most commercial polymeric ultrafiltration membranes. Carbon or inorganic ultrafiltration membranes, on the other hand, could survive in hot MSA. Carbon ultrafiltration support was reported but not commercially available.¹⁸⁷ Inorganic membranes such as ZrO₂ membranes with working range of pH 0-14 are available but expensive (around \$50/membrane).

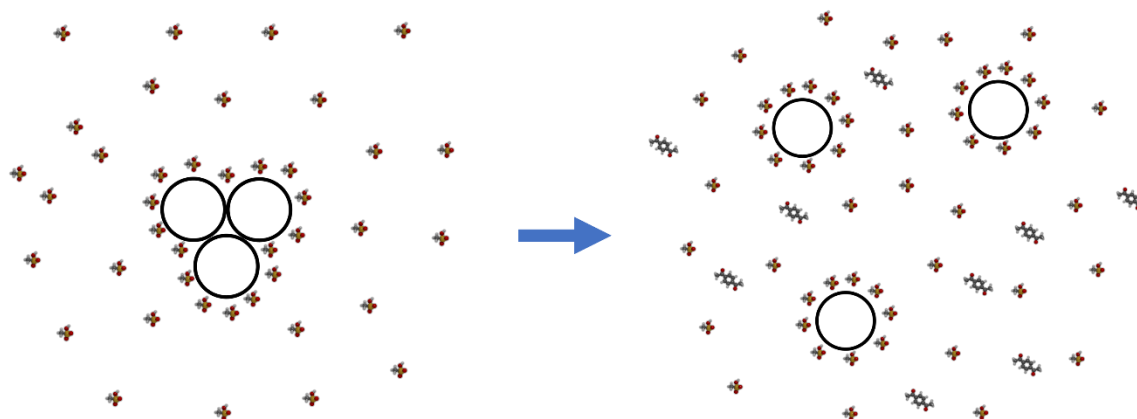


Figure 74. Proposed method of carbon nanotube dispersed in MSA followed by introduction of PPN monomer which would form crosslinked network.

The other possible method is to increase the mechanical strength of PPN membranes so that free standing PPN thin films could be used for OSN directly. We applied a copolymerization between monomers of *p*-PPN and PPN2. The diphenyl ether based monomers introduced flexibility and elongation in the resulting co-PPN

membranes, which improved the mechanical strength. However, the compromised structural rigidity led to a much poorer OSN selectivity. Another strategy is to introduce additives / fillers such as carbon nanotube in the PPN network to improve the mechanical strength. Carbon nanotube with size 2-3 nm (larger than intrinsic pore size of PPN) could be dispersed into MSA (**Figure 74**).¹⁸⁸ The PPN monomers can be then dissolved in the dispersion and polymerized into PPN. Diameter of the carbon nanotubes is larger than intrinsic pores but would be fitted into defects in PPN. Such a mixed matrix membrane can potentially solve the problem of poor mechanical strength at low thickness.

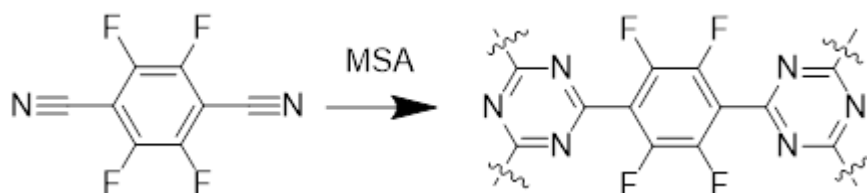


Figure 75. Synthetic route of F-CTF membrane preparation.

MSA is a practical catalyst in triple condensation. A synthetic route of fluorinated covalent triazine framework (F-CTF) membrane is proposed in **Figure 75**. F-CTF with outstanding ability to capture CO₂ was synthesized by a heterogeneous reaction with the catalyst of ZnCl₂ at 400 °C.¹⁸⁹ The preparation of F-CTF membranes, however, has not been reported yet. A preliminary reaction was performed using trifluoromethanesulfonic acid as catalyst and solvent at 100 °C to trigger reaction of F-CTF. The IR spectrum of the product showed disappeared peaks representing cyanide bond at 2252 cm⁻¹ and appearance of peaks at 1674, 1470, 1261, and 804 cm⁻¹ representing triazine groups (**Figure 76**). The resulting powder product could be dissolved in DMF revealing the low

conversion of this reaction. With MSA, however, the reaction temperature could be raised to 150 °C and above, which can lead into a higher conversion and membrane formation.

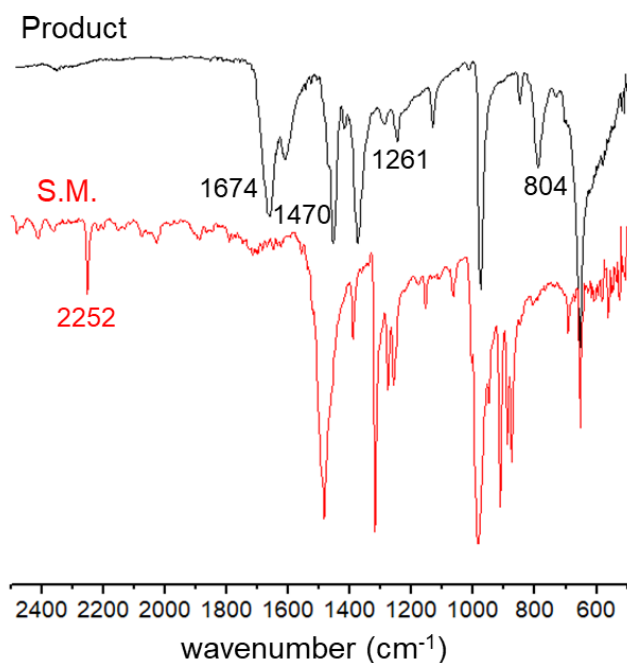


Figure 76. FTIR of starting materials of F-CTF compared with the product.

5.2 ZnO / PDMS hybrid membranes for Water /oil Separation

Zinc oxide tetrapod crystals with micrometer size was used for an underlying coating of a hydrophobic surface to increase the surface roughness. Previously, silica surface condensed by TEOS was used to cover the ZnO crystals. The coating of TEOS has been replaced by a commercial PDMS coating to address the problem of low defect tolerance in TEOS reaction. This feasible coating method, along with the revised continuous production method of ZnO crystals, made it possible for scalable fabrication of hybrid membranes with large area of 1 ft² in lab. With the coating of ZnO crystals and

PDMS, the WCA of the membrane was improved from 76° to 146°, close to that of a superhydrophobic surface. The resulting oleophilic and hydrophobic membranes demonstrated efficient separation towards water / oil mixture at room temperature and elevated temperature.

5.2.2 Perspective

ZnO crystals could trigger the photo-initiated polymerization of certain polymers (**Figure 77**). ZnO tetrapod crystals in this situation would serve dual purposes as a catalyst and surface roughening agent. The coating incorporated with ZnO crystals and hydrophobic polymer would display water repelling property. The curing process relying on light instead of heating would be practical to be used in outdoor coating, such as the external wall of buildings with self-cleaning property.

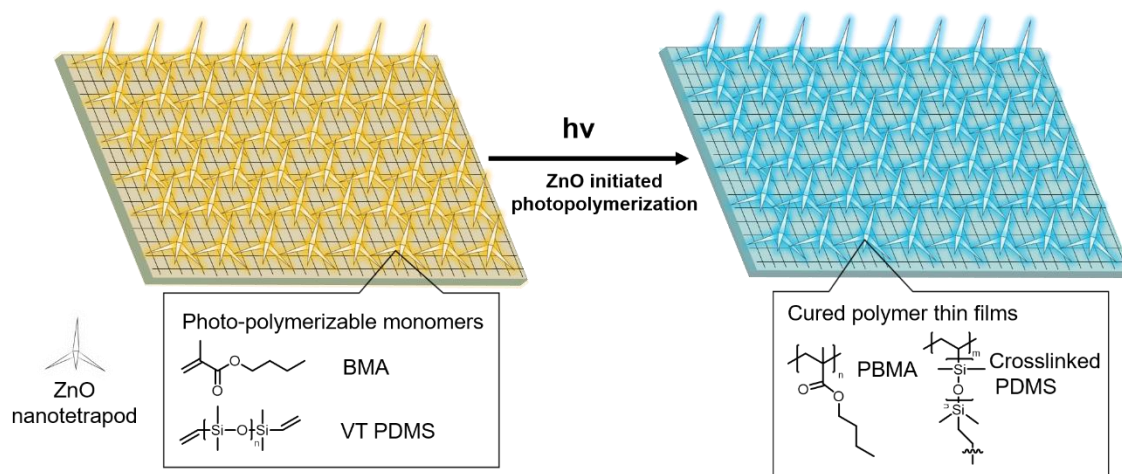


Figure 77. Scheme of ZnO crystals used for catalyst in photo-initiator in polymerization.

REFERENCE

- (1) Marchetti, P.; Jimenez Solomon, M. F.; Szekely, G.; Livingston, A. G. Molecular Separation with Organic Solvent Nanofiltration: A Critical Review, *Chem. Rev.* **2014**, *114*, 10735-10806.
- (2) Laboratory, O. R. N. *Materials for Separation Technologies. Energy and Emission Reduction Opportunities*, 2005.
- (3) Kandambeth, S.; Biswal, B. P.; Chaudhari, H. D.; Rout, K. C.; Shebeeb, K. H.; Mitra, S.; Karak, S.; Das, A.; Mukherjee, R.; Kharul, U. K.; Banerjee, R. Selective Molecular Sieving in Self-Standing Porous Covalent-Organic-Framework Membranes, *Adv. Mater.* **2017**, *29*, 1603945.
- (4) Byun, J.; Patel, H. A.; Thirion, D.; Yavuz, C. T. Charge-specific size-dependent separation of water-soluble organic molecules by fluorinated nanoporous networks, *Nat. Commun.* **2016**, *7*, 13377.
- (5) Feng, L.; Zhang, Z.; Mai, Z.; Ma, Y.; Liu, B.; Jiang, L.; Zhu, D. A Super-Hydrophobic and Super-Oleophilic Coating Mesh Film for the Separation of Oil and Water, *Angew. Chem. Int. Ed.* **2004**, *43*, 2012-2014.
- (6) Liao, Q.; Ke, C.; Huang, X.; Zhang, G.; Zhang, Q.; Zhang, Z.; Zhang, Y.; Liu, Y.; Ning, F.; Xi, K. Catalyst-free and efficient fabrication of highly crystalline fluorinated covalent organic frameworks for selective guest adsorption, *J. Mater. Chem. A* **2019**, *7*, 18959-18970.
- (7) Liang, B.; Wang, H.; Shi, X.; Shen, B.; He, X.; Ghazi, Z. A.; Khan, N. A.; Sin, H.; Khattak, A. M.; Li, L.; Tang, Z. Microporous membranes comprising conjugated polymers with rigid backbones enable ultrafast organic-solvent nanofiltration, *Nat. Chem.* **2018**, *10*, 961-967.
- (8) Lively, R. P.; Sholl, D. S. From water to organics in membrane separations, *Nat. Mater.* **2017**, *16*, 276-279.

- (9) Huang, H.-J.; Ramaswamy, S.; Tschirner, U. W.; Ramarao, B. V. A review of separation technologies in current and future biorefineries, *Separation and Purification Technology* **2008**, *62*, 1-21.
- (10) Takht Ravanchi, M.; Kaghazchi, T.; Kargari, A. Application of membrane separation processes in petrochemical industry: a review, *Desalination* **2009**, *235*, 199-244.
- (11) Vandezande, P.; Gevers, L. E. M.; Vankelecom, I. F. J. Solvent resistant nanofiltration: separating on a molecular level, *Chem. Soc. Rev.* **2008**, *37*, 365-405.
- (12) Bernardo, P.; Drioli, E.; Golemme, G. Membrane Gas Separation: A Review/State of the Art, *Industrial & Engineering Chemistry Research* **2009**, *48*, 4638-4663.
- (13) Ali, I.; Gupta, V. K. Advances in water treatment by adsorption technology, *Nature Protocols* **2006**, *1*, 2661-2667.
- (14) Delgado, N.; Capparelli, A.; Navarro, A.; Marino, D. Pharmaceutical emerging pollutants removal from water using powdered activated carbon: Study of kinetics and adsorption equilibrium, *J. Environ. Manage.* **2019**, *236*, 301-308.
- (15) Bai, Z.; Hu, C.; Liu, H.; Qu, J. Selective adsorption of fluoride from drinking water using NiAl-layered metal oxide film electrode, *Journal of Colloid and Interface Science* **2019**, *539*, 146-151.
- (16) Wu, J.; Xu, F.; Li, S.; Ma, P.; Zhang, X.; Liu, Q.; Fu, R.; Wu, D. Porous Polymers as Multifunctional Material Platforms toward Task-Specific Applications, *Adv. Mater.* **2019**, *31*, 1802922.
- (17) Sayari, A.; Belmabkhout, Y.; Serna-Guerrero, R. Flue gas treatment via CO₂ adsorption, *Chem. Eng. J.* **2011**, *171*, 760-774.

- (18) Lu, W.; Yuan, D.; Sculley, J.; Zhao, D.; Krishna, R.; Zhou, H.-C. Sulfonate-Grafted Porous Polymer Networks for Preferential CO₂ Adsorption at Low Pressure, *J. Am. Chem. Soc.* **2011**, *133*, 18126-18129.
- (19) Guo, X.; Zhang, S.; Shan, X.-q. Adsorption of metal ions on lignin, *J. Hazard. Mater.* **2008**, *151*, 134-142.
- (20) Qu, J. Research progress of novel adsorption processes in water purification: A review, *Journal of Environmental Sciences* **2008**, *20*, 1-13.
- (21) Alsaiee, A.; Smith, B. J.; Xiao, L.; Ling, Y.; Helbling, D. E.; Dichtel, W. R. Rapid removal of organic micropollutants from water by a porous β -cyclodextrin polymer, *Nature* **2016**, *529*, 190-194.
- (22) Yang, H. Y.; Han, Z. J.; Yu, S. F.; Pey, K. L.; Ostrikov, K.; Karnik, R. Carbon nanotube membranes with ultrahigh specific adsorption capacity for water desalination and purification, *Nat. Commun.* **2013**, *4*, 2220.
- (23) Ayawei, N., Ebelegi, A.N., Wankasi, D. Modelling and interpretation of adsorption isotherms, *J. Chem.* **2017**, 3039817.
- (24) Faust, S. D.; Aly, O. M. In *Adsorption Processes for Water Treatment*; Faust, S. D., Aly, O. M., Eds.; Butterworth-Heinemann: 1987, p 25-64.
- (25) Langmuir, I. THE ADSORPTION OF GASES ON PLANE SURFACES OF GLASS, MICA AND PLATINUM, *J. Am. Chem. Soc.* **1918**, *40*, 1361-1403.
- (26) Dąbrowski, A. Adsorption — from theory to practice, *Advances in Colloid and Interface Science* **2001**, *93*, 135-224.
- (27) Boparai, H. K.; Joseph, M.; O'Carroll, D. M. Kinetics and thermodynamics of cadmium ion removal by adsorption onto nano zerovalent iron particles, *J. Hazard. Mater.* **2011**, *186*, 458-465.

- (28) Sips, R. On the Structure of a Catalyst Surface, *The Journal of Chemical Physics* **1948**, *16*, 490-495.
- (29) Gimbert, F.; Morin-Crini, N.; Renault, F.; Badot, P.-M.; Crini, G. Adsorption isotherm models for dye removal by cationized starch-based material in a single component system: Error analysis, *J. Hazard. Mater.* **2008**, *157*, 34-46.
- (30) Amin, T. M.; Alazba, A. A.; Shafiq, M. Adsorptive Removal of Reactive Black 5 from Wastewater Using Bentonite Clay: Isotherms, Kinetics and Thermodynamics, *Sustainability* **2015**, *7*.
- (31) Bibby, A.; Mercier, L. Mercury(II) Ion Adsorption Behavior in Thiol-Functionalized Mesoporous Silica Microspheres, *Chem. Mater.* **2002**, *14*, 1591-1597.
- (32) Aguila, B.; Sun, Q.; Perman, J. A.; Earl, L. D.; Abney, C. W.; Elzein, R.; Schlaf, R.; Ma, S. Efficient Mercury Capture Using Functionalized Porous Organic Polymer, *Adv. Mater.* **2017**, *29*, 1700665.
- (33) Loeb, S.; Sourirajan, S. In *Saline Water Conversion—II*; AMERICAN CHEMICAL SOCIETY: 1963; Vol. 38, p 117-132.
- (34) Fonseca Couto, C.; Lange, L. C.; Santos Amaral, M. C. A critical review on membrane separation processes applied to remove pharmaceutically active compounds from water and wastewater, *Journal of Water Process Engineering* **2018**, *26*, 156-175.
- (35) Matsuura, T. Progress in membrane science and technology for seawater desalination — a review, *Desalination* **2001**, *134*, 47-54.
- (36) Luis, P.; Van Gerven, T.; Van der Bruggen, B. Recent developments in membrane-based technologies for CO₂ capture, *Progress in Energy and Combustion Science* **2012**, *38*, 419-448.

- (37) Wijmans, J. G.; Baker, R. W. The solution-diffusion model: a review, *J. Membr. Sci.* **1995**, *107*, 1-21.
- (38) Krishna, R.; Wesselingh, J. A. The Maxwell-Stefan approach to mass transfer, *Chemical Engineering Science* **1997**, *52*, 861-911.
- (39) Mortensen, N. A.; Okkels, F.; Bruus, H. Reexamination of Hagen-Poiseuille flow: Shape dependence of the hydraulic resistance in microchannels, *Physical Review E* **2005**, *71*, 057301.
- (40) Bowen, W. R.; Mohammad, A. W.; Hilal, N. Characterisation of nanofiltration membranes for predictive purposes — use of salts, uncharged solutes and atomic force microscopy, *J. Membr. Sci.* **1997**, *126*, 91-105.
- (41) Celebi, K.; Buchheim, J.; Wyss, R. M.; Droudian, A.; Gasser, P.; Shorubalko, I.; Kye, J.-I.; Lee, C.; Park, H. G. Ultimate Permeation Across Atomically Thin Porous Graphene, *Science* **2014**, *344*, 289-292.
- (42) Tio, K.-K.; Sadhal, S. S. Boundary conditions for stokes flows near a porous membrane, *Applied Scientific Research* **1994**, *52*, 1-20.
- (43) Sampson, R. A. On Stokes's Current Function, *Philosophical Transactions of the Royal Society of London. (A.)* **1891**, *182*, 449-518.
- (44) Shinde, D. B.; Sheng, G.; Li, X.; Ostwal, M.; Emwas, A.-H.; Huang, K.-W.; Lai, Z. Crystalline 2D Covalent Organic Framework Membranes for High-Flux Organic Solvent Nanofiltration, *J. Am. Chem. Soc.* **2018**, *140*, 14342-14349.
- (45) Nakao, S.-I.; Kimura, S. MODELS OF MEMBRANE TRANSPORT PHENOMENA AND THEIR APPLICATIONS FOR ULTRAFILTRATION DATA, *Journal of Chemical Engineering of Japan* **1982**, *15*, 200-205.

- (46) Lonsdale, H. K.; Merten, U.; Tagami, M. Phenol transport in cellulose acetate membranes, *Journal of Applied Polymer Science* **1967**, *11*, 1807-1820.
- (47) Paul, D. R. Reformulation of the solution-diffusion theory of reverse osmosis, *J. Membr. Sci.* **2004**, *241*, 371-386.
- (48) Buekenhoudt, A.; Bisignano, F.; De Luca, G.; Vandezande, P.; Wouters, M.; Verhulst, K. Unravelling the solvent flux behaviour of ceramic nanofiltration and ultrafiltration membranes, *J. Membr. Sci.* **2013**, *439*, 36-47.
- (49) Karan, S.; Jiang, Z.; Livingston, A. G. Sub-10 nm polyamide nanofilms with ultrafast solvent transport for molecular separation, *Science* **2015**, *348*, 1347-1351.
- (50) Bulut, M.; Gevers, L. E. M.; Paul, J. S.; Vankelecom, I. F. J.; Jacobs, P. A. Directed Development of High-Performance Membranes via High-Throughput and Combinatorial Strategies, *Journal of Combinatorial Chemistry* **2006**, *8*, 168-173.
- (51) Vandezande, P.; Gevers, L. E. M.; Paul, J. S.; Vankelecom, I. F. J.; Jacobs, P. A. High throughput screening for rapid development of membranes and membrane processes, *J. Membr. Sci.* **2005**, *250*, 305-310.
- (52) Mertens, P. G. N.; Bulut, M.; Gevers, L. E. M.; Vankelecom, I. F. J.; Jacobs, P. A.; Vos, D. E. D. Catalytic oxidation of 1,2-diols to α -hydroxy-carboxylates with stabilized gold nanocolloids combined with a membrane-based catalyst separation, *Catalysis Letters* **2005**, *102*, 57-61.
- (53) Mertens, P. G. N.; Cuypers, F.; Vandezande, P.; Ye, X.; Verpoort, F.; Vankelecom, I. F. J.; De Vos, D. E. Ag⁰ and Co⁰ nanocolloids as recyclable quasihomogeneous metal catalysts for the hydrogenation of α,β -unsaturated aldehydes to allylic alcohol fragrances, *Applied Catalysis A: General* **2007**, *325*, 130-139.
- (54) Gupta, K. C. Synthesis and evaluation of aromatic polyamide membranes for desalination in reverse-osmosis technique, *Journal of Applied Polymer Science* **1997**, *66*, 643-653.

- (55) Konagaya, S.; Tokai, M.; Kuzumoto, H. Reverse osmosis performance and chlorine resistance of new ternary aromatic copolyamides comprising 3,3'-diaminodiphenylsulfone and a comonomer with a carboxyl group, *Journal of Applied Polymer Science* **2001**, *80*, 505-513.
- (56) Petersen, R. J. Composite reverse osmosis and nanofiltration membranes, *J. Membr. Sci.* **1993**, *83*, 81-150.
- (57) Ismail, A. F.; Lai, P. Y. Effects of phase inversion and rheological factors on formation of defect-free and ultrathin-skinned asymmetric polysulfone membranes for gas separation, *Separation and Purification Technology* **2003**, *33*, 127-143.
- (58) Boussu, K.; Vandecasteele, C.; Van der Bruggen, B. Study of the characteristics and the performance of self-made nanoporous polyethersulfone membranes, *Polymer* **2006**, *47*, 3464-3476.
- (59) Hicke, H.-G.; Lehmann, I.; Malsch, G.; Ulbricht, M.; Becker, M. Preparation and characterization of a novel solvent-resistant and autoclavable polymer membrane, *J. Membr. Sci.* **2002**, *198*, 187-196.
- (60) Roh, I. J.; Park, S. Y.; Kim, J. J.; Kim, C. K. Effects of the polyamide molecular structure on the performance of reverse osmosis membranes, *Journal of Polymer Science Part B: Polymer Physics* **1998**, *36*, 1821-1830.
- (61) Kim, C. K.; Kim, J. H.; Roh, I. J.; Kim, J. J. The changes of membrane performance with polyamide molecular structure in the reverse osmosis process, *J. Membr. Sci.* **2000**, *165*, 189-199.
- (62) Jayarani, M. M.; Kulkarni, S. S. Thin-film composite poly(esteramide)-based membranes, *Desalination* **2000**, *130*, 17-30.
- (63) Jimenez Solomon, M. F.; Bhole, Y.; Livingston, A. G. High flux hydrophobic membranes for organic solvent nanofiltration (OSN)—Interfacial polymerization, surface modification and solvent activation, *J. Membr. Sci.* **2013**, *434*, 193-203.

- (64) Jimenez-Solomon, M. F.; Gorgojo, P.; Munoz-Ibanez, M.; Livingston, A. G. Beneath the surface: Influence of supports on thin film composite membranes by interfacial polymerization for organic solvent nanofiltration, *J. Membr. Sci.* **2013**, *448*, 102-113.
- (65) Robeson, L. M. Correlation of separation factor versus permeability for polymeric membranes, *J. Membr. Sci.* **1991**, *62*, 165-185.
- (66) Robeson, L. M. The upper bound revisited, *J. Membr. Sci.* **2008**, *320*, 390-400.
- (67) Gin, D. L.; Noble, R. D. Designing the Next Generation of Chemical Separation Membranes, *Science* **2011**, *332*, 674-676.
- (68) Villalobos, L. F.; Huang, T.; Peinemann, K. V. Cyclodextrin Films with Fast Solvent Transport and Shape-Selective Permeability, *Adv. Mater.* **2017**, *29*, 1606641.
- (69) Liu, J.; Hua, D.; Zhang, Y.; Japip, S.; Chung, T. S. Precise Molecular Sieving Architectures with Janus Pathways for Both Polar and Nonpolar Molecules, *Adv. Mater.* **2018**, *30*, 1705933.
- (70) Jimenez-Solomon, M. F.; Song, Q.; Jelfs, K. E.; Munoz-Ibanez, M.; Livingston, A. G. Polymer nanofilms with enhanced microporosity by interfacial polymerization, *Nat. Mater.* **2016**, *15*, 760.
- (71) Dey, K.; Pal, M.; Rout, K. C.; Kunjattu H, S.; Das, A.; Mukherjee, R.; Kharul, U. K.; Banerjee, R. Selective Molecular Separation by Interfacially Crystallized Covalent Organic Framework Thin Films, *J. Am. Chem. Soc.* **2017**, *139*, 13083-13091.
- (72) He, X.; Sin, H.; Liang, B.; Ghazi, Z. A.; Khattak, A. M.; Khan, N. A.; Alanagh, H. R.; Li, L.; Lu, X.; Tang, Z. Controlling the Selectivity of Conjugated Microporous Polymer Membrane for Efficient Organic Solvent Nanofiltration, *Adv. Funct. Mater.* **2019**, *0*, 1900134.

- (73) Shirvany, R.; Chabert, M.; Tourneret, J. Ship and Oil-Spill Detection Using the Degree of Polarization in Linear and Hybrid/Compact Dual-Pol SAR, *IEEE Journal of Selected Topics in Applied Earth Observations and Remote Sensing* **2012**, *5*, 885-892.
- (74) Xue, Z.; Cao, Y.; Liu, N.; Feng, L.; Jiang, L. Special wettable materials for oil/water separation, *J. Mater. Chem. A* **2014**, *2*, 2445-2460.
- (75) Cheryan, M.; Rajagopalan, N. Membrane processing of oily streams. Wastewater treatment and waste reduction, *J. Membr. Sci.* **1998**, *151*, 13-28.
- (76) Padaki, M.; Surya Murali, R.; Abdullah, M. S.; Misdan, N.; Moslehyani, A.; Kassim, M. A.; Hilal, N.; Ismail, A. F. Membrane technology enhancement in oil–water separation. A review, *Desalination* **2015**, *357*, 197-207.
- (77) O’Loughlin, T. E.; Dennis, R. V.; Fler, N. A.; Alivio, T. E. G.; Ruus, S.; Wood, J.; Gupta, S.; Banerjee, S. Biomimetic Plastronic Surfaces for Handling of Viscous Oil, *Energy & Fuels* **2017**, *31*, 9337-9344.
- (78) Yaghi, O. M.; O’Keeffe, M.; Ockwig, N. W.; Chae, H. K.; Eddaoudi, M.; Kim, J. Reticular synthesis and the design of new materials, *Nature* **2003**, *423*, 705-714.
- (79) Li, J.-R.; Sculley, J.; Zhou, H.-C. Metal–Organic Frameworks for Separations, *Chem. Rev.* **2012**, *112*, 869-932.
- (80) Waller, P. J.; Gandara, F.; Yaghi, O. M. Chemistry of Covalent Organic Frameworks, *Acc Chem Res* **2015**, *48*, 3053-3063.
- (81) Feng, X.; Ding, X.; Jiang, D. Covalent organic frameworks, *Chem Soc Rev* **2012**, *41*, 6010-6022.
- (82) Xu, Y.; Jin, S.; Xu, H.; Nagai, A.; Jiang, D. Conjugated microporous polymers: design, synthesis and application, *Chem. Soc. Rev.* **2013**, *42*, 8012-8031.

- (83) Cooper, A. I. Conjugated Microporous Polymers, *Adv. Mater.* **2009**, *21*, 1291-1295.
- (84) Yuan, D.; Lu, W.; Zhao, D.; Zhou, H.-C. Highly Stable Porous Polymer Networks with Exceptionally High Gas-Uptake Capacities, *Adv. Mater.* **2011**, *23*, 3723-3725.
- (85) Lu, W.; Yuan, D.; Zhao, D.; Schilling, C. I.; Plietzsch, O.; Muller, T.; Bräse, S.; Guenther, J.; Blümel, J.; Krishna, R.; Li, Z.; Zhou, H.-C. Porous Polymer Networks: Synthesis, Porosity, and Applications in Gas Storage/Separation, *Chem. Mater.* **2010**, *22*, 5964-5972.
- (86) Sumida, K.; Rogow, D. L.; Mason, J. A.; McDonald, T. M.; Bloch, E. D.; Herm, Z. R.; Bae, T. H.; Long, J. R. Carbon dioxide capture in metal-organic frameworks, *Chem Rev* **2012**, *112*, 724-781.
- (87) Lee, J.; Farha, O. K.; Roberts, J.; Scheidt, K. A.; Nguyen, S. T.; Hupp, J. T. Metal-organic framework materials as catalysts, *Chem Soc Rev* **2009**, *38*, 1450-1459.
- (88) Yoon, M.; Srirambalaji, R.; Kim, K. Homochiral metal-organic frameworks for asymmetric heterogeneous catalysis, *Chem Rev* **2012**, *112*, 1196-1231.
- (89) Xu, H.; Gao, J.; Jiang, D. Stable, crystalline, porous, covalent organic frameworks as a platform for chiral organocatalysts, *Nat Chem* **2015**, *7*, 905-912.
- (90) Colson, J. W.; Dichtel, W. R. Rationally synthesized two-dimensional polymers, *Nat. Chem.* **2013**, *5*, 453-465.
- (91) Li, J.-R.; Kuppler, R. J.; Zhou, H.-C. Selective gas adsorption and separation in metal-organic frameworks, *Chem. Soc. Rev.* **2009**, *38*, 1477-1504.
- (92) Zhang, Y.; Yuan, S.; Feng, X.; Li, H.; Zhou, J.; Wang, B. Preparation of Nanofibrous Metal-Organic Framework Filters for Efficient Air Pollution Control, *J. Am. Chem. Soc.* **2016**, *138*, 5785-5788.

- (93) Weber, J.; Thomas, A. Toward Stable Interfaces in Conjugated Polymers: Microporous Poly(p-phenylene) and Poly(phenyleneethynylene) Based on a Spirobifluorene Building Block, *J. Am. Chem. Soc.* **2008**, *130*, 6334-6335.
- (94) Chen, L.; Honsho, Y.; Seki, S.; Jiang, D. Light-Harvesting Conjugated Microporous Polymers: Rapid and Highly Efficient Flow of Light Energy with a Porous Polyphenylene Framework as Antenna, *J. Am. Chem. Soc.* **2010**, *132*, 6742-6748.
- (95) Jiang, J.-X.; Su, F.; Trewin, A.; Wood, C. D.; Campbell, N. L.; Niu, H.; Dickinson, C.; Ganin, A. Y.; Rosseinsky, M. J.; Khimyak, Y. Z.; Cooper, A. I. Conjugated Microporous Poly(aryleneethynylene) Networks, *Angew. Chem. Int. Ed.* **2007**, *46*, 8574-8578.
- (96) Jiang, J.-X.; Su, F.; Trewin, A.; Wood, C. D.; Niu, H.; Jones, J. T. A.; Khimyak, Y. Z.; Cooper, A. I. Synthetic Control of the Pore Dimension and Surface Area in Conjugated Microporous Polymer and Copolymer Networks, *J. Am. Chem. Soc.* **2008**, *130*, 7710-7720.
- (97) Huang, L.; Wang, H.; Chen, J.; Wang, Z.; Sun, J.; Zhao, D.; Yan, Y. Synthesis, morphology control, and properties of porous metal-organic coordination polymers, *Microporous and Mesoporous Materials* **2003**, *58*, 105-114.
- (98) Congzhi, Z.; Lei, F. Mingling Electronic Chemical Sensors with Supramolecular Host-Guest Chemistry, *Curr. Org. Chem.* **2014**, *18*, 1957-1964.
- (99) Knopfmacher, O.; Hammock, M. L.; Appleton, A. L.; Schwartz, G.; Mei, J.; Lei, T.; Pei, J.; Bao, Z. Highly stable organic polymer field-effect transistor sensor for selective detection in the marine environment, *Nat Commun* **2014**, *5*, 2954.
- (100) Bisbey, R. P.; DeBlase, C. R.; Smith, B. J.; Dichtel, W. R. Two-dimensional Covalent Organic Framework Thin Films Grown in Flow, *J Am Chem Soc* **2016**, *138*, 11433-11436.

- (101) Je, Sang H.; Buyukcakir, O.; Kim, D.; Coskun, A. Direct Utilization of Elemental Sulfur in the Synthesis of Microporous Polymers for Natural Gas Sweetening, *Chem* **2016**, *1*, 482-493.
- (102) Wang, S.; Zhang, C.; Shu, Y.; Jiang, S.; Xia, Q.; Chen, L.; Jin, S.; Hussain, I.; Cooper, A. I.; Tan, B. Layered microporous polymers by solvent knitting method, *Sci. Adv.* **2017**, *3*.
- (103) Troschke, E.; Grätz, S.; Lübken, T.; Borchardt, L. Mechanochemical Friedel–Crafts Alkylation—A Sustainable Pathway Towards Porous Organic Polymers, *Angew. Chem. Int. Ed.* **2017**, *56*, 6859-6863.
- (104) Zhu, X.; Tian, C.; Mahurin, S. M.; Chai, S.-H.; Wang, C.; Brown, S.; Veith, G. M.; Luo, H.; Liu, H.; Dai, S. A Superacid-Catalyzed Synthesis of Porous Membranes Based on Triazine Frameworks for CO₂ Separation, *J. Am. Chem. Soc.* **2012**, *134*, 10478-10484.
- (105) Zhu, X.; Tian, C.; Chai, S.; Nelson, K.; Han, K. S.; Hagan, E. W.; Veith, G. M.; Mahurin, S. M.; Liu, H.; Dai, S. New Tricks for Old Molecules: Development and Application of Porous N-doped, Carbonaceous Membranes for CO₂ Separation, *Adv. Mater.* **2013**, *25*, 4152-4158.
- (106) Elmorsy, S. S.; Pelter, A.; Smith, K. The direct production of tri- and hexa-substituted benzenes from ketones under mild conditions, *Tetrahedron Letters* **1991**, *32*, 4175-4176.
- (107) Huang, C. Y.; Fu, W. F.; Li, C. Z.; Zhang, Z. Q.; Qiu, W. M.; Shi, M. M.; Heremans, P.; Jen, A. K. Y.; Chen, H. Z. Dopant-Free Hole-Transporting Material with a C-3h Symmetrical Truxene Core for Highly Efficient Perovskite Solar Cells, *J. Am. Chem. Soc.* **2016**, *138*, 2528-2531.
- (108) Cherioux, F.; Guyard, L. Synthesis and Electrochemical Properties of Novel 1,3,5-Tris(oligothienyl)benzenes: A New Generation of 3D Reticulating Agents, *Adv. Funct. Mater.* **2001**, *11*, 305-309.

- (109) Cao, X.-Y.; Zhang, W.-B.; Wang, J.-L.; Zhou, X.-H.; Lu, H.; Pei, J. Extended π -Conjugated Dendrimers Based on Truxene, *J. Am. Chem. Soc.* **2003**, *125*, 12430-12431.
- (110) Zhu, X.; Tian, C. C.; Chai, S. H.; Nelson, K.; Han, K. S.; Hagaman, E. W.; Veith, G. M.; Mahurin, S. M.; Liu, H. L.; Dai, S. New Tricks for Old Molecules: Development and Application of Porous N-doped, Carbonaceous Membranes for CO₂ Separation, *Adv. Mater.* **2013**, *25*, 4152-4158.
- (111) Rose, M.; Klein, N.; Senkovska, I.; Schrage, C.; Wollmann, P.; Böhlmann, W.; Böhringer, B.; Fichtner, S.; Kaskel, S. A new route to porous monolithic organic frameworks via cyclotrimerization, *J. Mater. Chem.* **2011**, *21*, 711-716.
- (112) Wisser, F. M.; Eckhardt, K.; Wisser, D.; Böhlmann, W.; Grothe, J.; Brunner, E.; Kaskel, S. Tailoring Pore Structure and Properties of Functionalized Porous Polymers by Cyclotrimerization, *Macromolecules* **2014**, *47*, 4210-4216.
- (113) Zhao, Y.-C.; Zhou, D.; Chen, Q.; Zhang, X.-J.; Bian, N.; Qi, A.-D.; Han, B.-H. Thionyl Chloride-Catalyzed Preparation of Microporous Organic Polymers through Aldol Condensation, *Macromolecules* **2011**, *44*, 6382-6388.
- (114) Zou, Y.; Yuan, T.; Yao, H.; Frazier, D. J.; Stanton, D. J.; Sue, H. J.; Fang, L. Solution-Processable Core-Extended Quinacridone Derivatives with Intact Hydrogen Bonds, *Org Lett* **2015**, *17*, 3146-3149.
- (115) D. Gernon, M.; Wu, M.; Buszta, T.; Janney, P. Environmental benefits of methanesulfonic acid . Comparative properties and advantages, *Green Chem.* **1999**, *1*, 127-140.
- (116) Yuan, S.; Dorney, B.; White, D.; Kirklin, S.; Zapol, P.; Yu, L.; Liu, D. J. Microporous polyphenylenes with tunable pore size for hydrogen storage, *Chem Commun (Camb)* **2010**, *46*, 4547-4549.

- (117) de Souza, A. C.; Pires, A. T. N.; Soldi, V. Thermal stability of ferrocene derivatives and ferrocene-containing polyamides, *Journal of Thermal Analysis and Calorimetry* **2002**, *70*, 405.
- (118) Kitagawa, S. Porous Materials and the Age of Gas, *Angew. Chem. Int. Ed.* **2015**, *54*, 10686-10687.
- (119) Kuznicki, S. M.; Bell, V. A.; Nair, S.; Hillhouse, H. W.; Jacubinas, R. M.; Braunbarth, C. M.; Toby, B. H.; Tsapatsis, M. A titanosilicate molecular sieve with adjustable pores for size-selective adsorption of molecules, *Nature* **2001**, *412*, 720-724.
- (120) Shetty, D.; Jahovic, I.; Raya, J.; Ravaux, F.; Jouiad, M.; Olsen, J.-C.; Trabolsi, A. An ultra-absorbent alkyne-rich porous covalent polycalix[4]arene for water purification, *J. Mater. Chem. A* **2017**, *5*, 62-66.
- (121) Gu, C.; Huang, N.; Chen, Y.; Qin, L.; Xu, H.; Zhang, S.; Li, F.; Ma, Y.; Jiang, D. π -Conjugated Microporous Polymer Films: Designed Synthesis, Conducting Properties, and Photoenergy Conversions, *Angew. Chem. Int. Ed.* **2015**, *54*, 13594-13598.
- (122) Jimenez-Solomon, M. F.; Song, Q.; Jelfs, K. E.; Munoz-Ibanez, M.; Livingston, A. G. Polymer nanofilms with enhanced microporosity by interfacial polymerization, *Nat. Mater.* **2016**, *15*, 760-767.
- (123) Chen, Y.; Li, S.; Pei, X.; Zhou, J.; Feng, X.; Zhang, S.; Cheng, Y.; Li, H.; Han, R.; Wang, B. A Solvent-Free Hot-Pressing Method for Preparing Metal–Organic-Framework Coatings, *Angew. Chem. Int. Ed.* **2016**, *55*, 3419-3423.
- (124) Ray, J. K.; Gupta, S.; Pan, D.; Kar, G. K. Molecular recognition: studies on the synthesis of some bis thiophene carboxamide derivatives as ditopic receptors for long chain dicarboxylic acids, *Tetrahedron* **2001**, *57*, 7213-7219.
- (125) Li, Y.; Zheng, Y. Synthesis and characterization of a ferrocene-modified, polyaniline-like conducting polymer, *Journal of Applied Polymer Science* **2016**, *133*.

- (126) Stobe, C.; Seto, R.; Schneider, A.; Lützen, A. Synthesis, Chiral Resolution, and Absolute Configuration of C₂-Symmetric, Chiral 9,9'-Spirobifluorenes, *European Journal of Organic Chemistry* **2014**, *2014*, 6513-6518.
- (127) Hsiao, T.-S.; Chen, T.-L.; Chien, W.-L.; Hong, J.-L. Molecular design for the highly-sensitive piezochromic fluorophores with tri-armed framework containing triphenyl-quinoline moiety, *Dyes and Pigments* **2014**, *103*, 161-167.
- (128) Liang, B.; He, X.; Hou, J.; Li, L.; Tang, Z. Membrane Separation in Organic Liquid: Technologies, Achievements, and Opportunities, *Adv. Mater.* **2018**, *0*, 1806090.
- (129) Liu, G.; Jin, W.; Xu, N. Two-Dimensional-Material Membranes: A New Family of High-Performance Separation Membranes, *Angew. Chem. Int. Ed.* **2016**, *55*, 13384-13397.
- (130) Yang, Q.; Su, Y.; Chi, C.; Cherian, C. T.; Huang, K.; Kravets, V. G.; Wang, F. C.; Zhang, J. C.; Pratt, A.; Grigorenko, A. N.; Guinea, F.; Geim, A. K.; Nair, R. R. Ultrathin graphene-based membrane with precise molecular sieving and ultrafast solvent permeation, *Nat. Mater.* **2017**, *16*, 1198-1202.
- (131) Wang, J.; Chen, P.; Shi, B.; Guo, W.; Jaroniec, M.; Qiao, S.-Z. A Regularly Channeled Lamellar Membrane for Unparalleled Water and Organics Permeation, *Angew. Chem. Int. Ed.* **2018**, *57*, 6814-6818.
- (132) Zhang, C.; Wu, B.-H.; Ma, M.-Q.; Wang, Z.; Xu, Z.-K. Ultrathin metal/covalent-organic framework membranes towards ultimate separation, *Chem. Soc. Rev.* **2019**, *48*, 3811-3841.
- (133) Cheng, X. Q.; Wang, Z. X.; Jiang, X.; Li, T.; Lau, C. H.; Guo, Z.; Ma, J.; Shao, L. Towards sustainable ultrafast molecular-separation membranes: From conventional polymers to emerging materials, *Prog. Mater. Sci.* **2018**, *92*, 258-283.
- (134) Livingston, A. G.; Baker, R. Membranes from academia to industry, *Nat. Mater.* **2017**, *16*, 280-282.

- (135) Kim, J. H.; Cook, M.; Park, S. H.; Moon, S. J.; Kim, J. F.; Livingston, A. G.; Lee, Y. M. A compact and scalable fabrication method for robust thin film composite membranes, *Green Chem.* **2018**, *20*, 1887-1898.
- (136) Park, H. B.; Kamcev, J.; Robeson, L. M.; Elimelech, M.; Freeman, B. D. Maximizing the right stuff: The trade-off between membrane permeability and selectivity, *Science* **2017**, *356*.
- (137) See Toh, Y. H.; Lim, F. W.; Livingston, A. G. Polymeric membranes for nanofiltration in polar aprotic solvents, *J. Membr. Sci.* **2007**, *301*, 3-10.
- (138) Li, Y.; Yuan, S.; Zhou, C.; Zhao, Y.; Van der Bruggen, B. A high flux organic solvent nanofiltration membrane from Kevlar aramid nanofibers with in situ incorporation of microspheres, *J. Mater. Chem. A* **2018**, *6*, 22987-22997.
- (139) Song, Q.; Jiang, S.; Hasell, T.; Liu, M.; Sun, S.; Cheetham, A. K.; Sivaniah, E.; Cooper, A. I. Porous Organic Cage Thin Films and Molecular-Sieving Membranes, *Adv. Mater.* **2016**, *28*, 2629-2637.
- (140) Gorgojo, P.; Karan, S.; Wong, H. C.; Jimenez-Solomon, M. F.; Cabral, J. T.; Livingston, A. G. Ultrathin Polymer Films with Intrinsic Microporosity: Anomalous Solvent Permeation and High Flux Membranes, *Adv. Funct. Mater.* **2014**, *24*, 4729-4737.
- (141) Fan, H.; Gu, J.; Meng, H.; Knebel, A.; Caro, J. High-Flux Membranes Based on the Covalent Organic Framework COF-LZU1 for Selective Dye Separation by Nanofiltration, *Angew. Chem. Int. Ed.* **2018**, *57*, 4083-4087.
- (142) Matsumoto, M.; Valentino, L.; Stiehl, G. M.; Balch, H. B.; Corcos, A. R.; Wang, F.; Ralph, D. C.; Mariñas, B. J.; Dichtel, W. R. Lewis-Acid-Catalyzed Interfacial Polymerization of Covalent Organic Framework Films, *Chem* **2018**, *4*, 308-317.
- (143) Yuan, S.; Li, X.; Zhu, J.; Zhang, G.; Van Puyvelde, P.; Van der Bruggen, B. Covalent organic frameworks for membrane separation, *Chem. Soc. Rev.* **2019**, *48*, 2665-2681.

- (144) Zhu, X.; Tian, C.; Chai, S.; Nelson, K.; Han, K. S.; Hagaman, E. W.; Veith, G. M.; Mahurin, S. M.; Liu, H.; Dai, S. New Tricks for Old Molecules: Development and Application of Porous N-doped, Carbonaceous Membranes for CO₂ Separation, *Adv. Mater.* **2013**, *25*, 4152-4158.
- (145) Ma, L.; Liu, Y.; Liu, Y.; Jiang, S.; Li, P.; Hao, Y.; Shao, P.; Yin, A.; Feng, X.; Wang, B. Ferrocene-Linkage-Facilitated Charge Separation in Conjugated Microporous Polymers, *Angew. Chem. Int. Ed.* **2019**, *58*, 4221-4226.
- (146) Talapaneni, S. N.; Kim, J.; Je, S. H.; Buyukcakir, O.; Oh, J.; Coskun, A. Bottom-up synthesis of fully sp² hybridized three-dimensional microporous graphitic frameworks as metal-free catalysts, *J. Mater. Chem. A* **2017**, *5*, 12080-12085.
- (147) Valtcheva, I. B.; Kumbharkar, S. C.; Kim, J. F.; Bhole, Y.; Livingston, A. G. Beyond polyimide: Crosslinked polybenzimidazole membranes for organic solvent nanofiltration (OSN) in harsh environments, *J. Membr. Sci.* **2014**, *457*, 62-72.
- (148) Thebo, K. H.; Qian, X.; Zhang, Q.; Chen, L.; Cheng, H.-M.; Ren, W. Highly stable graphene-oxide-based membranes with superior permeability, *Nat. Commun.* **2018**, *9*, 1486.
- (149) Guan, X.; Li, H.; Ma, Y.; Xue, M.; Fang, Q.; Yan, Y.; Valtchev, V.; Qiu, S. Chemically stable polyarylether-based covalent organic frameworks, *Nat. Chem.* **2019**, *11*, 587-594.
- (150) Wu, X.; Zhou, G.; Cui, X.; Li, Y.; Wang, J.; Cao, X.; Zhang, P. Nanoparticle-Assembled Thin Film with Amphipathic Nanopores for Organic Solvent Nanofiltration, *ACS Appl. Mater. & Interfaces* **2019**, *11*, 17804-17813.
- (151) Liu, M.-L.; Guo, J.-L.; Japip, S.; Jia, T.-Z.; Shao, D.-D.; Zhang, S.; Li, W.-J.; Wang, J.; Cao, X.-L.; Sun, S.-P. One-step enhancement of solvent transport, stability and photocatalytic properties of graphene oxide/polyimide membranes with multifunctional cross-linkers, *J. Mater. Chem. A* **2019**, *7*, 3170-3178.

- (152) Guo, Z.-H.; Wang, C.; Zhang, Q.; Che, S.; Zhou, H.-C.; Fang, L. Cost-effective synthesis and solution processing of porous polymer networks through methanesulfonic acid-mediated aldol triple condensation, *Mater. Chem. Front.* **2018**, *2*, 396-401.
- (153) Jung, S.-M.; Park, J.; Shin, D.; Jeong, H. Y.; Lee, D.; Jeon, I.-Y.; Cho, H.; Park, N.; Yoo, J.-W.; Baek, J.-B. Paramagnetic Carbon Nanosheets with Random Hole Defects and Oxygenated Functional Groups, *Angew. Chem. Int. Ed.* **2019**, *0*.
- (154) Luque, S.; Gómez, D.; Álvarez, J. R. In *Membrane Science and Technology*; Elsevier: 2008; Vol. 13, p 177-216.
- (155) Yao, T.; Guo, S.; Zeng, C.; Wang, C.; Zhang, L. Investigation on efficient adsorption of cationic dyes on porous magnetic polyacrylamide microspheres, *J. Hazard. Mater.* **2015**, *292*, 90-97.
- (156) Miyah, Y.; Lahrichi, A.; Idrissi, M.; Khalil, A.; Zerrouq, F. Adsorption of methylene blue dye from aqueous solutions onto walnut shells powder: Equilibrium and kinetic studies, *Surf. Interfaces* **2018**, *11*, 74-81.
- (157) Alqadami, A. A.; Naushad, M.; Alothman, Z. A.; Ahamad, T. Adsorptive performance of MOF nanocomposite for methylene blue and malachite green dyes: Kinetics, isotherm and mechanism, *J. Environ. Manage.* **2018**, *223*, 29-36.
- (158) Li, B.; Cui, Y.; Japip, S.; Thong, Z.; Chung, T.-S. Graphene oxide (GO) laminar membranes for concentrating pharmaceuticals and food additives in organic solvents, *Carbon* **2018**, *130*, 503-514.
- (159) Shi, G. M.; Farahani, M. H. A.; Liu, J. Y.; Chung, T.-S. Separation of vegetable oil compounds and solvent recovery using commercial organic solvent nanofiltration membranes, *J. Membr. Sci.* **2019**, *588*, 117202.
- (160) Bastin, M.; Hendrix, K.; Vankelecom, I. Solvent resistant nanofiltration for acetonitrile based feeds: A membrane screening, *J. Membr. Sci.* **2017**, *536*, 176-185.

- (161) Werth, K.; Kaupenjohann, P.; Knierbein, M.; Skiborowski, M. Solvent recovery and deacidification by organic solvent nanofiltration: Experimental investigation and mass transfer modeling, *J. Membr. Sci.* **2017**, *528*, 369-380.
- (162) Huang, L.; Chen, J.; Gao, T.; Zhang, M.; Li, Y.; Dai, L.; Qu, L.; Shi, G. Reduced Graphene Oxide Membranes for Ultrafast Organic Solvent Nanofiltration, *Adv. Mater.* **2016**, *28*, 8669-8674.
- (163) Chen, C.; Wang, J.; Liu, D.; Yang, C.; Liu, Y.; Ruoff, R. S.; Lei, W. Functionalized boron nitride membranes with ultrafast solvent transport performance for molecular separation, *Nat. Commun.* **2018**, *9*, 1902.
- (164) Zhang, J.; Seeger, S. Polyester Materials with Superwetting Silicone Nanofilaments for Oil/Water Separation and Selective Oil Absorption, *Adv. Funct. Mater.* **2011**, *21*, 4699-4704.
- (165) O'Loughlin, T. E.; Ngamassi, F.-E.; McKay, P.; Banerjee, S. Separation of Viscous Oil Emulsions Using Three-Dimensional Nanotetrapodal ZnO Membranes, *Energy & Fuels* **2018**, *32*, 4894-4902.
- (166) Li, S.; Huang, J.; Chen, Z.; Chen, G.; Lai, Y. A review on special wettability textiles: theoretical models, fabrication technologies and multifunctional applications, *J. Mater. Chem. A* **2017**, *5*, 31-55.
- (167) Ge, J.; Zhao, H.-Y.; Zhu, H.-W.; Huang, J.; Shi, L.-A.; Yu, S.-H. Advanced Sorbents for Oil-Spill Cleanup: Recent Advances and Future Perspectives, *Adv. Mater.* **2016**, *28*, 10459-10490.
- (168) Gupta, R. K.; Dunderdale, G. J.; England, M. W.; Hozumi, A. Oil/water separation techniques: a review of recent progresses and future directions, *J. Mater. Chem. A* **2017**, *5*, 16025-16058.

- (169) Ainsworth CH, P. C., Perlin N, Dornberger LN, Patterson WF III, Chancellor E, Impacts of the Deepwater Horizon oil spill evaluated using an end-to-end ecosystem model., *PLoS ONE* **2018**, 13(11): e0190840.
- (170) Si, Y.; Fu, Q.; Wang, X.; Zhu, J.; Yu, J.; Sun, G.; Ding, B. Superelastic and Superhydrophobic Nanofiber-Assembled Cellular Aerogels for Effective Separation of Oil/Water Emulsions, *ACS Nano* **2015**, 9, 3791-3799.
- (171) Cao, C.; Ge, M.; Huang, J.; Li, S.; Deng, S.; Zhang, S.; Chen, Z.; Zhang, K.; Al-Deyab, S. S.; Lai, Y. Robust fluorine-free superhydrophobic PDMS–ormosil@fabrics for highly effective self-cleaning and efficient oil–water separation, *J. Mater. Chem. A* **2016**, 4, 12179-12187.
- (172) Ge, J.; Zhang, J.; Wang, F.; Li, Z.; Yu, J.; Ding, B. Superhydrophilic and underwater superoleophobic nanofibrous membrane with hierarchical structured skin for effective oil-in-water emulsion separation, *J. Mater. Chem. A* **2017**, 5, 497-502.
- (173) Pan, Q.; Wang, M.; Wang, H. Separating small amount of water and hydrophobic solvents by novel superhydrophobic copper meshes, *Applied Surface Science* **2008**, 254, 6002-6006.
- (174) La, D.-D.; Nguyen, T. A.; Lee, S.; Kim, J. W.; Kim, Y. S. A stable superhydrophobic and superoleophilic Cu mesh based on copper hydroxide nanoneedle arrays, *Applied Surface Science* **2011**, 257, 5705-5710.
- (175) Lee, C.; Baik, S. Vertically-aligned carbon nano-tube membrane filters with superhydrophobicity and superoleophilicity, *Carbon* **2010**, 48, 2192-2197.
- (176) O'Loughlin, T. E.; Martens, S.; Ren, S. R.; McKay, P.; Banerjee, S. Orthogonal Wettability of Hierarchically Textured Metal Meshes as a Means of Separating Water/Oil Emulsions *Advanced Engineering Materials* **2017**, 19, 1600808.
- (177) Bajpayee, A.; Alivio, T. E. G.; McKay, P.; Banerjee, S. Functionalized Tetrapodal ZnO Membranes Exhibiting Superoleophobic and Superhydrophilic Character for

Water/Oil Separation Based on Differential Wettability, *Energy & Fuels* **2019**, 33, 5024-5034.

(178) Hench, L. L.; West, J. K. The sol-gel process, *Chem. Rev.* **1990**, 90, 33-72.

(179) Zhang, J.; Pu, G.; Severtson, S. J. Fabrication of Zinc Oxide/Polydimethylsiloxane Composite Surfaces Demonstrating Oil-Fouling-Resistant Superhydrophobicity, *ACS Appl. Mater. & Interfaces* **2010**, 2, 2880-2883.

(180) Jin, X.; Deng, M.; Kaps, S.; Zhu, X.; Hölken, I.; Mess, K.; Adelung, R.; Mishra, Y. K. Study of Tetrapodal ZnO-PDMS Composites: A Comparison of Fillers Shapes in Stiffness and Hydrophobicity Improvements, *PLOS ONE* **2014**, 9, e106991.

(181) Ortiz-Acosta, D. Sylgard® Cure Inhibition Characterization. United States: N. p., 2012. Web. doi:10.2172/1053123.

(182) Wang, C.; Fuller, T.; Zhang, W.; Wynne, K. J. Thickness Dependence of Ice Removal Stress for a Polydimethylsiloxane Nanocomposite: Sylgard 184, *Langmuir* **2014**, 30, 12819-12826.

(183) Zimmermann, J.; Seeger, S.; Reifler, F. A. Water Shedding Angle: A New Technique to Evaluate the Water-Repellent Properties of Superhydrophobic Surfaces, *Textile Research Journal* **2009**, 79, 1565-1570.

(184) Li, J.; Kang, R.; Tang, X.; She, H.; Yang, Y.; Zha, F. Superhydrophobic meshes that can repel hot water and strong corrosive liquids used for efficient gravity-driven oil/water separation, *Nanoscale* **2016**, 8, 7638-7645.

(185) Li, J.; Yan, L.; Li, H.; Li, W.; Zha, F.; Lei, Z. Underwater superoleophobic palygorskite coated meshes for efficient oil/water separation, *J. Mater. Chem. A* **2015**, 3, 14696-14702.

- (186) Li, J.; Li, D.; Li, W.; Li, H.; She, H.; Zha, F. Facile fabrication of underwater superoleophobic SiO₂ coated meshes for separation of polluted oils from corrosive and hot water, *Separation and Purification Technology* **2016**, *168*, 209-214.
- (187) Gao, S.; Zhu, Y.; Gong, Y.; Wang, Z.; Fang, W.; Jin, J. Ultrathin Polyamide Nanofiltration Membrane Fabricated on Brush-Painted Single-Walled Carbon Nanotube Network Support for Ion Sieving, *ACS Nano* **2019**, *13*, 5278-5290.
- (188) Pramanik, C.; Gissinger, J. R.; Kumar, S.; Heinz, H. Carbon Nanotube Dispersion in Solvents and Polymer Solutions: Mechanisms, Assembly, and Preferences, *ACS Nano* **2017**, *11*, 12805-12816.
- (189) Zhao, Y.; Yao, K. X.; Teng, B.; Zhang, T.; Han, Y. A perfluorinated covalent triazine-based framework for highly selective and water-tolerant CO₂ capture, *Energy & Environmental Science* **2013**, *6*, 3684-3692.